HIGH-THROUGHPUT PHENOTYPING OF LARGE WHEAT BREEDING NURSERIES USING UNMANNED AERIAL SYSTEM, REMOTE SENSING AND GIS TECHNIQUES

by

ATENA HAGHIGHATTALAB

B.S., Isfahan University, 2007
M.S., K.N Toosi University of Technology, 2010

AN ABSTRACT OF A DISSERTATION

Submitted in partial fulfillment of the requirements for the degree

DOCTOR OF PHILOSOPHY

Department of Geography
College of Arts and Sciences

KANSAS STATE UNIVERSITY
Manhattan, Kansas

2016

Abstract

Wheat breeders are in a race for genetic gain to secure the future nutritional needs of a growing population. Multiple barriers exist in the acceleration of crop improvement. Emerging technologies are reducing these obstacles. Advances in genotyping technologies have significantly decreased the cost of characterizing the genetic make-up of candidate breeding lines. However, this is just part of the equation. Field-based phenotyping informs a breeder's decision as to which lines move forward in the breeding cycle. This has long been the most expensive and time-consuming, though most critical, aspect of breeding. The grand challenge remains in connecting genetic variants to observed phenotypes followed by predicting phenotypes based on the genetic composition of lines or cultivars.

In this context, the current study was undertaken to investigate the utility of UAS in assessment field trials in wheat breeding programs. The major objective was to integrate remotely sensed data with geospatial analysis for high throughput phenotyping of large wheat breeding nurseries. The initial step was to develop and validate a semi-automated high-throughput phenotyping pipeline using a low-cost UAS and NIR camera, image processing, and radiometric calibration to build orthomosaic imagery and 3D models. The relationship between plot-level data (vegetation indices and height) extracted from UAS imagery and manual measurements were examined and found to have a high correlation. Data derived from UAS imagery performed as well as manual measurements while exponentially increasing the amount of data available. The high-resolution, high-temporal HTP data extracted from this pipeline offered the opportunity to develop a within season grain yield prediction model. Due to the variety in genotypes and environmental conditions, breeding trials are inherently spatial in nature and vary non-randomly across the field. This makes geographically weighted regression models a good choice as a

geospatial prediction model. Finally, with the addition of georeferenced and spatial data integral in HTP and imagery, we were able to reduce the environmental effect from the data and increase the accuracy of UAS plot-level data.

The models developed through this research, when combined with genotyping technologies, increase the volume, accuracy, and reliability of phenotypic data to better inform breeder selections. This increased accuracy with evaluating and predicting grain yield will help breeders to rapidly identify and advance the most promising candidate wheat varieties.

HIGH-THROUGHPUT PHENOTYPING OF LARGE WHEAT BREEDING NURSERIES USING UNMANNED AERIAL SYSTEM, REMOTE SENSING AND GIS TECHNIQUES

by

ATENA HAGHIGHATTALAB

B.S., Isfahan University, 2007
M.S., K. N. Toosi University of Technology, 2010

A DISSERTATION

Submitted in partial fulfillment of the requirements for the degree

DOCTOR OF PHILOSOPHY

Department of Geography
College of Arts and Sciences

KANSAS STATE UNIVERSITY
Manhattan, Kansas

2016

Approved by:

Co-Major Professor
Jesse A. Poland

Approved by:

Co-Major Professor
Douglas Goodin

Approved by:

Co-Major Professor
Kevin Price

Copyright

Abstract

Wheat breeders are in a race for genetic gain to secure the future nutritional needs of a growing population. Multiple barriers exist in the acceleration of crop improvement. Emerging technologies are reducing these obstacles. Advances in genotyping technologies have significantly decreased the cost of characterizing the genetic make-up of candidate breeding lines. However, this is just part of the equation. Field-based phenotyping informs a breeder's decision as to which lines move forward in the breeding cycle. This has long been the most expensive and time-consuming, though most critical, aspect of breeding. The grand challenge remains in connecting genetic variants to observed phenotypes followed by predicting phenotypes based on the genetic composition of lines or cultivars.

In this context, the current study was undertaken to investigate the utility of UAS in assessment field trials in wheat breeding programs. The major objective was to integrate remotely sensed data with geospatial analysis for high throughput phenotyping of large wheat breeding nurseries. The initial step was to develop and validate a semi-automated high-throughput phenotyping pipeline using a low-cost UAS and NIR camera, image processing, and radiometric calibration to build orthomosaic imagery and 3D models. The relationship between plot-level data (vegetation indices and height) extracted from UAS imagery and manual measurements were examined and found to have a high correlation. Data derived from UAS imagery performed as well as manual measurements while exponentially increasing the amount of data available. The high-resolution, high-temporal HTP data extracted from this pipeline offered the opportunity to develop a within season grain yield prediction model. Due to the variety in genotypes and environmental conditions, breeding trials are inherently spatial in nature and vary non-randomly across the field. This makes geographically weighted regression models a good choice as a

geospatial prediction model. Finally, with the addition of georeferenced and spatial data integral in HTP and imagery, we were able to reduce the environmental effect from the data and increase the accuracy of UAS plot-level data.

The models developed through this research, when combined with genotyping technologies, increase the volume, accuracy, and reliability of phenotypic data to better inform breeder selections. This increased accuracy with evaluating and predicting grain yield will help breeders to rapidly identify and advance the most promising candidate wheat varieties.

Table of Contents

List of Figures

List of Tables

Acknowledgements

To my family. Obviously.

To Dr. Poland who gave me a unique opportunity.

To my advisers.

To Poland lab, technicians, scientists, and support staff who made these research opportunities accessible to me.

And to William Zorrilla whom I cannot thank enough.

Chapter 1 - Introduction

A plant phenotype is a set of structural, morphological, physiological, and performance-related traits of a given genotype in a defined environment (Granier & Vile 2014). The phenotype results from the interactions between a plant's genes and environmental factors. Plant phenotyping involves a broad range of plant measurements such as growth development, canopy architecture, physiology, disease and pest response and yield. Traditional phenotyping methods often rely on simple tools like rulers and other measuring devices, along with significant amounts of manual work, to extract the desired trait data. Compared to advanced genotyping methods such as the latest sequencing technologies, traditional phenotyping methods are time-consuming, labor-intensive, and cost-inefficient. This limits our ability to quantitatively understand how genetic traits are related to plant growth, environmental adaptation, and yield.

Great interest in plant high-throughput phenotyping (HTP) techniques has arisen, in the past several years. HTP is an assessment of plant phenotypes on a scale and scope not achievable with traditional methods such as visual scoring and manual measurements (Dhondt et al. 2013). HTP techniques use sensor systems and automated computer algorithms to extract phenotypic traits for large genetic mapping populations using non-destructive and non-invasive sampling methods. To be useful to breeding programs, HTP methods must be amenable to plot sizes, experimental designs and field conditions in these programs. This requires evaluating a large number of lines within a short time span, methods that are lower cost and less labor intensive than current techniques, and accurately assessing and making selections in large populations consisting of thousands to tens-of-thousands of plots (Sanchez, A et al. 2014; Haghighattalab et al. 2016). Use of information technologies such as remote sensing and computational tools are necessary to rapidly identify the growth responses of genetically distinct plants in the field and link these responses to individual genes.

The extraction of data via HTP platforms requires a series of discrete steps that must be reliably executed in sequence. Such a set of steps is referred to as a "pipeline".

In recent years, most focused has been done on automation of data acquisition using a robotic vehicle with imaging systems and sensors. Less well-developed are data pipelines that automate data storage, processing, and analysis of the data extracted from these phenotyping platforms (White et al. 2012). Therefore, a slow manual collection of small amounts of data will get replaced by a slow manual management of large amounts of automatically-collected data unless we develop an automatic data analysis pipeline.

To address this challenge, we describe here and the chapters that follow a semi-automated HTP analysis pipeline using an unmanned aerial vehicle (UAV) platform, which will improve the capability of breeders to assess great numbers of lines in field trials. Then we will use remote sensing and geographic information (GIS) techniques to predict grain yield using the information extracted from UAS imagery, and finally, we will adjust the data, using the geostatistical approaches, for the spatial variation in the field.

This dissertation focuses on the areas in which plant phenotyping can be improved and how remote sensing and GIS can be incorporated into breeding programs. Some of the problems and panaceas investigated are: 1.) Development of a semi-automated HTP analysis pipeline using a low cost unmanned aerial system (UAS) platform, and 2.) within-season grain yield prediction using spatio-temporal unmanned aerial systems imagery 3.) spatial adjustment of HTP data extracted from UAS imagery of field trial in wheat breeding nurseries.

Pipeline Development

Multispectral remote sensing plays a key role in precision agriculture due to its ability to represent crop growth condition on a spatial and temporal scale as well as its cost effectiveness.

In recent years, there has been increased interest in ground-based and aerial HTP platforms, particularly for applications in breeding and germplasm evaluation activities (Deery et al. 2014; Fiorani & Schurr 2013; Walter et al. 2015). Ground-based phenotyping platforms include modified vehicles using proximal sensing sensors (Busemeyer et al. 2013; Sanchez, A et al. 2014; Crain et al. 2015).

One of the emerging technologies in aerial based systems is UAV, which has undergone a remarkable development in recent years and is now a robust sensor-bearing platform for various agricultural and environmental applications (Dunford et al. 2009; Chapman et al. 2014). UAVs can cover an entire research site in a very short time, giving a rapid evaluation of the whole field and individual plots while minimizing the environment effects such as wind, cloud cover, and solar radiation. UAVs with sensors enable measuring with high spatial and temporal resolution, and capable of generating useful information for plant breeding programs.

With the introduction of HTP through UAV equipped with sensors, breeding programs can rapidly and reliably collect phenotypic data with minimal labor costs. This lowering of labor cost constraints allows for breeders to increase the number of lines assessed, thereby increasing the chance of achieving greater numbers of superior lines.

Recent advances in platform design, as well as the ability to the production of thousands of imagery and geo-referencing, and mosaicking the images, and extracting useful information from the imagery requires a workflow to execute HTP with UAS as a conventional tool in plant breeding. Additionally, developing efficient and easy-to-use pipelines to process HTP data and disseminate associated algorithms are necessary when dealing with big data. The primary objective of chapter 2 was to develop and validate a pipeline for processing data obtained by consumer grade digital cameras using a low-cost UAS to evaluate small plot field-based research typical of plant breeding programs.

Grain Yield Prediction

The primary objective of chapter 3 was to determine whether an accurate remote sensing based method could be developed to monitor plant growth and estimate grain yield using aerial spatio-temporal imagery in small plot wheat nurseries.

Multispectral sensors significantly help in exploring the relationships between crop biophysical data with crop production and yield. Many empirical relationships have been established in the past between spectral vegetation indices and crop growth rates through ground sampling or by using crop growth yield models. These relationships are then used by the crop growers, and breeders to estimate the expected yield of crops within season, to make crop management and production related decisions for maximizing field productivity and market gains.

To examine the value of UAS in plant breeding and the data derived from the imagery, chapter 3 looks at how HTP measurements can be collected throughout the growing season, how geostatistical methods can be used to add value to data taken at multiple times throughout the growing season and predict grain yield. The purpose of this research is to evaluate the performance of geographically weighted models in predicting grain yields at plot level in breeding nurseries.

Spatial Adjustment

The introduction of geographic information system (GIS), global positioning systems (GPS) and remote sensing in agriculture, has resulted in more accurate and efficient mapping of field variability.

The phenotypes are determined by the genetics of each entry in the nursery but also influenced by the spatial variation across the field along with the variation of genotypic values. To improve the accuracy of selections, breeder needs to account for non-heritable environmental variation in the form of spatial field effects. To improve the accuracy of selections, breeder needs to account for environmental variation in the form of spatial field effects. These variations are caused by multiple environmental factors that can vary across a field such as soil fertility, soil type, moisture holding capacity, and also many human-made variations such as irrigation system, the direction of cultivation/harvesting, and previous crop cycles (Funda et al. 2007; Bos 2008; Sarker & Singh 2015).

The goal of chapter 4 is to evaluate the use of moving grid, integrate with spatial information extracted from UAS images to adjust for environmental variation in high throughput phenotypic data and yield of a large wheat breeding nursery.

The eye in the sky

Aerial and NIR imagery have been used for more than 50 years to monitor crop growth. In recent years, the application of unmanned aerial systems for crop studies and precision agriculture has been gaining importance due to the improvements in the spatial and spectral resolution of the sensors, and also the smaller size of the cameras to be mounted on these platforms.

Recent studies have shown the potential of UAS in monitoring of plant growth for different crops such as wheat, corn, cotton, sorghum, rice, and so on (Swain et al. 2010; Haghighattalab et al. 2016; Neely et al. 2016; Hunt et al. 2008; Lelong et al. 2008).

The pipeline developed in this study is applicable to any crop types. GW regression as described in chapter 3 can also be used to predict grain yield for any other crops, and also can be used to predict grain yield from multiyear data set as long as data is provided from the same exact location. The spatial adjustment technique developed and explained in chapter 4, can be applied to any breeding field with spatial variation.

REFERENCE

Haghighattalab, A. et al., 2016. Application of unmanned aerial systems for high throughput phenotyping of large wheat breeding nurseries Application of unmanned aerial systems for high throughput phenotyping of large wheat breeding nurseries. *Plant Methods*, (August). Available at: "http://dx.doi.org/10.1186/s13007-016-0134-6.

Hunt, E.R. et al., 2008. Remote Sensing of Crop Leaf Area Index Using Unmanned Airborne Vehicles. *October*, 17, pp.18–20. Available at: http://www.asprs.org/publications/proceedings/pecora17/0018.pdf.

Lelong, C.C.D. et al., 2008. Assessment of unmanned aerial vehicles imagery for quantitative monitoring of wheat crop in small plots. *Sensors*, 8(5), pp.3557–3585.

Neely, L. et al., 2016. Unmanned Aerial Vehicles for High- Throughput Phenotyping and Agronomic Research. *PLoS ONE*, 11(7), pp.1–26.

Swain, K.C., Thomson, S.J. & Jayasuriya, H.P.W., 2010. Adoption of an Unmanned Helicopter for Low-Altitude Remote Sensing to Estimate Yield and Total Biomass of a Rice Crop. , 53(1). Available at: http://elibrary.asabe.org/abstract.asp?aid=29493&t=3.

Chapter 2 - Application of Unmanned Aerial Systems for High Throughput Phenotyping of Large Wheat Breeding Nurseries

This chapter has been published as following journal article:

Haghighattalab A, González Pérez L, Mondal S, Singh D, Schinstock D, Rutkoski J, Ortiz-Monasterio I, Singh RP, Goodin D, Poland J: Application of unmanned aerial systems for high throughput phenotyping of large wheat breeding nurseries. Plant Methods 2016, 12:1–15

Abbreviations

BER, Band Equivalent Reflectance; CIMMYT, International Maize and Wheat Improvement Center; DEM, Digital Elevation Model; DN, Digital Number; DPP, Digital Photo Professional; ENDVI, Enhanced Normalized Difference Vegetation Index; FWHM, Full Width at Half Maximum; GCP, Ground Control Points; GIPVI, Infrared Percentage Vegetation Index; GNDVI, Green Normalized Difference Vegetation Index; GSD, Ground Sampling Distance; HTP, High-throughput Phenotyping; LAI, Leaf Area Index; NDVI, Normalized Difference Vegetation Index; NIR, Near Infrared; RENDVI, Red-edge Normalized Difference Vegetation Index; RMSE, Root Mean Square Error; SIFT, Scale-invariant Feature Transform; UAS, Unmanned Aerial System; UAV, Unmanned Aerial Vehicle; VI, Vegetation Index

ABSTRACT

Background: Low cost unmanned aerial systems (UAS) have great potential for rapid proximal measurements of plants in agriculture. In the context of plant breeding and genetics, current approaches for phenotyping a large number of breeding lines under field conditions require substantial investments in time, cost, and labor. For field-based high-throughput phenotyping (HTP), UAS platforms can provide high-resolution measurements for small plot research, while enabling the rapid assessment of tens-of-thousands of field plots. The objective of this study was to complete a baseline assessment of the utility of UAS in assessment field trials as commonly implemented in wheat breeding programs. We developed a semi-automated image-processing pipeline to extract plot level data from UAS imagery. The image dataset was processed using a photogrammetric pipeline based on image orientation and radiometric calibration to produce orthomosaic images. We also examined the relationships between vegetation indices (VIs) extracted from high spatial resolution multispectral imagery collected with two different UAS systems (eBee Ag carrying MultiSpec 4C camera, and IRIS+ quadcopter carrying modified NIR Canon S100) and ground truth spectral data from hand-held spectroradiometer.

Results: We found good correlation between the VIs obtained from UAS platforms and ground-truth measurements and observed high broad-sense heritability for VIs. We determined radiometric calibration methods developed for satellite imagery significantly improved the precision of VIs from the UAS. We observed VIs extracted from calibrated images of Canon S100 had a significantly higher correlation to the spectroradiometer ($r = 0.76$) than VIs from the

MultiSpec 4C camera (r = 0.64). Their correlation to spectroradiometer readings was as high as or higher than repeated measurements with the spectroradiometer per se.

Conclusion: The approaches described here for UAS imaging and extraction of proximal sensing data enable collection of HTP measurements on the scale and with the precision needed for powerful selection tools in plant breeding. Low-cost UAS platforms have great potential for use as a selection tool in plant breeding programs. In the scope of tools development, the pipeline developed in this study can be effectively employed for other UAS and also other crops planted in breeding nurseries.

KEY WORDS

unmanned aerial vehicles / systems (UAV / UAS)
wheat
high-throughput phenotyping
remote sensing
GNDVI
Plot extraction

INTRODUCTION

In a world of finite resources, climate variability, and increasing populations, food security has become a critical challenge. The rates of genetic improvement are below what is needed to meet projected demand for staple crops such as wheat [1]. The grand challenge remains in connecting genetic variants to observed phenotypes followed by predicting phenotypes in new genetic combinations. Extraordinary advances over the last 5-10 years in sequencing and genotyping technology have driven down the cost and are providing an abundance of genomic data, but this only comprise half of the equation to understand the function of plant genomes and predicting plant phenotypes [2, 3]. High throughput phenotyping (HTP) platforms could provide the keys to connecting the genotype to phenotype by both increasing the capacity and precision and reducing the time to evaluate huge plant populations. To get to the point of predicting the real-world performance of plants, HTP platforms must innovate and advance to the level of quantitatively assessing millions of plant phenotypes. To contribute to this piece of the challenge, we describe here a semi-automated HTP analysis pipeline using a low cost unmanned aerial system (UAS) platform, which will increase the capacity of breeders to assess large numbers of lines in field trials.

A plant phenotype is a set of structural, morphological, physiological, and performance-related traits of a given genotype in a defined environment [4]. The phenotype results from the interactions between a plant's genes and environmental (abiotic and biotic) factors. Plant phenotyping involves a wide range of plant measurements such as growth development, canopy architecture, physiology, disease and pest response and yield. In this context, HTP is an assessment of plant phenotypes on a scale and with a level of speed and precision not attainable with traditional methods [5], many of which include visual scoring and manual measurements. To be useful to breeding programs, HTP methods must be amenable to plot sizes, experimental designs and field conditions in these programs. This entails evaluating a large number of lines within a short time span, methods that are lower cost and less labor intensive than current techniques, and accurately assessing and making selections in large populations consisting of thousands to tens-of-thousands of plots. To rapidly characterize the growth responses of genetically different plants in the field and relate these responses to individual genes, use of information technologies such as proximal or remote sensing and efficient computational tools are necessary.

In recent years, there has been increased interest in ground-based and aerial HTP platforms, particularly for applications in breeding and germplasm evaluation activities [6–8]. Ground-based phenotyping platforms include modified vehicles deploying proximal sensing sensors [9–12]. Measurements made at a short distance with tractors and hand-held sensors that do not necessarily involve measurements of reflected radiation, are classified as proximal sensing. Proximal, or close-range sensing, is expected to provide higher resolution for phenotyping studies as well as allowing collection of data with multiple view-angles, illumination control and known distance from the plants to the sensors [13]. However, these ground-based platforms do have limitations mainly on the scale at which they can be used, limitations on portability and time required to make the measurements in different field locations.

As a complement to ground-based platforms, aerial-based phenotyping platforms enable the rapid characterization of many plots, overcoming one of the limitations associated with ground-based phenotyping platforms. There is a growing body of literature showing how these approaches in remote and proximal sensing enhance the precision and accuracy of automated high-throughput field based phenotyping techniques [14–16]. One of the emerging technologies in aerial based platforms is UAS, which have undergone a remarkable development in recent years and are now powerful sensor-bearing platforms for various agricultural and environmental applications [17–21]. UAS can cover an entire experiment in a very short time, giving a rapid assessment of all of the plots while minimizing the effect of environmental conditions that change rapidly such as wind speed, cloud cover, and solar radiation. UAS enables measuring with high spatial and temporal resolution capable of generating useful information for plant breeding programs.

Different types of imaging systems for remote sensing of crops are being used on UAS platforms. Some of the cameras used are RGB, multispectral, hyperspectral, thermal cameras, and low cost consumer grade cameras modified to capture near infrared (NIR) [2, 9, 21–23]. Consumer grade digital cameras are widely used as the sensor of choice due to their low cost, small size and weight, low power requirements, and their potential to store thousands of images. However, consumer grade cameras often have the challenge of not being radiometrically calibrated. In this study, we evaluated the possibility of using traditional radiometric calibration methods developed for satellite imagery to address this issue.

Radiometric calibration accounts for both variations from photos within an observation day along with changes between different dates of image. The result of radiometric calibration is a more generalized and, most importantly, repeatable, method for different image processing techniques (such as derivation of VIs, change detection, and crop growth mapping) applied to the orthomosaic image instead of each individual image in a dataset. There are well-established radiometric calibration approaches for satellite imagery. However, these approaches are not necessarily applicable in UAS workflows due to several factors such as conditions of data acquisition during the exact time of image capture using these platforms.

Empirical line method is a technique often applied to perform atmospheric correction to convert at-sensor radiance measurements to surface reflectance for satellite imagery, although this technique can be modified to apply radiometric calibration and convert digital numbers (DNs) to reflectance values [24]. The method is based on the relationship between DNs and surface reflectance values measured from calibration targets located within the image using a field spectroradiometer. The extracted DNs from the imagery are then compared with the field-measured reflectance values to calculate a prediction equation that can be used to convert DNs to reflectance values for each band [25].

Advances in platform design, production, standardization of image geo-referencing, mosaicking, and information extraction workflow are needed to implement HTP with UAS as a routine tool in plant breeding and genetics. Additionally, developing efficient and easy-to-use pipelines to process HTP data and disseminate associated algorithms are necessary when dealing with big data. The primary objective of this research was to develop and validate a pipeline for processing data captured by consumer grade digital cameras using a low cost UAS to evaluate small plot field-based research typical of plant breeding programs.

MATERIALS and METHODS

Study Area

The study was conducted at Norman E Borlaug Experiment Station at Ciudad Obregon, Sonora, Mexico (Figure 1). The experiment consisted of 1092 advanced wheat lines distributed in 39 trials, each trial consisting of 30 entries. Each trial was arranged as an alpha lattice with three replications. The experimental units were 2.8m x 1.6m in size consisting of paired rows at 0.15m spacing, planted on two raised beds spaced 0.8m apart. The trials were planted later than optimal on February 24, 2015 to simulate heat stress with temperatures expected to be above optimum for the entire growing season (the local recommended planting date is November 15 to December 15). Irrigation and nutrient levels in the heat trials were maintained at optimal levels, as well as weed, insect and disease control. Grain yield was obtained by using a plot combine harvester.

Platforms and Cameras

We evaluated two unmanned aerial vehicles (UAV); the IRIS+ (3D Robotics, Inc, Berkeley, CA 94710, USA) and eBee Ag (senseFly Ltd., 1033 Cheseaux-Lausanne, Switzerland).

The IRIS+ is a low cost quadcopter UAV with a maximum payload of 400 g. The open-source Pixhawk autopilot system was programmed for autonomous navigation for the IRIS+

based on ground coordinates and the ‘survey’ option of Mission Planner (Pixhawk sponsored by 3D Robotics, www.planner.ardupilot.com). The IRIS+ is equipped with an uBlox GPS with integrated magnetometer. A Canon S100 modified by MaxMax (LDP LLC, Carlstadt, NJ 07072, USA, www.maxmax.com) to Blue-Green-NIR (400-760nm) was mounted to the UAV with a gimbal designed by Kansas State University. The gimbal compensates for the UAV movement (pitch and roll) during the flight to allow for nadir image collection.

The eBee Ag, designed as a fixed wing UAV for application in precision agriculture has a payload of 150 g. This UAV was equipped with MultiSpec 4C camera developed by Airinov (Airinov, 75018 Paris, France, www.airinov.fr/en/uav-sensor/agrosensor/) and customized for the eBee Ag. It contains four distinct bands with no spectral overlap (530-810nm): green, red, red-edge, and near infrared bands, and is controlled by the eBee Ag autopilot during the flight.

For ‘ground-truth’ validation, spectral measurements were taken using ASD VNIR handheld point-based spectroradiometer (ASD Inc., Boulder, CO, http://www.asdi.com/) with a wavelength range of 325 nm – 1075 nm, a wavelength accuracy of ±1 nm and a spectral resolution of <3 nm at 700 nm with a fiber optics of 25° (aperture) full conical angle. The instrument digitizes spectral values to 16 bits. Table 1 summarizes the specification for the cameras and sensor used in this study.

Ground Control Points

In order to geo-reference the aerial images, at the beginning of the season ten ground control points (GCPs) were distributed across the field. The GCPs were 25 cm x 25 cm square white metal sheets mounted on a 50 cm post. The GCPs were white to provide easy identification for the image processing software. The GCP coordinates were measured with a Trimble R4 RTK GPS, with a horizontal accuracy of 0.025 m and a vertical accuracy of 0.035 m. These targets were maintained throughout the crop season to enable more accurate geo-referencing of UAS aerial imagery and overlay of measurements from multiple dates.

Reflectance Calibration Panel

For radiometric calibration, spectra of easily recognizable objects (e.g. gray scale calibration board) are needed. A black-gray-white grayscale board with known reflectance values was built and placed in the field during flights for further image calibration. This grayscale calibration panel met the requirements for further radiometric calibration including 1) the panel was spectrally homogenous, 2) it was near Lambertian and horizontal, 3) it covered an area many times larger than the pixel size of the Canon S100, and 4) covered a range of reflectance values [25].

The calibration panel used in this study had 6 levels of gray from 0% being white and 100% being black, printed on matte vinyl. This made it possible to choose several dark and bright regions in the images to provide a more accurate regression for further radiometric calibration analysis. Photos of the calibration panel were taken in the field before a UAS flight using the same Canon S100 NIR camera mounted on the IRIS+. Using an ASD spectroradiometer on a sunny day, the spectral reflectance was measured of the panel at a fixed altitude of 0.50 m from different angles.

Field Data Collection

At the study site, image time series were acquired using IRIS+ and Canon S100 camera during the growing season as evenly spaced as possible, depending on the weather condition; April 10, April 22, April 28, May 6, and May 18, 2015.

Field data measurements for the experiment in this study included 1) IRIS+ carrying modified NIR Canon S100, and 2) eBee Ag carrying MultiSpec 4C camera, and 3) spectral reflectance measurements using handheld ASD spectroradiometer collected on May 6, 2015 when the trials were at mid grain filling. We took all field measurements within one hour around solar noon to minimize variation in illumination and solar zenith angle [26]. This limited the number of plots we could measure using handheld spectroradiometer to 280 plots. Four spectra per plot were taken with the beam of the fiber optics placed at 0.50 m over the top of the canopy with a sample area of 0.04 m2. Due to this very small sampling area, great care was taken in data collection to make sure the measured spectral responses were only from the crops.

Both the eBee and IRIS+ were able to image a much larger area in the same time frame. Each system was flown using a generated autopilot path that covered the 2 ha experiment area with an average of 75% overlap between images (Table 2).

For the IRIS+ with Canon S100, all images were taken in RAW format (.CR2) to avoid loss of image information. The Canon S100 settings were TV mode, which allowed setting of a constant shutter speed. The aperture was set to be auto-controlled by the camera to maintain a good exposure level, and ISO speed was set to Auto with a maximum value of 400 to minimize noise in the images. Focus range was manually set to infinity. We used CHDK (www.chdk.wkia.com) to automate Canon S100's functionality by running intervalometer scripts off an SD card in order to take pictures automatically at intervals during flight. The CHDK script allowed the UAS autopilot system to send electronic pulses to trigger the camera shutter. The camera trigger was set at the corresponding distance interval during the mission planning for the desired image overlap.

The eBee MultiSpec 4C camera had a predefined setting by Sensefly; ISO and shutter speed was set to automatic, maximum aperture was set to f/1.8 and focal distance was fixed at 4 mm.

Developing an image processing pipeline for HTP

In this research, a UAS-based semi-automated data analyses pipeline was developed to enable HTP analysis of large breeding nurseries. Data analysis was primarily conducted using Python scripts [27, 28]. The dataset used to develop the image processing pipeline was collected on May 6, 2015 with the IRIS+ flights carrying the modified NIR Canon S100 camera. In order to analyze hundreds of images taken by a UAS that represent the entire experiment area, we developed a semi-automated data analysis pipeline. The developed pipeline completed the following steps: 1) Image pre-processing, 2) Georeferencing and orthomosaic generation, 3) Image radiometric calibration, 4) Calculation of different VIs and 5) plot-level data extraction from the VI maps. The overall workflow of the developed pipeline is presented in Figure 2, and a detailed description of each segment is provided.

The RAW images of Canon S100 (.CR2 format) were pre-processed using Digital Photo Professional (DPP) software developed by Canon (http://www.canon.co.uk/support/camera_software/). This software to convert RAW to Tiff also included lens distortion correction, chromatic aberration, and gamma correction. For white balance adjustment, we used the pictures of grayscale calibration panel taken during the flights. After pre-processing the images were exported as a tri-band 16-bit linear TIFF image.

Image Stitching and Orthomosaic Generation

We then generated a geo-referenced orthomosaic image using the TIFF images. There are several software packages for mosaicking UAS aerial imagery, all based around the scale-invariant feature transform algorithm (SIFT) algorithm for feature matching between images [29]. While there are slight differences between packages each performs the same operation namely loading photos; aligning photos; importing GCP positions; building dense point cloud; building digital elevation model (DEM); and finally generating the orthomosaic image. We used the commercial Agisoft PhotoScan package (Agisoft LLC, St. Petersburg, Russia, 191144) to automate the orthomosaic generation within a custom Python script. The procedure of generating the orthomosaic using PhotoScan comprises five main stages 1) camera alignment, 2) importing GCPs and geo-referencing, 3) building dense point cloud, 4) building DEM and 5) generating orthomosaic [30].

For alignment, PhotoScan finds the camera position and orientation for each photo and builds a sparse point cloud model; the software uses the SIFT algorithm to find matching points of detected features across the photos. PhotoScan offers two options for pair selection: generic and reference. In generic pre-selection mode, the overlapping pairs of photos are selected by matching photos using the lower accuracy setting. On the other hand, in reference mode the overlapping pairs of photos are selected based on the measured camera locations. We examined both methods to generate the orthomosaic and compared the results.

With aerial photogrammetry the location information delivered with cameras is inadequate and the data does not align properly with other geo-referenced data. In order to do further spatial and temporal analysis with aerial imagery, we performed geo-referencing using GCPs. We used 10 GCPs evenly distributed around the orthomosaic image. Geo-referencing with GCPs is the step that still requires manual input.

The main source of error in georeferencing is performing the linear transformation matrix on the model. In order to remove the possible non-linear deformation components of the model, and minimizing the sum of re-projection error and reference coordinate misalignment, PhotoScan offers an optimization of the estimated point cloud and camera parameters based on the known reference coordinates [30].

After alignment optimization, the next step is generating dense point clouds. Based on the estimated camera positions PhotoScan calculates depth information for each camera to be combined into a single dense point cloud [30]. PhotoScan allows creating a raster DEM file from a dense point cloud, a sparse point cloud or a mesh to represent the model surface as a regular grid of height values. Although most accurate results are calculated based on dense point cloud data.

The final step is orthomosaic generation. An orthomosaic can be created based on either mesh or DEM data. Mesh surface type can be chosen for models that are not referenced. The blending mode has two options (mosaic and average) to select how pixel values from different photos will be combined in the final texture layer. Average blending computes the average brightness values from all overlapping images to help reduce the effect of the bidirectional reflectance distribution function that is strong within low altitude wide-angle photography [31]. Blending pixel values using mosaic mode does not mix image details of overlapping photos, but uses only images where the pixel in question is located within the shortest distance from the image center. We compared these two methods by creating orthomosaic images using both mosaic and average mode.

Radiometric Calibration

After the orthomosaic was completed, we then performed radiometric calibration to improve the accuracy of surface spectral reflectance obtained using digital cameras. We applied empirical line correction to each orthomosaic within the data set using field measurements taken with the ASD. The relationship between image raw DNs and their corresponding reflectance values is not completely linear for all the bands for Canon S100 camera and most digital cameras (Figure 3). To relate remote sensing data to field-based measurements we used a modified empirical line method [32]. We used the grayscale calibration board combined with reflectance measurements from the ASD spectroradiometer to find the relationship between DNs extracted form Canon S100 and surface reflectance values measured from grayscale calibration board using a field spectroradiometer. We then calculated the prediction equations for each band separately to convert DNs to reflectance values.

We calculated the mean pixel value of the calibration panel extracted from images for each band separately, and plotted against the mean band equivalent reflectance (BER) of field spectra [33, 34]. We found a linear relation between the natural logarithm of image raw DN values and their corresponding BER, although the relation between image raw DNs and their corresponding BER was not completely linear for all bands of Canon S100 (Figure 3). We derived the correction coefficient needed to fit uncalibrated UAS multispectral imagery to field-measured reflectance spectra. Using the correction coefficient for each band, we then performed this correction on the entire image.

With the corrected orthomosaic, a map showing the vegetation indices can be generated. The most used VIs derivable from a three-band multispectral sensor are: normalized difference vegetation index (NDVI), and green normalized difference vegetation index (GNDVI) (Table 4). NDVI is calculated from reflectance measurements in the red and NIR portion of the spectrum and its values range from −1.0 to 1.0. GNDVI is computed similarly to the NDVI, where the green band is used instead of the red band and its value ranges from 0 to 1.0. Like NDVI, this index is also related to the proportion of photosynthetically absorbed radiation and is linearly correlated with Leaf Area Index (LAI) and biomass [22, 35, 36].

Field Plot Extraction

In order to get useful information about each wheat plot in the field, we need to extract plot level data from the orthomosaic VI image. Individual wheat plot boundaries need to be extracted and defined separately from images with an assigned plot ID that defines their genomic type. We examined three approaches for extracting plot boundaries from the orthomosaic image: a simple grid based plot extraction, field-map based plot extraction, and image classification/segmentation.

To apply a simple grid superimposed on top of the orthomosaic image we used the Fishnet function using Arcpy scripting in ArcGIS. This function creates a net of adjacent rectangular cells. The output is polygon features defining plot boundaries. Creating a fishnet requires two basic pieces of information: the spatial extent of the desired net, and the number of rows and columns. The number of rows and ranges (columns) and height and width of each cell in the fishnet can be defined by the user. The user can also define the extent of the grid by supplying both the minimum and maximum x- and y-coordinates.

The next method we evaluated in this study is a field-map based method. Experimental or field data are usually stored in a spreadsheet. To accomplish this, we reformatted the field map in order to represent the plots in the field; the first row of the excel sheet is the length (or width, depending on how plots are located in the field) of the plots, and the first column is the width (or length). Each cell in the excel sheet is the plot ID and other information regarding that particular plot available in the field map.

In this approach, first we created a KML file from the field map (.CSV) using Python [27], we generated polygon shapefiles with known size for each plot from KML file, and assigned plot ID to each plot using the field map. To define the geographic extent of the field, the python script has inputs for the coordinate of two points in the field: the start point of the first plot on the top right and the end point of the last plot on the bottom left. The script starts from the top right and builds the first polygon using the defined plot size, and skips the gap between plots and generates the next one until it gets to the last plot on the bottom left. In this approach the plot IDs are assigned automatically and simultaneously from the field map excel sheet. The most important advantage of this approach is that it can be generalized to other crop types as long as the field map is provided and the plots are planted in regular distance and have a consistent size within a trial.

The third method is to extract wheat plot boundaries from the orthomosaic image directly. To examine this method, we used the April 10 data set instead of May 6. The reason for choosing this set of data was that in this dataset we had the most distinguished features (e.g. vegetation vs. bare soil) in the image compared to the image data taken on May 6. We classified the GNDVI image created from the orthomosaic image into four classes: “Wheat”, “Shadow”, “Soil”, and a class named “Others” for all the GCP targets in the field. The class “shadow” stands for the shadow projected on the soil surface. In this supervised classification, we defined training samples and signature files for each defined class. After classifying the image, we merged the “Shadow”,” Soil” and “Others” classes together and ended up with two classes: “Wheat”, and “Non-wheat”. The classified image often needs further processing to clean up the random noise and small isolated regions to improve the quality of the output. With a simple segmentation, we extracted wheat plot polygons from the image.

This method works best with high-resolution imagery taken at the beginning of the growing season when all the classes are clearly distinguishable from each other on the image. Otherwise time consuming post-processing is needed in order to separate the mixed classes.

To analyze the result of VI extraction from the orthomosaic, we used the zonal statistics plugin in the open source software QGIS. We calculated several values of the pixels of orthomosaic (such as the average VI values, Min, Max, standard deviation, majority, minority and also the median of VI values for each plot and the total count of the pixels that are within a plot boundary), using the polygonal vector layer of plot boundaries generated by one of the methods above. We then merged the data from the field map spreadsheet (plot ID, entry numbers, trial name, number of rep, number of block, row and column, and other information on planting) with the generated plots statistics.

Accuracy evaluation of different types of aerial imagery sensors and platforms

To evaluate the accuracy and reliability of our low cost UAS and consumer grade camera, we calculated correlations between calibrated DN values from the orthomosaic images of Canon S100 and MultiSpec 4C camera and band equivalent reflectance (BER) of field spectra. For ground-truth evaluation we used the ASD Fieldspectro 2 spectroradiometer to measure spectral reference of 280 sample plots after running the UAS within the time window of 1 hour around noon. The ASD spectroradiometer measures a wavelength range of 325 nm – 1075 nm, a wavelength accuracy of ±1 nm and a spectral resolution of <3 nm at 700 nm (Table 1). Using the ASD, the top of canopy reflectance was measured approximately 0.5 m above the plants. To account for the very small field of view of this sensor, we constantly monitored the spectral response curves to avoid measuring mixed pixels in our samplings and we averaged four reflectance readings within each sample plots. Reflectance measurements were calibrated at every 15 plots using a white (99% reflectance) Spectralon calibration panel.

To evaluate the accuracy of each platform, we calculated the correlations between different VIs extracted from Canon S100 and VIs extracted from MultiSpec 4C compared to the BER of field spectra. We calculated BER for each camera separately by taking the average of all the spectroradiometer bands that are within the full width at half maximum (FWHM) of each instrument (Table 1). The Pearson correlation between the average VI values of the sample plots and field spectra for each platform was calculated. The resulting correlation coefficients were tested using a two-tail test of significance at the $p \leq 0.05$ level. Accuracy assessment was based on computing the root mean square error (RMSE) for GNDVI image by comparing the pixel values of the reflectance image to the corresponding BER of field spectra at the sample sites not selected to generate the regression equations.

Broad-sense Heritability

Broad-sense heritability, commonly known as repeatability, is an index used by plant breeders and geneticists to measure precision of a trial [37–39]. The ratio of the genetic variance to the total phenotypic variance is broad-sense heritability (H2), which varies between 0 and 1. A heritability of 0 indicates there is no genetic variation contributing to phenotypic variation, and

H2 of 1 if the entire phenotypic variation is due to genetic variation and no environmental noise. For the purpose of comparing phenotyping tools and approaches, broad-sense heritability calculated for measurements on a given set of plots under field conditions at the same point in time, is a direct assessment of measurement error as the genetics and environmental conditions are constant.

In order to assess the accuracy of the different HTP platforms, we calculated broad-sense heritability on an entry-mean basis for each individual trial and phenotypic sampling date on May 6, 2015. To calculate heritability, we performed a two steps process where we first calculated the plot average and then fit a mixed model for replication, block and entry as random effects. Heritability was calculated from equation 1 [40].

$$H^2 = \frac{\sigma^2_{genotypic}}{\sigma^2_{phenotypic}} = \frac{\sigma^2_{genotypic}}{\sigma^2_{genotypic} + \frac{\sigma^2_{error}}{replication}} \quad (1)$$

Where$\sigma^2_{genotypic}$is genotypic variance and σ^2_{error} is error variance.

RESULTS and DISCUSSION

Developing an image processing pipeline for HTP

To evaluate the potential of UAS for plant breeding programs, we deployed a low cost, consumer grade UAS and imaging system at multiple times throughout the growing season. Using the aerial imagery collected on May 6, we built a robust pipeline scripted in Python that facilitated image analysis and allowed a semi-automated image analysis algorithm to run with minimum user support. The only requirement for manual input in the processing pipeline is to validate the GCP positions. This pipeline was tested on eight temporal datasets collected from IRIS+ flights over heat trials during the growing season.

The individual parameters selected during orthomosaic generation and plot extraction can have a large impact on the quality of the orthomosaic and subsequent data analysis. Because of the multiple parameter settings that users could choose, we investigated how changing various parameters would affect the data quality. To obtain more accurate camera position estimates, we selected higher accuracy at the alignment step. For pair selection mode, we chose reference since in this mode the overlapping pairs of photos are selected based on the estimated camera locations (i.e. from the GPS log of the control system). For the upper limit of feature points on every image to be taken into account during alignment stage, we accepted the default value of 40000. We imported positions for all of the ten GCPs available on the field to geo-reference the aerial images. The GCPs were also used in the self-calibrating bundle adjustment to ensure correct geo-location and to avoid any systematic error or block deformation. To improve georeferencing accuracy, we performed alignment optimization.

Finally, to generate orthomosaic, we tested the two methods of blending: mosaic and average. We found the orthomosaic generated by the mosaic method gives more quality for the orthomosaic and texture atlas than the average mode. On the other hand, mosaic blending mode generated artifacts in the image since it uses fewer images by selecting pixels with the shortest distance from the image center (Figure 4). We examined the correlation between orthomosaic generated from these two approaches and the ground truth data and found the averaging method has slightly higher correlation of 0.68 compared to mosaic method with the correlation of 0.65.

The 16 bit orthomosaic TIFF image was generated semi-automatically using python scripting in PhotoScan software with a resolution of 0.8 centimeters, matching the ground sampling distance (GSD) of the camera. Due to the short flight times (less than 20 minutes) and low flying altitude (30 meters above ground level), we assume there is no need for atmospheric corrections [28].

To convert DNs to reflectance values, a modified empirical approach was implemented using pixel values of IRIS+ aerial imagery and field-based reflectance measurements from handheld spectroradiometer. Calibration equations (2, 3, and 4) calculated from non-linear relationship between average field spectra and relative spectra response of each band separately were determined as:

$$Reflectance_{Blue} = -\,exp(-log(4.495970e^{-01} + (3.191189e^{-05}) * DN_{Blue}))) \qquad (2)$$
$(r^2 = 0.98\,, P < 0.001)$

$$Reflectance_{Green} = -\,exp(-log(4.705485e^{-01} + (3.735676e^{-05}) * DN_{Green}))) \qquad (3)$$
$(r^2 = 0.97, P < 0.001)$

$$Reflectance_{NIR} = -\,exp(-log(1.197440e^{+00} + (4.712299e^{-05}) * DN_{NIR}))) \qquad (4)$$
$(r^2 = 0.94, P < 0.001)$

We applied each calibration equation to their corresponding band image and converted the image raw DNs into reflectance values.

Wheat Plot boundary extraction results

We evaluated multiple approaches for defining and overlaying plot coordinate boundaries for the large field trials. As breeding trials are regularly containing thousands or tens of thousands of plots, an automated or semi-automated approach to generating and overlaying plot boundaries is needed.

Simple-grid based method

We first implemented a simple overlay grid (Figure 5a) using QGIS open source software. This method, although fast and easy, is not accurate for plot assigning as it does not account for within plot gaps (for plots planted in beds), gaps between plots and also gaps between each range of wheat plots. It simply generates polygons attached to each other and not spaced as needed to correctly capture the actual plot boundaries (Figure 5a). In the example below, it can also be noticed that a boundary polygon may cover part of the neighbor wheat plot, which is due to the assumption of a fixed plot boundary size in this method. To account for the gap between plots, beds and also between ranges of plots, we developed a field map based method.

Field-map based method

To accurately reflect the actual field planting and plot size, we developed a script to overlay defined plot sizes with known spacing. We reformatted the field map using the information in the spreadsheet such as: plot ID, and plot's location based on the block number, column and row's number, and also knowing the plots were planted on beds with a plot size of 2.8 m length and 1.6 m wide. This method allows us to eliminate border effect by changing the plot size to 2.3 m by 1.5 m. In the reformatted field map spreadsheet, the first row of the excel sheet is the length of the plots (1.5 m) and the length of the gap between plots in beds (0.15 m) and gaps between each bed (0.8 m). The first column is the width of wheat plots (2.3 m) and the width of the gaps between each range (0.5 m). The cells in the reformatted spreadsheet are filled with the plot's information including plot ID, trial name, and planting date. From this plot level information, we overlay plots of the defined size with plot-to-plot spacing that accurately reflects the field configuration (Figure 5b).

Image Classification Plot Extraction

To examine an image classification based plot extraction method, we first generated GNDVI from the orthomosaic image generated from the April 10 aerial imagery rather than the May 6 dataset analyzed in the rest of this study. The reason for choosing this set of data was that in this dataset from earlier in the season had the sharpest contrast between plots and the surrounding soil. We then applied a Maximum Likelihood Classification to the GNDVI image. We converted the classified image into polygons to obtain plot shape polygons (Figure 5c). This approach is more reliable if the early season aerial imagery is provided. The drawback with this approach is that it requires post-processing and cleanup of the final result if the classes are not quite distinguished and separated from each other in the orthomosaic image. Frequently, this approach did not separate plots properly and manual editing was required (Figure 5c). As it can be seen in the Figure 5c, the two plots slightly merged with each other and it caused the classification to classify them as one single plot. To have more accurate results from image classification method, the presence of early season imagery is needed, since this process can have more post-processing and cleanup if the wheat plots and the gaps between plots are not visually discrete from each other in the images.

Plot-level GNDVI Extraction Results

After generating VI maps, we compared these three plot-level extraction techniques using GNDVI values extracted form canon S100 aerial imagery and the corresponding values extracted from spectroradiometer in the field. The field-map based approach for plot polygons generated the best correlation to spectroradiometer measurements, while the classification technique had the lowest correlation with ground-truth data (Table 3). The lower reliability of classification technique compared to field-map based, could be due to the absence of early season imagery. In generating plot boundaries using field-map based, we also considered a buffer around the polygons to avoid any possible mixed plants or border effects for a plot which likely improved performance. We then correlated plot level GNDVI calculated from the spectral reflectance for those same plots using different boundary plot extraction methods (Table 3). From the comparison of different plot extraction methods with correlation to spectral reflectance we found that the boundaries defined using the map-based algorithm were superior to both the simple grid and the classification-based approach (Table 3).

Empirical Line Correction

Using Python scripting in QGIS, we generated different VI maps from the calibrated orthomosaic image and extracted plot boundaries using the field-map based method. Using the zonal statistics plugin, we then calculated statistic values of each plot of wheat in the orthomosaic. For each individual plot, the average VI value was used for further analysis and correlation. We tested the utility of applying an empirical line correction to improve the converting of digital numbers to reflectance values for the cameras. Using the same field-map based plot extraction, the correlation between raw GNDVI values extracted from the orthomosaic image and the BER increased from 0.68 to 0.76 after performing empirical line method as the radiometric calibration method.

Comparison of Different Vegetation Indices

To test the accuracy of VI from the digital cameras by comparison to the ASD spectroradiometer, we calculated BER for Canon S100 by taking the average of all the spectroradiometer bands that are within the FWHM of this camera (Table 1). For example, to calculate BER GNDVI for Canon S100, we averaged the reflectance values between 490-550 nm as green band, and averaged all the values between 680-760 nm as NIR band.

Among all the calculated VIs for the Canon S100, GNDVI had the highest correlation with the spectroradiometer (Table 4, Figure 6). Since the MultiSpec 4C camera has 4 bands, NIR, red-edge, Red and Green, we were able to generate a Red-edge normalized difference vegetation index (RENDVI) as well as other VIs. Using the developed pipeline, we extracted wheat plots from the generated orthomosaic for RENDVI by means of the field-map based method, which had also proved to be the best method of plot extraction for the MultiSpec 4C camera. The RENDVI plot values had higher correlation with spectroradiometer when compared to other VIs extracted from MultiSpec 4C camera (Figure 7).

Although it needs to be noted that red edge band used in MultiSpec 4C camera is not within the red edge region common in remote sensing sensors (680 – 730 nm) and is more of a NIR band. Which makes the RENDVI calculated from this camera to be more close to NDVI.

We found the correlation between VIs extracted from spectroradiometer and calibrated Canon S100 was significantly higher than the one with MultiSpec 4C camera. This could be due to lower flight altitude, and slower movements of multi-rotor IRIS+ compare to fixed wing eBee Ag, which results in higher resolution imagery captured by IRIS+ / Canon S100. The MultiSpec 4C camera is a narrow band multispectral camera that does not have any spectral overlap in its band response. The better spectral performance could be negated by the lower resolution of the sensor, higher flight altitude, and faster travel speed of the fixed wing UAV. It was also clear that the modified empirical line correction also played a role in higher correlation of Canon S100 values with ground truth spectral measurements.

We also calculated the correlation between the spectra readings using the handheld spectroradiometer. As we had four readings per plot, we were able to determine the repeatability within the spectroradiometer measurements. We averaged the first two measurements of and last two measurements for each plot independently and calculated an overall correlation for 280 sample plots (Table 5). Based on this assessment, the UAS imaging had repeatability as good as, or better than the spectroradiometer.

Broad Sense Heritability

As the Canon S100 and MultiSpec 4C measurements were taken at the same time on the same day and on the same plots, the environmental variance and genetic variance can be considered as negligible. Therefore, the broad sense heritability values (H2) can be interpreted as a level of precision of sensor measurement, which is the only remaining significant source of error variance. Overall the heritability for VIs was high. We found VIs derived from the Canon

S100 imagery had a higher heritability than the MultiSpec 4C data for nine out of eleven trials (Table 6). The trials had lower, but still high, heritability for grain yield. There were some unexpected rains during the crop cycle followed by irrigation issues in the borders of the field, however, the heritability for yield was still above 0.60 which is a moderate repeatability for breading trials under heat (Table 6).

CONCLUSION

We developed a semi-automated pipeline for data analysis of a low cost UAS imagery. The raw images of a consumer grade digital camera were pre-processed and used as the input of the image-processing pipeline. During the mosaicking step, we found that the averaging method had marginally higher correlation of 0.68 compared to mosaic method with the correlation of 0.65. Using a modified empirical line method, we radiometrically calibrated the DN values extracted from canon S100 and compared the calibrated digital values with the reflectance values of the spectroradiometer to evaluate the comparability of our data. Our results confirm that radiometric calibration is important for consumer grade cameras to convert the DN values to reflectance measurements and can improve the value of the image data.

We examined three different ways of wheat plot extraction: simple grid, field-map based, and image classification. We found that the field-map based technique is more accurate and fastest compared to other techniques, and had a higher correlation to ground truth data. The advantage of this method is that it is applicable to any crop types as long as the field map is provided, and also this method is fully automated in Python.

We evaluated two types of UAS; 1) low cost: IRIS+ and 2) commercial grade agriculture-use: eBee Ag, each carrying different sensors with 1) low cost consumer grade camera: modified NIR Canon S100 on the IRIS+ and 2) a more specialized multispectral camera: MultiSpec 4C camera on the eBee. We compared their performance with ground-truth reflectance data and found overall good performance to spectroradiometer measurements. Based on correlation to the spectral readings and assessment of heritability, the Canon S100 had better performance than the MultiSpec 4C mounted on the fixed wing, which was likely a result of higher resolution of the sensor, lower altitude and slower travel speed for the Canon S100 carried on the quadcopter IRIS+.

Our study provides strong evidence of the value of UAS for HTP applied to large wheat breeding nurseries. Further work is needed to investigate the strength of the relationship between remotely sensed derived plant phenological traits and the wheat biophysical properties collected in the field such as plant height, biomass, and yield. With the overall vision of integrating multiple measurements extracted from UAS (plant height, ground cover, etc.) with plant growth simulations to maximize the biological utility of the estimated phenotypes new avenues will be opened to breeders for predicting yield. Moreover, the development of new sensors and imaging systems undoubtedly will continue to improve our ability to phenotype very large experiments or breeding nurseries. When combined with genomic and physiological modeling, the rapid, low-cost evaluation of large field trials in plant breeding with UAS platforms has the potential to greatly accelerate the breeding process through more accurate selections on larger populations.

Acknowledgements

This work was done through the International Maize and Wheat Improvement Center (CIMMYT), Mexico and supported through the National Science Foundation - Plant Genome Research Program (IOS-1238187) and the US Agency for International Development Feed the Future Innovation Lab for Applied Wheat Genomics (Cooperative Agreement No. AID-OAA-A-13-00051).

Competing Interests

The authors declare no competing interests.

Authors' Contributions

Conceived and designed the study: DS, RPS, DG and JP; Developed and Validated Methods: AH, LGP, DS, and IOM; Collected Data: AH, LGP, SM, JR, and RPS; Analyzed Data and Interpreted Results: AH, SM and JP; All authors prepared and approved the manuscript.

REFERENCES

1. Ray DK, Mueller ND, West PC, Foley J a: Yield Trends Are Insufficient to Double Global Crop Production by 2050. PLoS One 2013, 8:e66428.

2. White JW, Andrade-Sanchez P, Gore M a., Bronson KF, Coffelt T a., Conley MM, Feldmann K a., French AN, Heun JT, Hunsaker DJ, Jenks M a., Kimball B a., Roth RL, Strand RJ, Thorp KR, Wall GW, Wang G: Field-based phenomics for plant genetics research. F Crop Res 2012, 133:101–112.

3. Cobb JN, DeClerck G, Greenberg A, Clark R, McCouch S: Next-generation phenotyping: requirements and strategies for enhancing our understanding of genotype–phenotype relationships and its relevance to crop improvement. Theor Appl Genet 2013, 126:867–887.

4. Granier C, Vile D: Phenotyping and beyond: Modelling the relationships between traits. Curr Opin Plant Biol 2014, 18:96–102.

5. Dhondt S, Wuyts N, Inzé D: Cell to whole-plant phenotyping: the best is yet to come. Trends Plant Sci 2013, 18:428–39.

6. Furbank R, Tester M: Phenomics–technologies to relieve the phenotyping bottleneck. Trends Plant Sci 2011, 16:635–44.

7. Fiorani F, Schurr U: Future scenarios for plant phenotyping. Annu Rev Plant Biol 2013, 64:267–91.

8. Walter A, Liebisch F, Hund A: Plant phenotyping: from bean weighing to image analysis. Plant Methods 2015, 11:14.

9. Busemeyer L, Mentrup D, Möller K, Wunder E, Alheit K, Hahn V, Maurer H, Reif J, Würschum T, Müller J, Rahe F, Ruckelshausen A: BreedVision — A Multi-Sensor Platform for Non-Destructive Field-Based Phenotyping in Plant Breeding. Sensors 2013, 13:2830–2847.

10. Andrade-Sanchez P, Gore MA, Heun JT, Thorp KR, Carmo-Silva AE, French AN, Salvucci ME, White JW: Development and evaluation of a field-based high- throughput phenotyping platform. Funct Plant Biol 2014, 41:68–79.

11. Crain J, Wei Y, Barker J, Sean T, Alderman P, Reynolds M, Zhang N, Poland J: Development and deployment of a portable field phenotyping platform. Crop Sci 2015.

12. Deery D, Jimenez-Berni J, Jones H, Sirault X, Furbank R: Proximal Remote Sensing Buggies and Potential Applications for Field-Based Phenotyping. Volume 4; 2014.

13. White J, Andrade-Sanchez P, Gore MA, Bronson KF, Coffelt TA, Conley MM, Feldmann KA, French AN, Heun JT, Hunsaker DJ, Jenks MA, Kimball BA, Roth RL, Strand RJ, Thorp KR, Wall GW, Wang G: Field-based phenomics for plant genetics research. F Crop Res 2012, 133:101–112.

14. Berger B, Parent B, Tester M: High-throughput shoot imaging to study drought responses. J Exp Bot 2010, 61:3519–28.

15. Munns R, James R a, Sirault XRR, Furbank RT, Jones HG: New phenotyping methods for screening wheat and barley for beneficial responses to water deficit. J Exp Bot 2010, 61:3499–507.

16. Araus JL, Cairns JE: Field high-throughput phenotyping: the new crop breeding frontier. Trends Plant Sci 2014, 19:52–61.

17. Baluja J, Diago MP, Balda P, Zorer R, Meggio F, Morales F, Tardaguila J: Assessment of vineyard water status variability by thermal and multispectral imagery using an unmanned aerial vehicle (UAV). Irrig Sci 2012, 30:511–522.

18. Chao H, Cao Y, Chen Y: Autopilots for small unmanned aerial vehicles: A survey. Int J Control Autom Syst 2010, 8:36–44.

19. Dunford R, Michel K, Gagnage M, Piégay H, Trémelo M-L: Potential and constraints of Unmanned Aerial Vehicle technology for the characterization of Mediterranean riparian forest. Int J Remote Sens 2009, 30:4915–4935.

20. Gonzalez-Dugo V, Zarco-Tejada P, Nicolás E, Nortes P a., Alarcón JJ, Intrigliolo DS, Fereres E: Using high resolution UAV thermal imagery to assess the variability in the water status of five fruit tree species within a commercial orchard. Precis Agric 2013, 14:660–678.

21. Chapman S, Merz T, Chan A, Jackway P, Hrabar S, Dreccer M, Holland E, Zheng B, Ling T, Jimenez-Berni J: Pheno-Copter: A Low-Altitude, Autonomous Remote-Sensing Robotic Helicopter for High-Throughput Field-Based Phenotyping. Agronomy 2014, 4:279–301.

22. Hunt, Jr. ER, Hively WD, Fujikawa SJ, Linden DS, Daughtry CST, McCarty GW: Acquisition of NIR-Green-Blue Digital Photographs from Unmanned Aircraft for Crop Monitoring. Remote Sens 2010, 2:290–305.

23. Liebisch F, Kirchgessner N, Schneider D, Walter A, Hund A: Remote, aerial phenotyping of maize traits with a mobile multi-sensor approach. Plant Methods 2015, 11:9.

24. Haest B, Biesemans J, Horsten W, Development S, Everaerts J, Manager P, Camp N Van, Valckenborgh J Van: Radiometric Calibration of Digital Photogrammetric. Proc ASPRS Annu Meet 2009.

25. Smith GM, Milton EJ: The use of the empirical line method to calibrate remotely sensed data to reflectance. Int J Remote Sens 1999, 20:2653–2662.

26. Gu XF, Guyot G, Verbrugghe M: Evaluation of measurement errors in ground surface reflectance for satellite calibration. Int J Remote Sens 1992, 13:2531–2546.

27. Haghighattalab A: Plot Boundary Extraction. http://dx.doi.org/10.5281/zenodo.46732. 2015.

28. Haghighattalab A, Agisoft LLC: Orthomosaic generation. http://dx.doi.org/10.5281/zenodo.46734. 2014.

29. Lowe DG: Distinctive Image Features from Scale-Invariant Keypoints. Int J Comput Vis 2004, 60:91–110.

30. Agisoft LLC: Agisoft PhotoScan User Manual: Professional Edition, Version 1.2. 2016.

31. Wang C, Price KP, Van Der Merwe D, An N, Wang H: Modeling above ground Biomass in Tallgrass Prairie using Ultra High Spatial Resolution sUAS Imagery. Photogramm Eng Remote Sens 2014, 80:1151–1159.

32. Staben GW, Pfitzner K, Bartolo R, Lucieer A: Empirical line calibration of WorldView-2 satellite imagery to reflectance data: using quadratic prediction equations. Remote Sens Lett 2012, 3:521–530.

33. Staben G, Pfitzner K: Calibration of WorldView-2 Satellite Imagery to Reflectance Data Using an Empirical Line Method. Proc 34th Int Symp Remote Sens Environ GEOSS Era Towar Oper Environ Monit Sydney, Aust 2011.

34. Wang C, Myint SW: A Simplified Empirical Line Method of Radiometric Calibration for Small Unmanned Aircraft Systems-Based Remote Sensing. IEEE J Sel Top Appl Earth Obs Remote Sens 2015, 8:1876–1885.

35. Kross A, McNairn H, Lapen D, Sunohara M, Champagne C: Assessment of RapidEye vegetation indices for estimation of leaf area index and biomass in corn and soybean crops. Int J Appl Earth Obs Geoinf 2015, 34:235–248.

36. Gitelson A, Merzlyak M: Remote sensing of chlorophyll concentration in higher plant leaves. Adv Spaces Res 1998, 22:689–692.

37. Xu NW, Xu S, Ehlers J: Estimating the broad-sense heritability of early growth of cowpea. Int J Plant Genomics 2009, 2009:984521.

38. Piepho H-P, Möhring J: Computing heritability and selection response from unbalanced plant breeding trials. Genetics 2007, 177:1881–8.

39. Visscher PM, Hill WG, Wray NR: Heritability in the genomics era — concepts and misconceptions. Nat Rev Genet 2008, 9:255–266.

40. Holland J, Nyquist W, Cervantes-Martinez C: Estimating and interpreting heritability for plant breeding: An update. Plant Breed Rev 2003, 22:9–112.

TABLES

Table 1 Sensor specification.

Sensor	**Platform (UAV)**	**Sensor Resolution (MP)**	**Focal Length (mm)**	**Full width at half maximum (FWHM)**	**Peak wavelength**
Canon S100	IRIS+	12.1	5.2	Blue:400-495 Green:490-550 NIR:680-760	Blue:460 Green:525 NIR:710
MultiSpec 4C	eBee Ag	1.2 (4 sensors)	3.6	Green:530-570 Red:640-680 RedEdge: 730-740 NIR:770-810	Green:550 Red:660 RedEdge:735 NIR:790
	Spectral Resolution	**wavelength accuracy**		**Wavelength Range**	
ASD spectroradiometer	<3 nm at 700 nm	±1 nm		325 nm – 1075 nm	

Table 2 Flight information using IRIS+ (multirotor) and eBee Ag (fixed wing) UASs, on May 6, 2015, at CIMMYT, Cd Obregon, Mexico. * RAW images of Canon S100 were converted to 16 bits TIFF imagery after pre-processing in Canon Digital Photo Professional software (DPP).

Camera	**Platform (UAS)**	**Flight Speed (m/s)**	**Altitude (m)**	**Percent Overlap**		**No. of Images**	**Image format**	**Spatial Resolution (cm)**
				Side	Forward			
Modified Canon S100	**IRIS+**	2	30	75%	75%	144	RAW (16 bits TIFF)*	0.8
MultiSPEC 4C	**eBee Ag**	10	48	75%	75%	40	10 bits TIFF	5

Table 3 Correlation analysis between mean GNDVI values extracted from raw Canon S100 digital number values, Calibrated Canon S100 digital number values and corresponding band equivalent reflectance (BER) GNDVI values from the spectroradiometer using different plot boundary extraction method.

	Raw Digital Numbers	**Calibrated Digital Numbers**		
	field-map based	**field-map based**	**classification**	**simple-grid**
spectroradiometer BER	**0.68**	**0.76**	**0.58**	**0.68**

Table 4 Calculated vegetation indices for each camera, based on their spectral bands and correlation between vegetation index values extracted from UAS imagery and band equivalent reflectance values from Spectroradiometer. The values from Canon S100 values are before applying modified empirical line correction method.

INDEX	**Formula**	**Correlation**	
		Canon S100	**MultiSpec 4C**
NDVI	$\frac{NIR - Red}{NIR + Red}$	-	0.33
GNDVI	$\frac{NIR - Green}{NIR + Green}$	**0.68**	0.63
RENDVI	$\frac{NIR - Red\_edge}{NIR + Red\_edge}$	-	**0.64**
ENDVI	$\frac{NIR + Green - 2 * Blue}{NIR + Green + 2 * Blue}$	0.54	-
GIPVI	$\frac{NIR}{NIR + Green}$	0.59	-

Table 5 Correlation between repeated measurements from Handheld ASD for two different vegetation indices. Four measurements were taken on each of 280 plots. To determine repeatability, the first two measurements were averaged and correlated to the average of the second two measurements on a per plot basis across all plots. The VIs presented are band equivalent indices for the Canon S100 (Green Normalized Difference Vegetation Index; GNDVI) and MultiSpec 4C (Red-edge Normalized Difference Vegetation Index: RENDVI) used in this study.

	Correlation
Green Normalized Difference Vegetation Index; GNDVI (Canon S100)	0.62
Red-edge Normalized Difference Vegetation Index; RENDVI (MultiSpec 4C)	0.88

Table 6 Broad-sense heritability in 11 trials for vegetation indices and grain yield. The VIs derived from the Canon S100 had a higher heritability than the MultiSpec 4C for nine out of eleven trials (shown in bold font).

Trial Name	Broad-sense Heritability (H^2) Vegetation Indices Canon S100 (GNDVI)	MultiSpec 4C (RENDVI)	Grain Yield
EYTBWBLHT_01	**0.89**	0.84	0.66
EYTBWBLHT_02	0.90	0.90	0.91
EYTBWBLHT_03	0.84	**0.90**	0.78
EYTBWBLHT_04	**0.87**	0.70	0.75
EYTBWBLHT_05	**0.81**	0.80	0.82
EYTBWBLHT_06	**0.73**	0.66	0.80
EYTBWBLHT_07	**0.83**	0.70	0.85
EYTBWBLHT_08	**0.64**	0.61	0.86
EYTBWBLHT_09	**0.78**	0.64	0.87
EYTBWBLHT_10	**0.66**	0.57	0.65
EYTBWBLHT_11	**0.72**	0.57	0.74

FIGURES

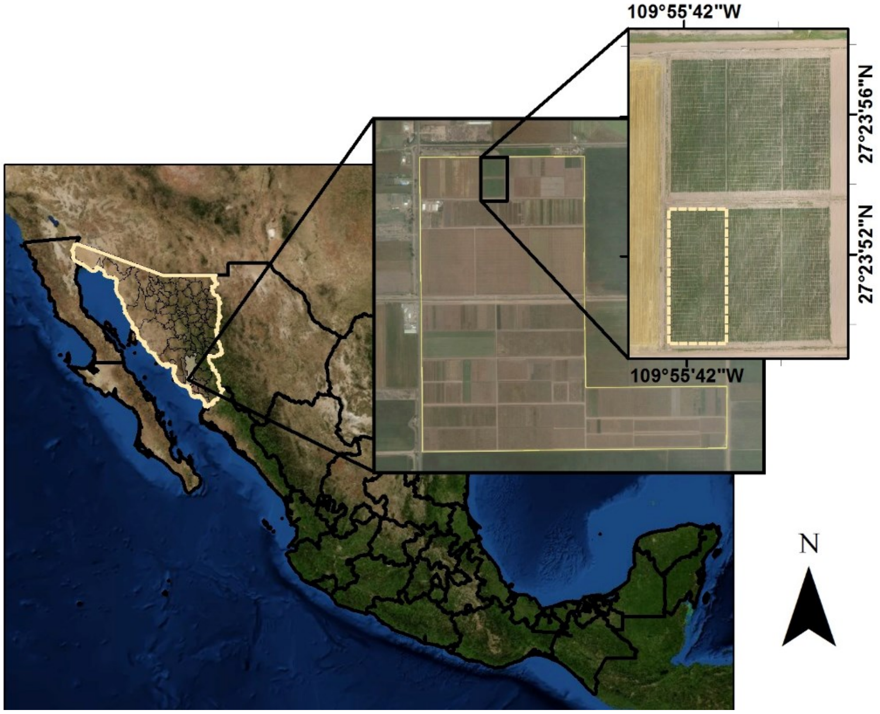

Figure 1 Location of the study area with late sown heat stress wheat trials in 2015 on the Norman E Borlaug Experiment Station at Ciudad Obregon, Sonora.

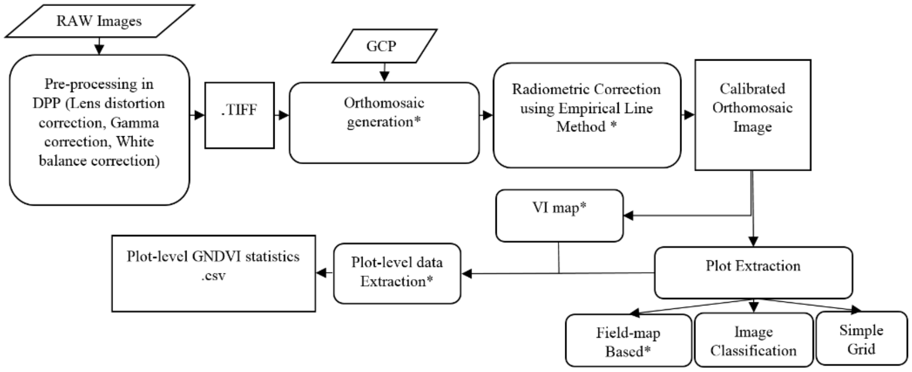

Figure 2 Image processing workflow for the low cost UAS imaging system. The developed pipeline steps are as follows: Image pre-processing using DPP software, Orthomosaic Generation using Python scripting in PhotoScan, Image radiometric correction using empirical line method commonly used for satellite imagery, Extraction of wheat plot boundary, and Calculation of different VI's. *Designates steps done using Python script

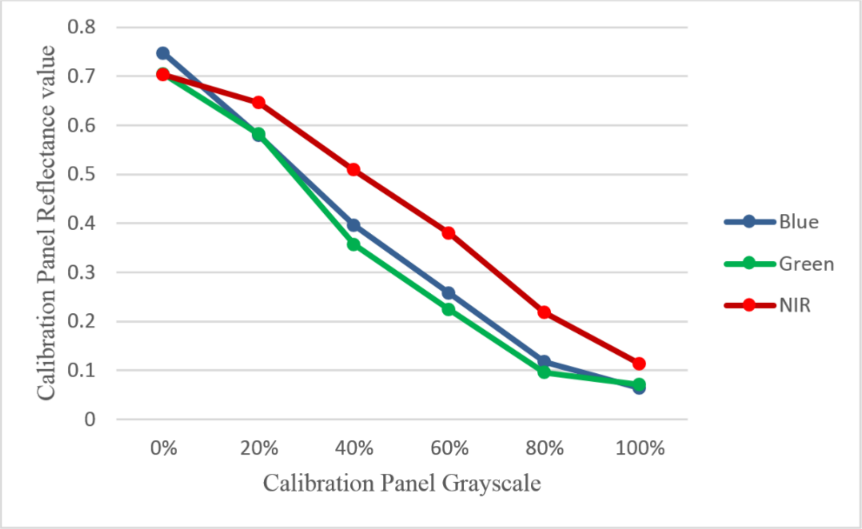

Figure 3 Empirical observation of non-linear relationship between percent gray values of the calibration panel and their corresponding mean reflectance values at the spectral region of Canon S100 wavebands (B: 400-495, G: 490-550, NIR: 680-760).

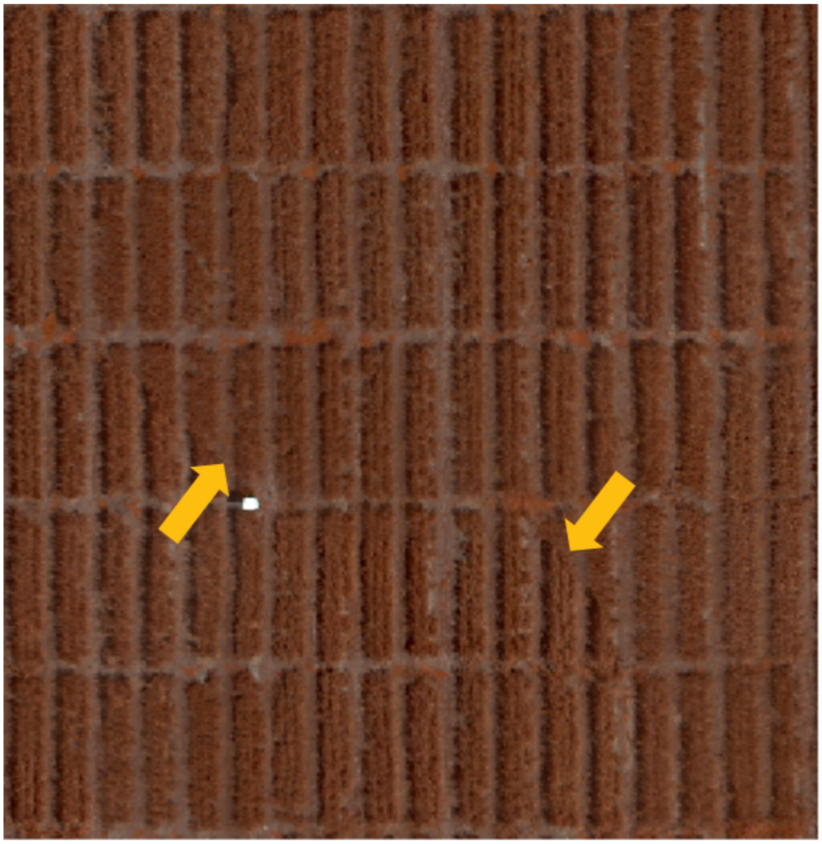

Figure 4 An example of artifact in the orthomosaic generated by Mosaic blending method from IRIS+ aerial imagery. The yellow arrows point to two locations in the orthomosaic where artifacts from merging different original images are evident.

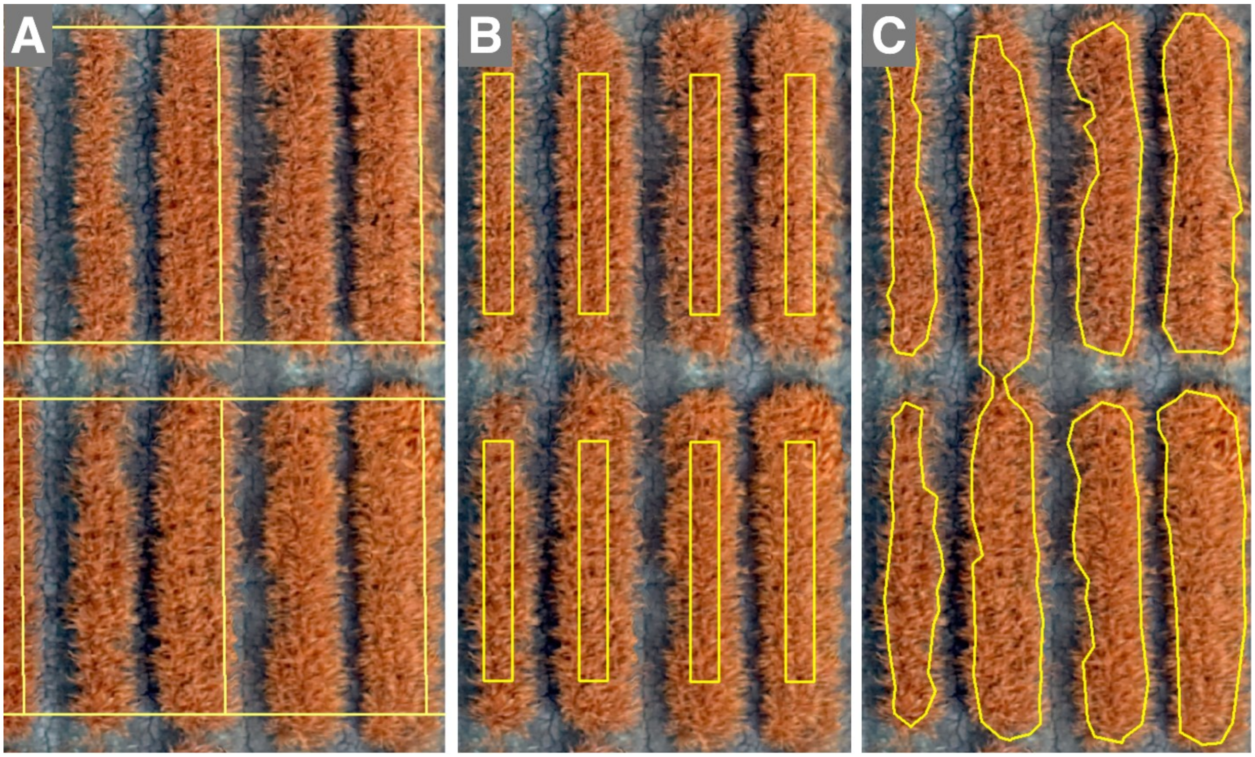

Figure 5 Results of different plot extraction method overlay on a subset of plots from IRIS+ calibrated orthomosaic. a) simple-grid plots, b) field-map based method, c) image classification approach and an example of misclassification; this example confirms the need of post processing for image classification method.

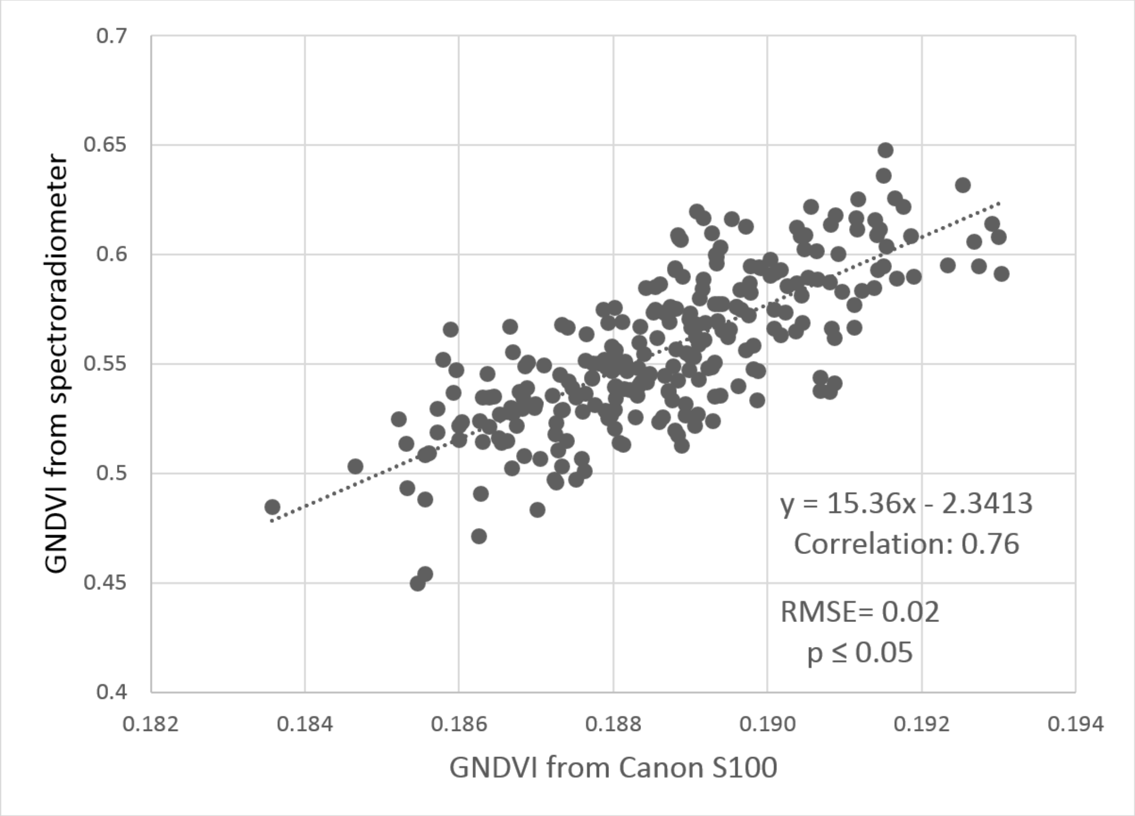

Figure 6 Linear relation between GNDVI from Canon S100 and BER GNDVI from spectroradiometer. Sample plot GNDVI values were extracted from calibrated orthomosaic of Canon S100 imagery, IRIS+ and band equivalent GNDVI for Canon S100 camera calculated from ASD spectroradiometer readings for 280 sample plots.

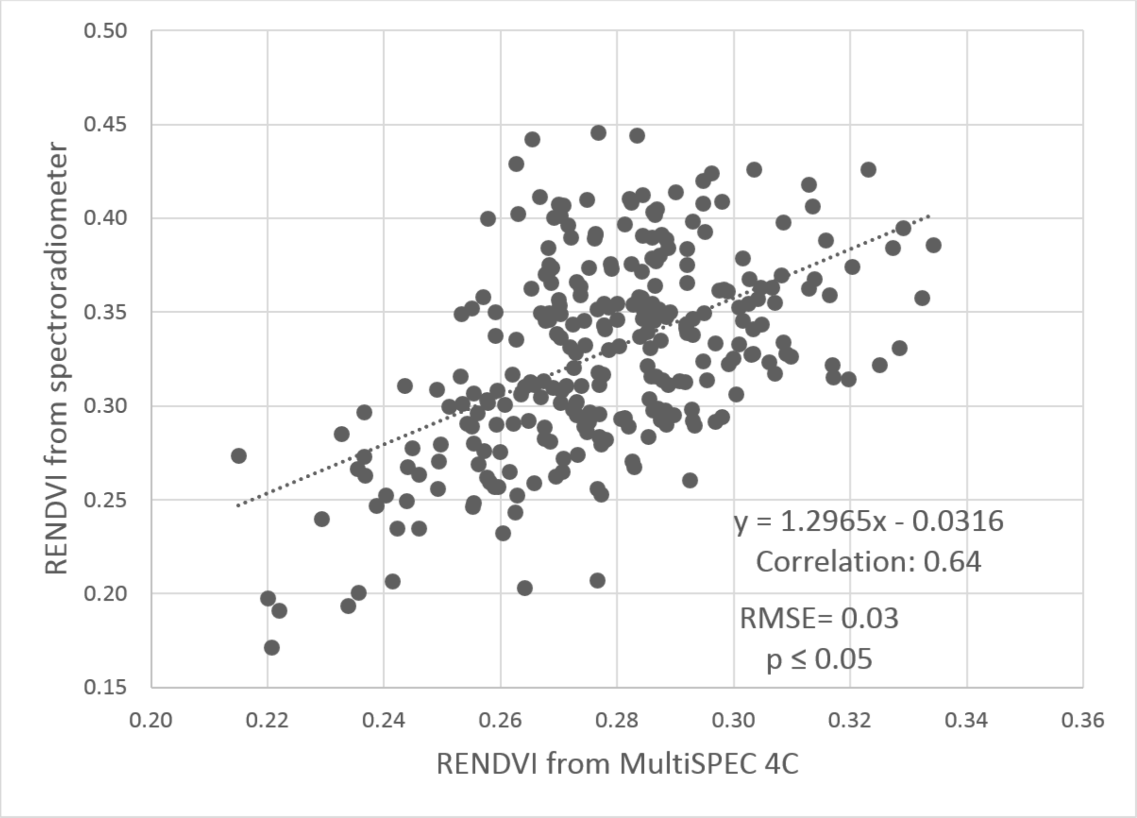

Figure 7 Scatterplot of the plot-level RENDVI from MultiSpec 4C imagery vs spectroradiometer. Plot-level RENDVI were extracted from orthomosaic generated from MultiSPEC 4C camera imagery using field-map based plot extraction method, and Band equivalent RENDVI for Spec 4C calculated from spectroradiometer reading for 280 sample plots.

Chapter 3 - Application of geographically weighted regression to improve grain yield prediction from unmanned aerial system imagery

A chapter to be submitted to the Crop Science journal as:

Atena Haghighattalab[1], Jared Crain[2], Suchismita Mondal[3], Jessica Rutkoski[3,4] , Ravi Prakash Singh[3], and Jesse Poland[5*]

[1] Department of Geography, Kansas State University, Manhattan, KS, 66506, USA

[2] Department of Plant Pathology, Kansas State University, Manhattan, KS 66506, USA

[3] International Maize and Wheat Improvement Center (CIMMYT), Int. Apdo. Postal 6-641, 06600, Mexico D.F.

[4] International Programs of the College of Agriculture and Life Science, Cornell University, Ithaca, NY 14853, USA

[5] Wheat Genetics Resource Center, Department of Plant Pathology and Department of Agronomy, Kansas State University, Manhattan, KS 66506, USA

Abbreviations:

BNDVI, blue normalized difference vegetation index; DEM, digital elevation model; DSM, digital surface model; DTHD, days to heading; DTM, digital terrain model; ENDVI, enhanced normalized difference vegetation index; EYT, elite yield trials; FWHM, full-width at half maximum; GCP, ground control point; GIPVI, green infrared percentage vegetation index; GNDVI, green normalized difference vegetation index; GWR, geographically weighted regression; HTP, high-throughput phenotyping; NDVI, normalized difference vegetation index;

NIR, near infrared; UAV unmanned aerial vehicle; UAS, unmanned aerial system; VI, vegetation index

ABSTRACT

Phenological data such as plant height are important assessments of the in-season growth of crops, though this assessment is generally limited by the availability of spatial and temporal data during the growing season. Unmanned aerial systems (UAS) have the potential to provide high spatial and temporal resolution for phenotyping tens-of-thousands of small plots under field conditions without requiring substantial investments in time, cost, and labor. Thus, there is considerable interest in implementing UAS as a rapid screening tool in crop breeding programs.

The primary objective of this research was to determine whether an accurate remote sensing based method could be developed to monitor plant growth and estimate grain yield using aerial spatio-temporal imagery in small plot wheat nurseries. We used a modified consumer grade camera mounted on a low-cost unmanned aerial vehicle (UAV) to obtain blue, green and near-infrared imagery. The UAS was deployed multiple times throughout the growing season in Elite Yield Trials in irrigated and drought-stressed environments at the International Maize and Wheat Improvement Center (CIMMYT) station in Ciudad Obregon, Mexico. We assessed data quality and evaluated the potential to predict grain yield on a plot level by examining the relationships between information derived from UAS imagery and the final measured grain yield.

Using geographically weighted (GW) models, we predicted grain yield for both drought and irrigated environments. The relationship between measured phenotypic traits derived from imagery and grain yield was highly correlated (r=0.74 and r=0.46 ($p < .001$) for drought and irrigated environments respectively). Residuals from GWR were much lower and less spatially dependent than the standard method of best linear unbiased estimators suggesting the superiority of spatially corrected models. These results show that image based vegetation indices collected from high-throughput UAS imagery can be used to predict grain yield and subsequently used for selection decisions and to improve genomic prediction models.

INTRODUCTION

Wheat is a primary staple crop throughout the world, with a total projected production of 727 million tons in 2016 (Office of the Chief Economist 2016). Due to the emergence of more aggressive pests and diseases, shortage of available water resources, lack of fertile soil, and climate change, wheat production is projected to fall behind the increasing demand (Ray et al. 2013). With limited options to increase the amount of land under production, it is generally agreed that increasing crop yield per unit area, rather than expanding cultivated land area, is needed to meet the world demand for wheat by 2050 (Muir et al. 2010; Foley et al. 2011). Unfortunately, the rate of genetic increase is currently estimated at 1% or less (Reynolds et al. 2012), while a rate of 2% or more is needed to meet the projected targets (Ray et al. 2013).

Historically, large advances in grain yield have been achieved within breeding programs. However, studies have shown that traditional breeding programs cannot currently increase crop yield at a sufficient pace to meet growing demands (Reynolds et al. 2009; Tester & Langridge

2010). Traditional phenotypic selection involves the use of manual data collection that is time-consuming, labor-intensive, expensive and often burdensome when making selections in large populations. While there have been little changes in phenotypic tools and evaluation methods (White et al. 2012), astonishing advances over the last 5-10 years have occurred in sequencing technology resulting in many advanced tools and methods to assess genotypes and improve plant breeding techniques (Cobb et al. 2013; Elshire et al. 2011; White et al. 2012). The grand challenge remains in measuring plant phenotypes with the same speed and precision as possible for observing the genome leading to active innovation in field-based high-throughput phenotyping (HTP) platforms.

HTP platforms could provide the keys to connecting genotype to phenotype by increasing the capacity, efficiency, and precision of evaluating large plant populations. HTP can maximize the population sizes screened for desirable traits in breeding nurseries. An increase in population size enabled by HTP increases the probability of identifying valuable traits and the genetic basis of those traits. This enables breeding programs to achieve a higher capacity for genetic gain (Poland 2015; Reynolds & Langridge 2016; Goggin et al. 2015).

HTP is also expected to increase the precision and accuracy with which these traits can be measured compared to manual measurements (Goggin et al. 2015; White et al. 2012). The emphasis on high dimensionality, the need for automation and more non-destructive sampling techniques in general, necessitates that HTP platforms often rely on imaging to measure plant phenotypes (Goggin et al. 2015). One emerging technology allowing plant breeders to screen large numbers of genotypes reliably is unmanned aerial systems (UAS). The main advantage of

UAS over traditional manual approaches is the ability to cover an entire experiment area in a very short time, enabling researchers to monitor larger fields with higher temporal resolution and higher spatial resolution during the growing season.

Different imaging systems are being used on unmanned aerial vehicle (UAV) phenotyping platforms making them capable of generating various measurements useful for plant breeding programs (Liebisch et al. 2015; Deery et al. 2014; White et al. 2012). High resolution multispectral cameras can be used to produce 3D models of the experiment area resulting in the extraction of plant height using a digital elevation model (DEM) (Feng et al. 2015; Rosnell & Honkavaara 2012). Other sensors include hyperspectral and thermal cameras that can be used to investigate different vegetation indices (VIs) and their relation to crop biomass and yield (Hruska et al. 2012).

Several spectral reflectance measurements and VIs have shown a strong relationship to plant health and crop growth. From this, remote sensing has proven to be a valuable tool for estimating crop yields in advance of harvest at an affordable cost. One of the most common VIs, the normalized difference vegetation index (NDVI), has been used by researchers for crop yield predictions since the 1980's (Teal et al. 2006; Singh et al. 2001; Sultana et al. 2014; Wang et al. 2014). In a study conducted by Salazar et al. (Salazar et al. 2007) a strong correlation was found between winter wheat yield and NDVI extracted from satellite imagery during the critical period of winter wheat development and productivity occurring during April to May in Kansas. Grain-yield prediction using remote sensing has been extensively studied in cereal crops, such as wheat, using satellite imagery (Prasad et al. 2006; Manjunath et al. 2016; Mkhabela et al. 2011;

Salazar et al. 2007) or ground-based platforms (Rischbeck et al. 2016; Raun et al. 2001). However, little work has been conducted using proximal sensing, such as UAS imagery platforms.

The use of physiological selection criteria to predict grain yield is an indirect breeding approach suggested in wheat research (M. a. Babar et al. 2006; Crain et al. 2016; Rutkoski et al. 2016). VIs have been widely studied as the potential tool to differentiate genotypes for yield under different environmental growing conditions such as irrigated and non-irrigated (M. A. Babar et al. 2006; Araya et al. 2013; Arnold et al. 1995; You et al. 2013). Additionally, several studies have examined how yield-enhancing traits, such as stay-green, can be used as a predictor of grain yield using spectral responses (Lopes & Reynolds 2012). Lopes et al. studied temporal NDVI data from grain fill to maturity to improve understanding of genotypic stay-green variation. In this study, they found that stay-green variables explained 30% of yield variability in multiple regression analysis, although the cumulative effect that stay-green variables provide, together with other traits may allow for additional insights to be gained about plant health and final grain yield.

Data derived from HTP can provide deeper and broader insight about the crop than what breeders are accustomed to having available. With the addition of georeferenced and spatial data inherent in HTP and imagery, researchers can utilize tools not traditionally used in the area of plant breeding. The purpose of this research is to evaluate the performance of geographically weighted models in predicting grain yields at plot level in breeding nurseries. The Foundation of geostatistical rationale is the understanding that spatial data, information about the locations and shapes of geographic features (wheat plots) and the relationships between them, stored as coordinates and topology, will vary across a field (Mitchell 2005). Regression-based models mostly ignore this assumption, which could potentially impact the accuracy of prediction models.

A typical linear regression model follows:

$$y_i = \beta_0 + \sum_{j=1,m} \beta_j x_{ij} + \varepsilon_i \quad (1)$$

With y_i is the ith observation of the dependent variable, $x_{ij}$the ith observation of the jth independent variables, and ε_i the residual that is identically and independently distributed.

When applied to spatial data, this model assumes a stationary spatial process; spatially consistent relationships between the dependent variable and each explanatory variable across the field. It should be noted that there are two types of stationarity; strong and weak. Strong stationarity requires that the distribution of the regionalized variable Z(x) is independent of location x. This implies that the mean, variance, and all other distribution parameters are the same, everywhere in the field. Second-order stationarity, also known misleadingly as the 'weak-stationarity' assumption, requires that the expected value (i.e. the mean, and the variance) is the same at all the locations (Myers., 1989).

Typical linear regression produces one single model for all parts of the study area. Field trials, however, are inherently spatial, often varying non-randomly across the field, which could impact the accuracy of these models. Geographically weighted regression (GWR) is a local statistical approach to model spatially heterogeneous processes, which could be applicable to field trials. GWR is used to analyze spatial nonstationarity; when the extent of relationships among variables differs from location to location (Brunsdon et al. 1996; Lu, Charlton, et al. 2014; Fotheringham et al. 2002). In this approach, unlike other regression models, the spatial non-stationary relationship is assumed and is tested, based on Tobler's first law of geography: "everything is related to everything else, but near things are more related than distant things" (Tobler 1970). GWR allows the relationships to vary over space, and extends the traditional regression framework of equation (1) by allowing local variations in rates of change so the coefficients in the model are no longer global estimates but are specific to a location i. This is the core of GWR, in the linear form:

$$y_i = \beta_{i0} + \sum_{j=1,m} \beta_{ij} x_{ij} + \varepsilon_i \quad (2)$$

where β_{ij} is the value of the jth parameter at location i. Instead of remaining the same everywhere, $\beta_{\bullet j}$ now varies in terms of the locations (i) (Mennis 2006; Brunsdon et al. 1996; Lu, Charlton, et al. 2014; Fotheringham et al. 2002).

In the context of growing interest in UASs applied to precision agriculture studies, we evaluated the relationship between the data extracted from UAS imagery, including green NDVI, blue NDVI, enhanced NDVI, Green Infrared Percentage Vegetation Index (GNDVI, BNDVI, ENDVI, and GIPVI), and plant height during the growing season to grain yield. Using the extracted data, we evaluated the application of spatio-temporal UAS imagery to predict within-season grain yield in a large international wheat breeding program using statistical methods based on experimental design and GWR.

MATERIALS AND METHODS

Study Area

The study was conducted at Norman E. Borlaug Experiment Station at Ciudad Obregon, Sonora, Mexico, in two different growing environments drought and irrigated. The genetic materials were advanced breeding lines in the Elite Yield Trials (EYT) of the CIMMYT bread wheat breeding program. The experiment consisted of 280 advanced wheat lines distributed in 10 trials, with each trial consisting of 28 entries and two checks. Each trial was arranged as an alpha lattice design with three replications and six blocks. The different environments were based on mega-environments which are major wheat growing regions that experience similar growing environments, with the chosen environments (irrigated and drought) representing approximately 32 and 10 million ha worldwide respectively (Braun et al. 1996). The plot size for each experimental unit in irrigated trials was 2.8 m long and 1.6 m wide (plot area = 4.48 m2) sown on two 0.8 m wide raised beds with two rows per bed, whereas plots in drought trials were 4 m long and 1.3 m wide (plot area = 5.2 m2) sown on flat land as 6 rows 18 cm apart with 40 cm interplot spacing. The drought trial was sown at the optimum planting date with minimal irrigation throughout the season using drip tape. The irrigated environment represents an optimal planting date (mid-November) with optimal flood irrigation throughout the growing season. During the crop season, the drought environment received 180mm of irrigation, and the irrigated environment received 500mm of water. Fertilizer and pesticide control were similar in both environments.

Platforms and Cameras

High-throughput phenotypic data from a UAS was collected as previously described by Haghighattalab et. al (Haghighattalab, González Pérez, et al. 2016). We used a consumer grade

Canon S100 camera modified by MaxMax (LDP LLC, Carlstadt, NJ 07072, USA, www.maxmax.com) to Blue-Green-NIR (400-760nm), which was mounted on a low-cost UAV, (IRIS+, 3D Robotics, Inc, Berkeley, CA 94710, USA). The bandwidth of the modified camera, based on the wavelength (nm) and quantum efficiency diagram reported by MaxMax are summarized in Table 1. For further analysis, we calculated full width at half maximum (FWHM) for each band. The FWHM is the range of wavelengths (i.e. bandwidth) where the filter transmits half of light at the peak.

Ground Control Points and Reflectance Calibration Panel

To geo-reference the aerial images, a total of 13 GCPs were distributed across each field at the beginning of the season. The GCPs coordinates were measured with a Trimble R4 RTK GPS that has a horizontal accuracy of 2.5 cm and a vertical accuracy of 3.5 cm. These targets were maintained throughout the crop season to enable the overlay of measurements from multiple dates. The GCPs were designed as coded targets (printed as circles with black and white segments) on 25 cm x 25 cm square white metal sheets and mounted on a 50 cm post to provide easy identification of GCPs in the image processing software. Six white 30 cm x 30 cm square ceramic tiles mounted on 10 cm post were also used to have a variety of heights in GCPs in order to increase the accuracy of height extraction analysis.

To enable consistent analysis of extracted data from aerial imagery across multiple days, we placed a calibration panel in the field before each flight. This foldable panel consisted of six individual 7 mm thick lightweight plywood panels with levels of gray from 0% being white and 100% being black and were attached using metal hinges. Using a handheld spectroradiometer

(ASD Inc., Boulder, CO) on a sunny day, the spectral reflectance of these panels were measured at a fixed altitude of 50 cm from five different angles. We also used this panel for white balance adjustment of the raw imagery captured by our consumer grade camera.

Field Data Collection

Grain harvested by using a small plot combine at the end of the season and total plot yield recorded in kg per plot. For the irrigated environment, manual measurements for plant height were recorded for the first replicate in each trial, and for all plots in the drought environment. These measurements were taken as the distance from the ground to the average top of the terminal spikelet for a representative plant, usually from the middle of the plots. Before measurement, culms were manually pulled up to the vertical position if they were lodged (Bell et al. 1994).

For each environment, aerial imagery was taken at multiple time points using the UAV phenotyping platform (IRIS+ and a modified Canon S100 camera) during the growing season, with observation days spaced at approximately seven-day intervals, depending on the weather condition. All images were taken in RAW format (.CR2) to avoid loss of image information. An overview of each day of UAS observation is summarized in Table 2.

HTP Image Processing

For each experiment we collected three sets of observations from heading through senescence (Zadoks et al. 1974). We used the semi-automated data analysis pipeline presented in Haghighattalab et al. (Haghighattalab, González Pérez, et al. 2016) to analyze each dataset and extracted plot level phenomics values. Image processing was primarily conducted using Python scripts, open source software QGIS (http://qgis.osgeo.org) and Agisoft PhotoScan package (Agisoft LLC, St. Petersburg, Russia, 191144) (Haghighattalab, Perez, et al. 2016).

To generate plot level values for VIs and plant height, we used the image processing developed by Haghighattalab et al. (Haghighattalab, González Pérez, et al. 2016). In summary, HTP data processing, for each time point of data collection, included the following steps:

1) raw image pre-processing
2) Photo alignment
3) importing GCPs and geo-referencing
4) optimize GCP alignment
5) constructing dense point cloud
6) classifying data within the dense point as plant or soil
7) building digital elevation model using classified point cloud
8) forming orthomosaic image using two different blending methods
9) generating orthomosaic and DEM
10) calculation of various VIs, and plant height
11) plot-level data extraction

Due to the modified Canon S100 available bandwidth, the calculated VIs were limited to GNDVI, BNDVI, ENDVI, and GIPVI. The formulas used to calculate these indices are presented in Table 3.

Plant Height Extraction

PhotoScan generates a dense point cloud based on the estimated camera positions. The program also calculates depth information for each photo to be combined into a single dense point cloud (Agisoft LLC 2016). We generated dense point cloud with medium accuracy. To extract plant height, we produced both the digital terrain model (DTM) and the digital surface model (DSM), with plant height being calculated as the difference between the two models (equation 3):

$$\text{Plant Height} = \text{DSM} - \text{DTM} \quad (3)$$

The generated dense point cloud includes everything that can be seen in the images, pixels from the ground, vegetation, and any other artifacts or noise. PhotoScan offers two options of dense point cloud classification: 1) automatic classification of the points into two categories – ground points and other, 2) manual selection of a group of points to be placed in a particular class from the standard list known for LIDAR data, such as vegetation, water, or road surface. Three parameters control automatic ground point classification: maximum angle, maximum distance, and maximum cell size (Agisoft LLC 2016). Point cloud classification provides ways to customize the DEM generation step as the software allows choosing types of objects within the scene to be reconstructed and indicate the corresponding point class as a source data for DEM generation. For example, DEM reconstruction based on ground points only, allows users to export DTM (as opposed to DSM, based on the complete dense point cloud, excluding the artifacts and noises) (Agisoft LLC 2016).

In our plot imagery, we reduced the default values for maximum angle and maximum distance parameter values since the height for crops are considerably lower than heights of other objects like buildings. To estimate plant height, we allowed automatic classification of ground points and then classified the vegetation points manually, generating DTM and DSM for each dataset. We defined training sets for classes of ‘ground’, ‘low vegetation’, and ‘high vegetation’ by sampling the points. Using the classified point cloud, we extracted the DTM by only using ground points, and the DSM by using data assigned to the vegetation points. For a small field, the generated classified point cloud can be used to calculate plant height directly. However, the point cloud exported from PhotoScan are very large files and for large wheat breeding nurseries, as we used in our study, we used the generated DEM.

Using our custom field map based method, we extracted two plot boundaries for each field. One plot boundary was buffered to avoid pixels outside the plot, and was used for the DSM extraction, as we are only interested in values reflected from wheat plants. The second plot boundary was extended to have the DTM values of the ground surrounding the wheat plots. We calculated mean, and standard deviation (SD) for DSM, and lower quantile for DTM. We calculated height for each plot as the difference between the mean values of DSM and lower quantile values of DTM as these values would represent the lowest elevation point in the DTM.

Using the classified DEM, we generated orthomosaic using both blending methods (average and mosaic). In the average mode, the brightness values of the final orthomosaic is the average of all the overlapping images, while mosaic mode only uses images where the pixel in question is located within almost nadir view (Haghighattalab, González Pérez, et al. 2016; Agisoft LLC 2016).

After calibrating each orthomosaic data set for each environment using empirical line method, we generated VI maps using Python scripting in QGIS as described in our developed pipeline (Haghighattalab, González Pérez, et al. 2016; Smith & Milton 1999). We calculated statistical values for each plot for each day of data that included the minimum, mean, maximum, and standard deviation for both blending methods.

HTP Data Analysis

Broad-sense Heritability

Within environment and trial, we calculated broad-sense heritability, commonly known as repeatability (Piepho & Möhring 2007), for extracted VIs measured on individual dates, and grain yield.

To estimate heritability, we performed a two steps process where we first calculated the plot-level value for HTP measurements and then fit a mixed model for replication, block, and genotype as random effects.

Broad-sense heritability for each trait within trial within environment was calculated from equation 4 (Holland et al. 2003).

$$H^2 = \frac{\sigma^2_{genotypic}}{\sigma^2_{genotypic}+\frac{\sigma^2_{error}}{nrep}} \tag{4}$$

Where $\sigma^2_{genotypic}$is genotypic variance, σ^2_{error} is error variance, *nrep* is the number of replicates in the trial (*nrep*=3). The *lme4* R package was used for all mixed model analysis (Bates et al. 2014).

Parameter Estimation

Within each environment and trial, to estimate genetic values for traits measured across multiple dates, we estimated best linear unbiased estimates (BLUEs) for each genotype using the following mixed model:

$$y_{ijk} = \mu + g_i + r_j + b_{k(j)} + \epsilon_{ijk} \left(\begin{smallmatrix} i=1 \ldots nlines \\ j=1 \ldots 3\ replicates \\ k=1 \ldots 6\ blocks \end{smallmatrix} \right) \qquad (5)$$

Where y_{ijk} is the phenotype observation for each trait, μ is the mean value of the population; g_i is the fixed genotype effect of entry i, r_j is the random effect for the j replicate distributed as i.i.d. $r_j \sim N(0, \sigma_j^2)$, $b_{,k(j)}$ is the random effect for the m block nested within replicate distributed as i.i.d. $b_{k(j)} \sim N(0, \sigma_k^2)$, and $\boldsymbol{\epsilon}_{ijk}$is the residual distributed as *i.i.d.* $\epsilon_{ijk} \sim N(0, \sigma_\epsilon^2)$.

We calculated BLUEs for grain yield, DTHD, all the VIs, and plant height. We assessed the height measurements by calculating the correlation between manual height measurements and extracted UAS imagery measurements.

Because the phenotypic BLUEs were highly correlated we used principal component regression to evaluate the relationship between phenotypic values and grain yield. Principal component regression is a popular technique that can adequately account for multiple variables that may have varying levels of correlation between variables (Mevik & Wehrens 2007). Within each environment, we fit a principal component regression model using the multi-temporal and multi-VI (ENDVI, BNDVI, GIPVI, GNDVI) to observed grain yield. The *pls* R package (Mevik et al. 2013) was used for all principal component model development. We validated the prediction model using a 10-fold cross validation with the accuracy of prediction reported as the correlation of the predicted values compared to the observed values.

Geographically Weighted Modeling

By mapping yield and vegetation indices from both growing conditions, we were able to determine the presence of spatial patterns (Figure 8). This led us to develop a geographically weighted model to explore changing spatial relationships between grain yield and measured phenotypic traits. An important extension of GWR is its semiparametric construction by combining globally fixed and geographically varying coefficients (Equation 6) (Lu, Harris, et al. 2014).

$$y_i = \sum_k \beta_k(u_i, v_i)x_{k,i} + \sum_l \gamma_l + z_{l.i} + \varepsilon_i \tag{6}$$

Where y_i, $x_{k,i}$, and ε_i are, respectively, grain yield, kth phenotypic trait, and the Gaussian error at location i; (u_i, v_i) is the x-y coordinate of the ith location; and coefficients $\beta_k(u_i, v_i)$ are varying conditionals on the location. The global term, $z_{l.i}$ is the lth phenotypic trait with a fixed coefficient γ_l (Nakaya 2016).

In this approach, a moving window weighting technique is used, where local models at both sampled and unsampled locations are calibrated. All neighboring observations, for an individual sample point, are weighted based on a distance decay kernel function, and the model is fit to this weighted data. The key to GW modeling is the weighting matrix, which sets the spatial dependency in the data (Lu, Harris, et al. 2014). There are three elements in defining this matrix: the distance metric (in our case, the distance between observations is calculated as the distance between polygon centroids); the type of kernel weighting function; and the kernel weighting function’s bandwidth which controls the size of the moving window (Mennis 2006). The scope of these parameters and details on GW modeling are outlined in Fotheringham et al.,

(2002) (Fotheringham et al. 2002). For GW modeling, we used the GWmodel package in R to investigate spatial relationships among the numerous phenotypic observations and grain yield (Lu, Harris, et al. 2014). We obtained accuracies of GW prediction model ability for both environments using 10-fold cross-validation technique.

RESULTS and DISCUSSION

Image Processing for HTP Data

To evaluate the potential of UAS for within season grain yield prediction in wheat breeding programs, we deployed a low-cost, consumer-grade UAV phenotyping platform at multiple times throughout the growing season in two different growing environments (Table 2). We processed all the imagery taken at various dates using a semi-automated pipeline (Haghighattalab, González Pérez, et al. 2016). Image processing included converting raw imagery to TIFF format, georeferencing, point cloud generation, DEM and orthomosaic generation, and plot level data extraction. We examined how the choice of mosaic or average orthomosaics generation affected the results. Additionally, our pipeline calculated the standard summaries for each plot of minimum, maximum, mean, range, and standard deviation of each vegetation index. The pipeline made efficient use of the data that was generated. For a regular flight 100 photos were taken resulting in 1.35 GB of raw data, processing time averaged 3 hours per flight on a 16 GB RAM single core processor. While efficient, this highlights one of the needed areas of research to reduce processing time to allow users to collect data and rapidly analyze or even process in real-time.

Plant Height Measurements

To evaluate the suitability of using the UAS phenotyping platform to monitor plant height, we calculated the pairwise correlation using manual measurements for the drought and irrigated environments compared to the height extracted from UAS (n=900 for drought and n=300 for irrigated). Using the initial data, it was apparent that there were outliers in both the irrigated and drought environment. Using the SD of the height values calculated from the DEM for both environments, we set a minimum height threshold to identify and remove lodged plots. After removal of plots with height lower than 60cm for drought environment, and 80cm for irrigated environment there was a significant correlation between the DEM and manual measurements of height with correlations of r=0.7 and r=0.56 for irrigated and drought respectively (Figure 9).

While we found a significant association between manual measurements and UAS height measurement, we believe the results for height could be improved with an elevation soil map taken before vegetation begins growing. This would be a more accurate DEM map of the area and allow for more precise height extractions from the DTM. Additionally, we found that relying on the minimum values or the lower quantile values of DTM extracted from each plot of wheat are more challenging for irrigated environment since they are planted in bed. In the bed planting, while height should be calculated from the center of the bed, digital extraction may include the wheat plants between the bed which may be several centimeters in difference compared to the ground elevation. Another option may be to use RGB images which would have higher accuracy compare to the images captured by the modified NIR cameras.

Reason for lower correlation with manual measurements for drought environment compare to irrigated, could be due to the very close values of plant heights in this environment; the range of height for drought falls between 68 cm and 84 cm for 900 observed plots, while this range for irrigated environment based on the manual measurement was 91 cm-122cm for the 300 observed plots. With the vertical accuracy of RTK GPS in this study (~3 cm), extracting plant heights that were very close to each other in values can be more challenging.

Grain Yield Prediction using Principal Component Regression

To evaluate the potential of UAS phenotyping platforms to quantify grain yield we used principal component regression (PCR) to develop models for each environment. This technique provides a method to adequately address the correlation between variables, as many of the measured vegetation indices exhibited high levels of correlation. Using the estimated BLUEs and a 10-fold cross validation scheme, the correlation between the predicted grain yield and observed grain yield was r=0.48 and r=0.32 for drought and irrigated environments, respectively (Figure 10).

Grain Yield Prediction using GWR

Because plant breeding trials are inherently spatial in nature, we assessed using geographically weighted regression to evaluate grain yield. We used a subset of the extracted VIs for variables within the GWR model. The GWR model provides basic variable selection for accounting for correlated variables that was typical of our VIs. The data were then entered into the GW modeling using a variable bandwidth setting that minimizes the AIC. The adaptive bandwidth approach was chosen to account for the spatial variation in the size of the wheat plots, and hence the density of plots centroids (Mennis 2006).

Within each environment, we used a 10-fold cross-validation that was repeated 1000 times to evaluate model prediction to observed grain yield (Figure 3). The average correlation between observed and predicted values was r=0.74 and r=0.46 ($p < .001$) for the drought and irrigated environments respectively. In addition to having higher prediction accuracies than principal component regression, the root mean squared error was decreased from 0.36 to 0.2 for the irrigated environment and 0.39 to 0.14 for the drought environment.

Environment Prediction

Using both principal component regression and GWR, we observed similar trends. In general, GWR resulted in higher prediction accuracies compared to principal component regression, which would be expected as GWR takes into account the neighborhood (local environment) around the plot. This higher prediction was observed in both environments for GWR. However, both PCR and GWR followed a similar trend of high predictive ability in the drought environment with less predictive power in the irrigated environment. Why one environment was predictive compared to the other is not clear. We examined the heritability for each observed phenotypic trait (VI's and grain yield) for each of the 10 trials in the study area. In general, heritability was high for all traits Table 4, suggesting minor environmental fluctuations. Grain yield had a larger range of variance for both irrigated and drought (H2=0.37-0.87 for irrigated grain yield trials and H2= 0.71-0.96 for drought grain yield trials), which would be expected as grain yield is the sum of the entire growing season, while daily VIs would represent a single time point of observations. While the irrigated had a larger range in heritability and lower prediction, the differences may be due to the timing of the data collection within the environments, or the ability to detect differences in genotypes that are saturating reflectance (Esfandiary et al. 2009). While our work shows that UAS phenotyping platform can be used to monitor and predict yield performance in drought, more work is needed to transfer this to the irrigated (high-yield) environment.

CONCLUSION

With the development of new sensors and imaging systems enabling parallel phenotypic measurements, HTP can advance the scope of scientific studies and expand our understanding of plants. Using a low-cost UAS, we generated spatio-temporal phenotypic data and applied a semi-automated pipeline to extract information from individual wheat plots during the growing season.

The extracted height from UAS had a high correlation with manual measurements in both environments. Although planting systems, on flat or bed, and variation in plant's height may have an effect on estimated readings, our results demonstrate that UAS can be successfully used for measuring plant height in wheat. Different VIs and canopy height were related to final grain yield. We evaluated several prediction models, with models accounting for spatial variability performing the best. In addition to predicting plant yield, our analysis highlights some of the flexibility in these methods that end users can use by modifying how data can be extracted and classified from the images. For example, dense point cloud classification provides ways to customize the DEM generation step as the software allows choosing types of objects within the scene to be reconstructed and indicate the corresponding point class as a source data for DEM generation.

Our study provides strong support of the value of UAS for predicting and evaluating several physiological traits and using this information for overall yield prediction. Application of this technology can enable plant breeders and scientists to enhance their understanding of plants, especially using types of data collected by UAS's in genetic studies and genomic prediction models. Through the implementation of in-season yield prediction in early generations of the breeding program, selection decisions could be made before harvest and only selected lines harvested from the field. Likewise, the incorporation of ‘secondary traits’ as described here has been shown to increase the prediction accuracy of genomic models when incorporated in a multivariate framework (Rutkoski et al., 2016). Overall, the rapid measurement of physiological and agronomic traits in-season for large breeding nurseries will provide breeders will additional tools meet the challenge of increasing genetic gain and delivering superior high-yielding varieties.

Acknowledgements

This work was done through the International Maize and Wheat Improvement Center (CIMMYT), Mexico and supported through the National Science Foundation - Plant Genome Research Program (IOS-1238187) and the US Agency for International Development Feed the Future Innovation Lab for Applied Wheat Genomics (Cooperative Agreement No. AID-OAA-A-13-00051).

Competing Interests

The authors declare no competing interests.

Authors' Contributions

Conceived and designed the study: RPS, and JP; Developed and Validated Methods: AH, and JC; Collected Data: AH, SM, JR, and RPS; Analyzed Data and Interpreted Results: AH, JC and JP; All authors prepared and approved the manuscript.

REFERENCES

Agisoft LLC, 2016. Agisoft PhotoScan User Manual: Professional Edition, Version 1.2. Available at: http://www.agisoft.com/pdf/photoscan-pro_1_2_en.pdf.

Araya, S. et al., 2013. Crop phenology based on MODIS satellite imagery as an indicator of plant available water content. 20th International Congress on Modelling and Simulations, Adelaide, Australia.

Arnold, J.G. et al., 1995. Chapter 8. PLANT GROWTH COMPONENT. Growth (Lakeland), (July), pp.1–41.

Babar, M. a. et al., 2006. The Potential of Using Spectral Reflectance Indices to Estimate Yield in Wheat Grown Under Reduced Irrigation. Euphytica, 150(1-2), pp.155–172. Available at: http://www.springerlink.com/index/10.1007/s10681-006-9104-9.

Babar, M.A. et al., 2006. Spectral Reflectance Indices as a Potential Indirect Selection Criteria for Wheat Yield under Irrigation. pp.578–588.

Bates, D. et al., 2014. lme4: Linear mixed-effects models using Eigen and S4.

Bell, M.A. et al., 1994. Guide to Plant and Crop Sampling: Measurements and Observations for Agronomic and Physiological Research in Small Grain Cereals,

Braun, H.-J., Rajaram, S. & Ginkel, M., 1996. CIMMYT's approach to breeding for wide adaptation. Euphytica, 92(1-2), pp.175–183.

Brunsdon, C., Fotheringham, A.S. & Charlton, M.E., 1996. Geographically Weighted Regression: A Method for Exploring Spatial Nonstationary. Geographical Analysis, 28(4).

Cobb, J.N. et al., 2013. Next-generation phenotyping: requirements and strategies for enhancing our understanding of genotype–phenotype relationships and its relevance to crop improvement. Theoretical and Applied Genetics, 126(4), pp.867–887. Available at: http://link.springer.com/10.1007/s00122-013-2066-0 [Accessed Sep 30, 2016].

Crain, J.L., Reynolds, M.P. & Poland, J.A., 2016. Utilizing high-throughput phenotypic data for improved phenotypic selection of stress adaptive traits in wheat. Crop Science.

Deery, D. et al., 2014. Proximal Remote Sensing Buggies and Potential Applications for Field-Based Phenotyping, Available at: http://www.mdpi.com/2073-4395/4/3/349/ [Accessed September 14, 2016].

Elshire, R.J. et al., 2011. A Robust, Simple Genotyping-by-Sequencing (GBS) Approach for High Diversity Species. PLoS ONE, 6(5), pp.1–10.

Esfandiary, F., Aghaie, G. & Mehr, A.D., 2009. Wheat Yield Prediction through Agro Meteorological Indices for Ardebil District. International Journal of Biological, Biomolecular, Agricultural, Food and Biotechnological Engineering, 3(1), pp.18–21.

Feng, Q., Liu, J. & Gong, J., 2015. Urban Flood Mapping Based on Unmanned Aerial Vehicle Remote Sensing and Random Forest Classifier—A Case of Yuyao, China. Water, 7, pp.1437–1455.

Foley, J.A. et al., 2011. Solutions for a cultivated planet. Nature, 478, pp.337–342.

Fotheringham, A.S., Brunsdon, C. & Charlton, M., 2002. Geographically weighted regression: the analysis of spatially varying relationships. Available at: http://www.123library.org/book_details/?id=14164.

Goggin, F.L., Lorence, A. & Topp, C.N., 2015. Applying high-throughput phenotyping to plant–insect interactions: picturing more resistant crops. Current Opinion in Insect Science, 9, pp.69–76. Available at: http://linkinghub.elsevier.com/retrieve/pii/S2214574515000334.

Haghighattalab, A., González Pérez, L., et al., 2016. Application of unmanned aerial systems for high throughput phenotyping of large wheat breeding nurseries. Plant Methods, 12(1), pp.1–15. Available at: http://dx.doi.org/10.1186/s13007-016-0134-6.

Holland, J., Nyquist, W. & Cervantes-Martinez, C., 2003. Estimating and interpreting heritability for plant breeding: An update. Plant Breeding Review, 22, pp.9–112.

Hruska, R. et al., 2012. Radiometric and geometric analysis of hyperspectral imagery acquired from an unmanned aerial vehicle. Remote Sensing, 4(9), pp.2736–2752.

Jessica Rutkoski, Jesse Poland, Suchismita Mondal, Enrique Autrique, Lorena González Párez, Josá Crossa, Matthew Reynolds, R.S., 2016. Canopy Temperature and Vegetation Indices from High-Throughput Phenotyping Improve Accuracy of Pedigree and Genomic Selection for Grain Yield in Wheat. G3 (Bethesda, Md.).

Liebisch, F. et al., 2015. Remote, aerial phenotyping of maize traits with a mobile multi-sensor approach. Plant methods, 11, p.9. Available at: http://www.pubmedcentral.nih.gov/articlerender.fcgi?artid=4365514&tool=pmcentrez&rendertype=abstract [Accessed Sep 29, 2016].

Lopes, M.S. & Reynolds, M.P., 2012. Stay-green in spring wheat can be determined by spectral reflectance measurements (normalized difference vegetation index) independently from phenology. Journal of experimental botany, pp.1–10.

Lu, B., Charlton, M., et al., 2014. Geographically weighted regression with a non-Euclidean distance metric: a case study using hedonic house price data. International Journal of Geographical Information Science, 28(4). Available at: http://dx.doi.org/10.1080/13658816.2013.865739.

Lu, B., Harris, P., et al., 2014. The GWmodel R package: Further Topics for Exploring Spatial Heterogeneity using Geographically Weighted Models. Geo-spatial Information Science, 17(2), pp.85–101.

Manjunath, K.R., Potdar, M.B. & Purohit, N.L., 2016. Large area operational wheat yield model development and validation based on spectral and meteorological data. International Journal of Remote Sensing ISSN:23(15), pp.3023–3038.

Mennis, J., 2006. Mapping the Results of Geographically Weighted Regression. The Cartographic Journal, 43(2), pp.171–179.

Mevik, B.H. & Wehrens, R., 2007. The pls package: Principal component and partial least squares regression in R. Journal of Statistical Software, 18(2), pp.1–23.

Mevik, B.-H., Wehrens, R. & Liland, K.H., 2013. pls: Partial Least Squares and Principal Component regression.

Mitchell, A., 2005. The ESRI Guide to GIS Analysis. ESRI Press, 2.

Mkhabela, M.S. et al., 2011. Crop yield forecasting on the Canadian Prairies using MODIS NDVI data. Agricultural and Forest Meteorology, 151(3), pp.385–393. Available at: http://linkinghub.elsevier.com/retrieve/pii/S0168192310003138.

Myers DE: To Be or Not to Be . . . Stationary? That Is the Question. Math Geol 1989, 21:347–362.

Muir, J.F. et al., 2010. Food Security: The Challenge of Feeding 9 Billion People. Science, 327(February).

Nakaya, T., 2016. Windows Application for Geographically Weighted Regression Modelling.

Office of the Chief Economist, 2016. World Agricultural Supply and Demand Estimates. USDA.

Piepho, H.-P. & Möhring, J., 2007. Computing heritability and selection response from unbalanced plant breeding trials. Genetics, 177(3), pp.1881–8.

Poland, J., 2015. Breeding-assisted genomics. Current Opinion in Plant Biology, 24, pp.119–124.

Prasad, A.K. et al., 2006. Crop yield estimation model for Iowa using remote sensing and surface parameters. International Journal of Applied Earth Observation and Geoinformation, 8, pp.26–33.

Raun, W.R. et al., 2001. In-Season Prediction of Potential Grain Yield in Winter Wheat Using Canopy Reflectance. Agronomy Journal, 93(1), p.131.

Ray, D.K. et al., 2013. Yield Trends Are Insufficient to Double Global Crop Production by 2050. PloS one, 8(6).

Reynolds, M. et al., 2012. Achieving yield gains in wheat. Plant, Cell and Environment, 35(10), pp.1799–1823.

Reynolds, M. et al., 2009. Phenotyping approaches for physiological breeding and gene discovery in wheat. Annals of Applied Biology, 155, pp.309–320.

Reynolds, M. & Langridge, P., 2016. Physiological Breeding. Current Opinion in Plant Biology, 31, pp.162–171. Available at: http://dx.doi.org/10.1016/j.pbi.2016.04.005.

Rischbeck, P. et al., 2016. Data fusion of spectral, thermal and canopy height parameters for improved yield prediction of drought stressed spring barley. European Journal of Agronomy, 78, pp.44–59. Available at: http://dx.doi.org/10.1016/j.eja.2016.04.013.

Rosnell, T. & Honkavaara, E., 2012. Point cloud generation from aerial image data acquired by a quadrocopter type micro unmanned aerial vehicle and a digital still camera. Sensors, 12(1), pp.453–480.

Rutkoski, J. et al., 2016. Predictor traits from high-throughput phenotyping improve accuracy of pedigree and genomic selection for grain yield in wheat. , pp.1–33.

Salazar, L., Kogan, F. & Roytman, L., 2007. Use of remote sensing data for estimation of winter wheat yield in the United States. International Journal of Remote Sensing, 28(17), pp.37–41.

Singh, S.P. et al., 2001. Relationship of wheat grain yield with spectral indices. Journal of the Indian Society of Remote Sensing, 29(1-2), pp.93–96.

Smith, G.M. & Milton, E.J., 1999. The use of the empirical line method to calibrate remotely sensed data to reflectance. Int J Remote Sens, 20. Available at: http://dx.doi.org/10.1080/014311699211994.

Sultana, S.R. et al., 2014. Normalized Difference Vegetation Index as a Tool for Wheat Yield Estimation: A Case Study from Faisalabad, Pakistan. The Scientific World Journal, 2014.

Teal, R.K. et al., 2006. In-Season Prediction of Corn Grain Yield Potential Using Normalized Difference Vegetation Index. Agronomy Journal, 98(6), p.1488. Available at: https://www.agronomy.org/publications/aj/abstracts/98/6/1488 [Accessed September 14, 2015].

Tester, M. & Langridge, P., 2010. Breeding technologies to increase crop production in a changing world. Science (New York, N.Y.), 327(5967), pp.818–822.

Tobler, A.W.R., 1970. A Computer Movie Simulating Urban Growth in the Detroit Region. Economic Geography, 46, pp.234–240.

Wang, L. et al., 2014. Field Crops Research Predicting grain yield and protein content in wheat by fusing multi- sensor and multi-temporal remote-sensing images. Field Crops Research, 164, pp.178–188. Available at: http://dx.doi.org/10.1016/j.fcr.2014.05.001.

White, J. et al., 2012. Field-based phenomics for plant genetics research. Field Crops Research, 133, pp.101–112.

You, X. et al., 2013. Remote Sensing Based Detection of Crop Phenology for Agricultural Zones in China Using a New Threshold Method. Remote Sensing, 5, pp.3190–3211.

Zadoks, J.C., Chang, T.T. & Konzak, C.F., 1974. A Decimal Code for the Growth Stages of Cereals. Weed Research, 14(6), pp.415–421.

TABLES

Table 7 Sensor specifications for each instrument used for spectral data collection.

Sensor	Platform (UAS)	Effective Pixels (MP)	Band width (nm)	Full width at half maximum (FWHM)
Canon S100	IRIS+	12.1	Blue:380-540 Green:460-570 NIR:650-780	Blue:400-495 Green:490-550 NIR:680-760
	Spectral Resolution	**Wavelength Accuracy**	**Wavelength Range**	
ASD spectroradiometer	<3 nm at 700 nm	±1 nm	325 nm – 1075 nm	

Table 8 Flight information using unmanned aerial system high-throughput phenenotyping platform (IRIS+ and modified Canon S100), at CIMMYT, Ciudad Obregon, Mexico, 2016.

Environment	No. of Flights	Flight Speed (m/s)	Altitude (m)	Percent Overlap of each photo		No. of Images	Spatial Resolution (cm)
				Side	Forward		
Drought	3	2	30	70%	80%	100	~0.9
Irrigated	3	2	25	70%	80%	93	~0.9

Table 9 Vegetation indices calculated for each day of data measurements using a modified Canon S100.

INDEX	**Formula**
GNDVI	$\frac{NIR - Green}{NIR + Green}$
BNDVI	$\frac{NIR - Blue}{NIR + Blue}$
ENDVI	$\frac{NIR + Green - 2 * Blue}{NIR + Green + 2 * Blue}$
GIPVI	$\frac{NIR}{NIR + Green}$

Table 10 Broad-sense heritability in 10 trials for vegetation indices and grain yield. The VIs extracted from Canon S100 at three time points during the growing season for Drought and irrigated environment. In irrigated all the VIs derived from the Canon S100 had higher heritability than the final grain yield.

Broad Sense Heritability H^2													
Drought Environment													
	March 2, 2016				**March 10, 2015**				**March 14, 2016**				
Trial #	**BNDVI**	**ENDVI**	**GIPVI**	**GNDVI**	**BNDVI**	**ENDVI**	**GIPVI**	**GNDVI**	**BNDVI**	**ENDVI**	**GIPVI**	**GNDVI**	**Yield**
1	0.94	0.93	0.93	0.93	0.94	0.93	0.89	0.89	0.89	0.85	0.94	0.94	0.88
2	0.91	0.89	0.91	0.91	0.92	0.9	0.88	0.88	0.89	0.85	0.92	0.92	0.71
3	0.93	0.91	0.94	0.94	0.94	0.95	0.88	0.88	0.86	0.82	0.94	0.94	0.85
4	0.92	0.91	0.92	0.92	0.91	0.89	0.93	0.93	0.92	0.87	0.95	0.95	0.92
5	0.89	0.87	0.94	0.94	0.9	0.89	0.91	0.91	0.95	0.93	0.96	0.96	0.96
6	0.88	0.86	0.93	0.93	0.9	0.85	0.91	0.91	0.94	0.88	0.93	0.93	0.78
7	0.96	0.95	0.97	0.97	0.93	0.92	0.88	0.88	0.87	0.82	0.94	0.94	0.91
8	0.95	0.94	0.96	0.96	0.93	0.93	0.9	0.9	0.9	0.88	0.91	0.89	0.89
9	0.9	0.86	0.96	0.96	0.93	0.91	0.94	0.94	0.89	0.85	0.94	0.94	0.9
10	0.91	0.89	0.94	0.94	0.93	0.91	0.93	0.93	0.94	0.88	0.96	0.96	0.92
Mean	0.92	0.90	0.94	0.94	0.92	0.91	0.91	0.91	0.91	0.86	0.94	0.94	0.87
Range	0.88-0.96	0.86-0.95	0.91-0.97	0.91-0.97	0.9-0.94	0.85-0.95	0.88-0.94	0.88-0.94	0.86-0.95	0.82-0.93	0.91-0.96	0.89-0.96	0.71-0.96
Irrigated Environment													
	March 10, 2016				**March 15, 2015**				**April 8, 2016**				
Trial #	**BNDVI**	**ENDVI**	**GIPVI**	**GNDVI**	**BNDVI**	**ENDVI**	**GIPVI**	**GNDVI**	**BNDVI**	**ENDVI**	**GIPVI**	**GNDVI**	**Yield**
1	0.98	0.98	0.94	0.94	0.97	0.96	0.92	0.92	0.88	0.85	0.94	0.94	0.48
2	0.94	0.94	0.91	0.91	0.93	0.93	0.88	0.88	0.93	0.9	0.97	0.97	0.78
3	0.92	0.92	0.9	0.9	0.91	0.91	0.86	0.86	0.92	0.9	0.94	0.94	0.66
4	0.93	0.93	0.9	0.9	0.93	0.94	0.82	0.82	0.94	0.9	0.92	0.92	0.84
5	0.92	0.92	0.87	0.87	0.91	0.91	0.84	0.84	0.9	0.91	0.95	0.95	0.46

6	0.85	0.87	0.8	0.8	0.83	0.85	0.78	0.78	0.96	0.91	0.96	0.96	0.87
7	0.89	0.9	0.75	0.75	0.89	0.92	0.67	0.67	0.96	0.95	0.97	0.97	0.37
8	0.91	0.9	0.89	0.89	0.92	0.93	0.85	0.85	0.85	0.84	0.9	0.9	0.73
9	0.95	0.95	0.94	0.94	0.98	0.98	0.91	0.91	0.92	0.93	0.91	0.91	0.86
10	0.95	0.95	0.91	0.91	0.96	0.96	0.88	0.88	0.86	0.85	0.93	0.93	0.5
Mean	0.92	0.93	0.88	0.88	0.92	0.93	0.84	0.84	0.91	0.89	0.94	0.94	0.66
Range	0.85-0.98	0.87-0.98	0.75-0.94	0.75-0.94	0.83-0.98	0.85-0.98	0.67-0.92	0.67-0.92	0.85-0.96	0.84-0.95	0.9-0.97	0.9-0.97	0.37-0.87

FIGURES

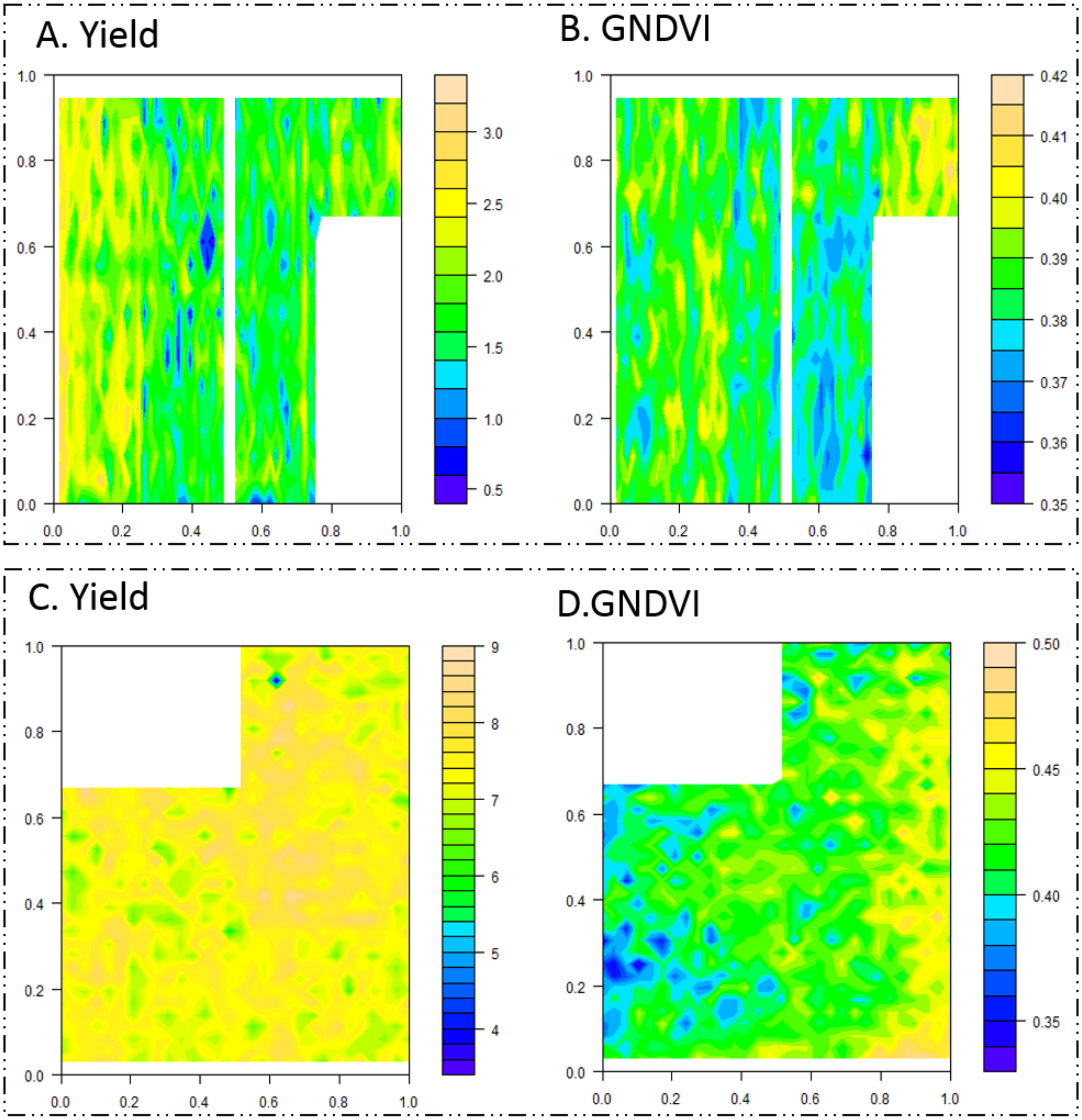

Figure 8 (A) Mapping yield values in drought environment shows the spatial variation across the field. (B) The graph of GNDVI values for drought in march 10, 2016. (C) The yield values in irrigated environment shows patches of spatial variation across the field, although less variation compares to the yield in drought. (D) map of GNDVI values for irrigated in March 10, 2016.

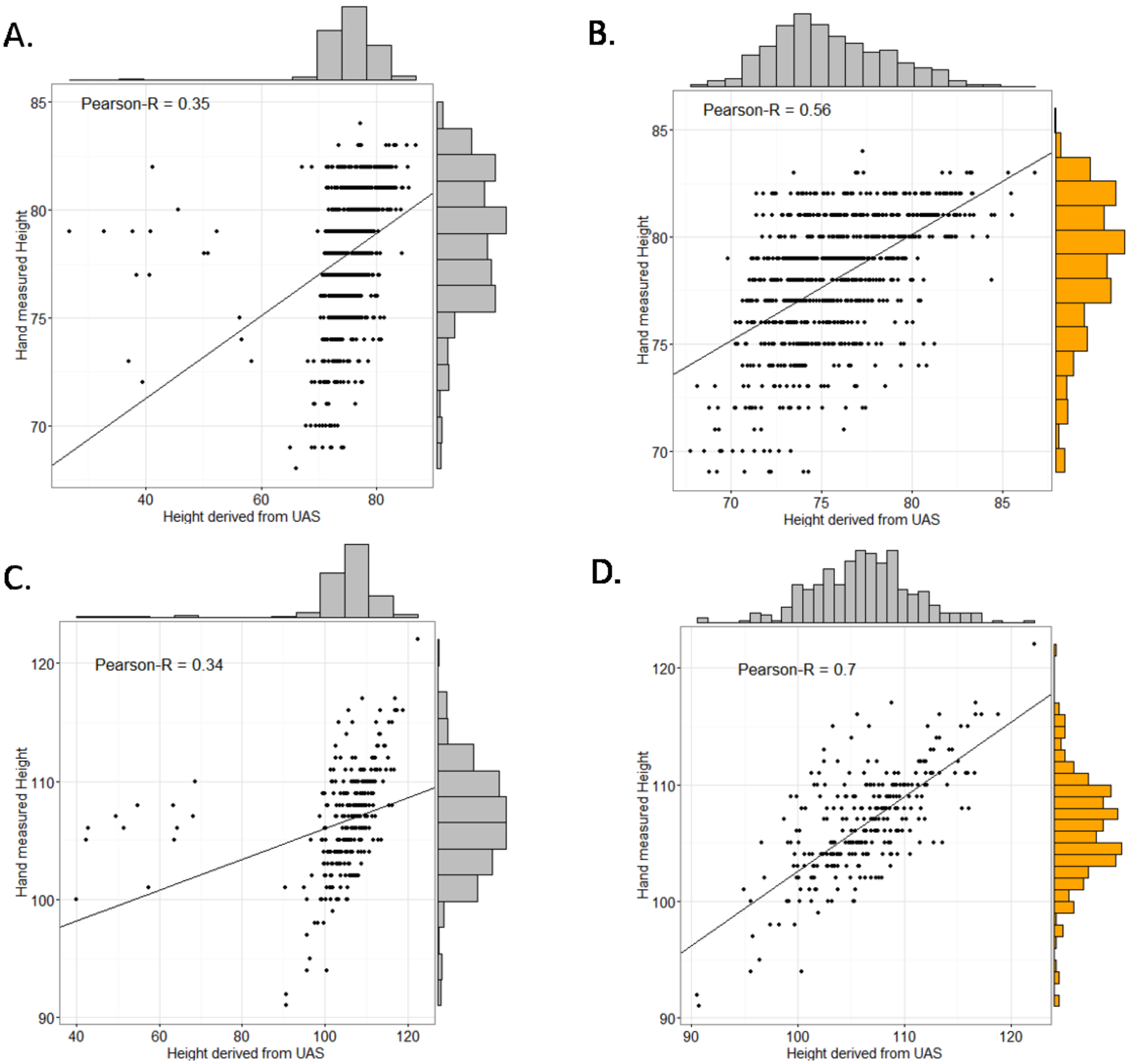

Figure 9 (A) Correlation between 900 manual height data collected from the drought environment, and the 900 height extracted from UAS (r= 0.35). (B) The correlation improves after removing the data points with high standard variations from heights extracted from UAS imagery (r= 0.56). (C) Pairwise correlation between 300 manual height data from the first rep of each trial in irrigated environment, and corresponding height extracted from UAS (r= 0.34). (D) The correlation improves after removing the data points with high standard variations (r= 0.7).

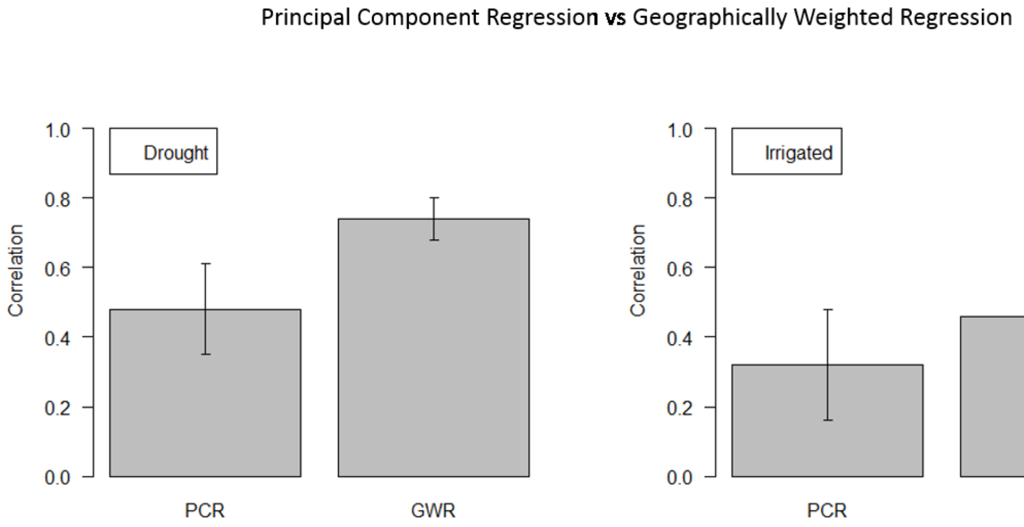

Figure 10 Prediction accuracy between predicted grain yield and observed grain yield for drought and irrigated environment using principal component regression and geographically weighted regression. GWR resulted in higher prediction accuracies compared to principal component regression (r=0.74 for drought environment using GWR versus r=0.48 suing PCR, and for irrigated environment, r=0.46 using GWR approach versus r=0.32 using PCR analysis)

Chapter 4 - Spatial Adjustment of High-Throughput Phenotypic Data Extracted from Unmanned Aerial System (UAS) Imagery of Field Trial in Wheat Breeding Nurseries

Abbreviations:

BNDVI, blue normalized difference vegetation index; DEM, digital elevation model; ENDVI, enhanced normalized difference vegetation index; EYT, elite yield trials; GCP, ground control point; GNDVI, green normalized difference vegetation index; HTP, high-throughput phenotyping; MVNG, moving grid adjustment; NIR, near infrared; UAV unmanned aerial vehicle; UAS, unmanned aerial system; UTM, Universal Transverse Mercator; VI, vegetation index

ABSTARCT

Unmanned aerial systems (UASs) have the potential to provide breeders with phenological data such as plant height and vegetation indices to help with more accurate selections on larger populations. The phenotypes are determined by the genetics of each entry in the nursery, but also influenced by the spatial variation across the field along with the variation of genotypic values. To improve the accuracy of selections, breeder needs to account for non-heritable environmental variation in the form of spatial field effects. There has been extensive investigation into field design and statistical models to account for field effects, however this previous work was generally limited in the overall treatment of the breeding field experiments as geospatial entities. The objective of this study is to evaluate the use of geostatistical spatial analysis for controlling the heterogeneity in yield data as well as high throughput phenotypic data derived from UAS imagery in a large wheat breeding nursery. We analyzed the temporal phenotypic data extracted from UAS imagery for two environments during the growing season and detected the spatially non-random patterns in the data. To correct the trends observed in the field, we modified the R package, mvngGrAd, in a way that the function uses the phenotypic information extracted from geo-referenced aerial imagery in a latitude-longitude grid to obtain an adjusted phenotypic value of the plot in the center of the moving circular window. The adjustment is based on using the mean of all the adjacent plots as a covariate. To find the optimum size of the moving windows, we applied a hotspot analysis of each dataset and used the Z score values as a guide to have different window sizes for different patches of variation in the field. After spatial adjustment, we found an increase in broad-sense heritability for vegetation indices obtained from UAS platforms and grain yield in both environments. The heritability gains were higher for vegetation indices extracted from UAS imagery at multiple time points for

both environments. The analysis implemented in this study enables breeders with collection and post-processing of HTP measurements on larger populations and can provide increased accuracy for selection in plant breeding. Overall the use of UAS imaging to improve selection in plant breeding has great promise when combined with analysis and statistical methods that fully leverage the spatial nature of the breeding trial data.

INTRODUCTION

Field phenotyping of large populations is a constraint that limit our capacity to fully understand quantitative traits, especially those related to biotic and abiotic stress (White et al. 2012). However, recent development in field-based high-throughput phenotyping (HTP) platforms alleviates the phenotyping bottleneck (Crain et al. 2015; Crain et al. 2016; Andrade-Sanchez et al. 2014; Deery et al. 2014) and provides opportunities for breeders to leverage this technology to improve selection accuracy and increase population size in breeding programs.

New advances in remote sensing technology considerably increase demand on high-throughput phenotyping mainly due to their ability to phenotype a significant number of genotypes in breeding nurseries in a very short time compare to manual measuring methods (Fritsche-Neto & Borém 2015). Use of these technologies has led to a boom in precision agriculture, but applying these advances to breeding requires a drastic increase in the accuracy, processing speed and volume of measurements.

One of the emerging technologies in HTP platforms is unmanned aerial vehicles (UAV), which have undergone a remarkable development in recent years (Baluja et al. 2012; Dunford et al. 2009; Chapman et al. 2014; Chao et al. 2010; Gonzalez-Dugo et al. 2013). UAVs use sensor systems and automated computer algorithms to extract phenotypic traits for large genetic mapping populations using non-destructive and non-invasive sampling methods. Like most new technologies in phenotyping platforms, the main focus for UAVs has been on combining robotic vehicles with imaging systems and sensors for automatic data acquisition. And less well-developed are image processing that evaluates the quality and accuracy of the data before handing it to the breeders.

Large breeding nurseries are often affected by spatial variation across the field. These variations are caused by multiple environmental factors that can vary across a field such as soil fertility, soil type, moisture holding capacity, and also many human-made variations such as irrigation system, the direction of cultivation/harvesting, and previous crop cycles (Funda et al. 2007; Bos & Caligari 2008; Sarker & Singh 2015). The spatial variation in the field, and the variations in the quality of growing conditions could favor some plots to be selected as the superior phenotypic value, despite not being superior genotype. These spatial variations, be it randomly or with a trend, need to be taken into account when using phenotypic data and yield values for selection in breeding programs (Bos 2008; Lado et al. 2013).

Data extracted from unmanned aerial systems (UAS) is not an exception, as it also records the characteristics of the plants resulting from the interaction of plant's genotype with its growing condition. Using UASs is aimed at improving and accelerating the selection process. To improve the efficiency of UAS data in breeding programs, we need to make sure that the coefficient of correlation between the derived phenotypic values and the genotypic values are as high as possible, and one way to do so is minimizing the spatial variation in the field data (Bos 2008).

Different strategies exist, including experimental field designs, and post-processing (Quinn & J.Keough 2002; Casler 2013). The three main concepts for the field designs that experimental designs all have in common are replication to calculate and reduce experimental error; control of variation between plots; and randomization, to remove bias from the confounding effects of genotype and environment or treatment effects (Es et al. 2007; Rutherford 2005; Mead 1997).

There are several row and column designs developed to control the spatial variations in the field (Atkinson & Bailey 2001; Quinn & J.Keough 2002; Bos & Caligari 2008; Es et al. 2007; Gilmour et al. 1997; W. L. Leiser et al. 2012), nevertheless due to the presence of spatial variability between plots within a block and also between plants within a plot; these experimental designs remain limited (Katsileros et al. 2015). Although a good choice of experimental design can reduce the effect of spatial heterogeneity, there is a need to address these variations when analyzing the treatments to increase their precision. Correspondingly, model-based approaches for analyzing field trials that focus on the need to control spatial variation have been put forward (Hu & Spilke 2009; Zas 2006; Lado et al. 2013; Katsileros et al. 2015; Bowman 1993; Hartung et al. 2006).

Many studies have shown the ability of geostatistical approaches in removing spatial effects from the raw data. These methods can estimate spatial effects more efficiently and decrease the need for check plots. Considering a good spatial model is selected, this makes a compelling choice over blocking designs for reducing overall plot numbers (Wu et al. 1998; Hartung et al. 2006).

Semivariograms and kriging, as a geostatistic approach have been evaluated for the effect of modeling the spatial variation (Zas 2006; Hartung et al. 2006). Kriging is based on the regionalized variable theory that assumes the spatial variation in the phenomenon is statistically homogeneous throughout the field (for example, the same pattern of variation can be observed at all locations on the field). This hypothesis of spatial homogeneity is fundamental to the regionalized variable theory (McBratney et al. 1981; OLIVER & WEBSTER 1990). This characteristic of the Kriging method makes it unsuitable for fields with multiple treatments that are expectable to have different patterns of variations.

Another method is nearest neighbor method proposed by Papadakis (1937). This is an analysis of covariance to reduce the effects of spatial heterogeneity in yield values (J.S 1937). When spatial heterogeneity is present, near neighbors are more similar than far neighbors, i.e., data are autocorrelated (Zas 2006). Other modifications have been applied to the Papadakis method such as the moving average method based on the use of the arithmetic mean for the two neighbors' plots (Townley-Smith & Hurd 1973).

Linear regression models with moving means as covariate is another option to account for spatial correlations. The adjustment using this method is made by calculating the mean of all the entries included and using it as a covariate (Lado et al. 2013; Katsileros et al. 2015; Townley-Smith & Hurd 1973; Bos 2008; Kempton & Gleeson 1997; Cullis et al. 1998). Although this method is common in unreplicated plant breeding field trials, it has been reported for analysis of replicated trials as adjustment can improve the spatial error in the data, and in some cases is superior to methods based on row and columns analysis or blocking analysis based on the experimental design alone (Lado et al. 2013; Bos 2008; Mitchell et al. 1982; Cullis et al. 1998; Gilmour et al. 1997; W L Leiser et al. 2012; Townley-Smith & Hurd 1973).

The goal of this study is to integrate geospatial techniques with moving grid method to adjust for environmental variations in spatio-temporal high throughput phenotypic data extracted from UAS imagery and yield data of a large wheat breeding nursery.

MATERIALS and METHODS

Study Area

The study was conducted at Norman E Borlaug Experiment Station at Ciudad Obregon, Sonora, Mexico, during the wheat growing season in 2016. The experiment composed of 300 advanced wheat lines distributed in 10 trials, each trial consisting of 30 entries. The trials were grown in each of the following environments: drought and optimally irrigated environment. The drought experiment was sown at the optimum planting date with minimal irrigation throughout the season. The irrigated environment was sown at optimal planting date (mid-November). Full irrigation was maintained throughout the irrigated trial. Irrigated, and drought trials were sown in mid-November. During the growing season, the irrigated environments received 500mm of water, and drought received 180mm of irrigation. Nutrient levels were maintained at optimum levels, and pesticides were applied as needed. Grain yield was measured by harvesting with a small plot combine.

Field Data: Design and Collection

High-throughput phenotypic data was collected with a consumer grade Canon S100 camera modified to Blue-Green-NIR (400-760nm) by MaxMax (LDP LLC, Carlstadt, NJ 07072, USA, www.maxmax.com) The S100 was held by a custom gimble mounted on a small UAV, (IRIS+, 3D Robotics, Inc, Berkeley, CA 94710, USA).

For each environment, aerial imagery was taken three times from heading through senescence using this low-cost UAV platform (IRIS+ and a modified Canon S100 camera) with observation days spaced at approximately seven to ten-day intervals, depending on the weather condition. All images were taken in RAW format (.CR2) to avoid loss of image information. An overview of each day of UAS observation is summarized in Table 11.

A total of 13 ground control points (GCPs), per field, were distributed on 25 cm x 25 cm square white metal sheets and mounted on a 50 cm post. These targets were designed as circles with black and white segments on them to provide easy identification of the GCPs. Coordinates of these coded targets were measured with a Trimble R4 RTK GPS, with a horizontal accuracy of 0.025 m and a vertical accuracy of 0.035 m. These GCPs were maintained throughout the crop season to enable georeferncing of UAS imagery from multiple dates.

The number of GCPs depends on the amount of distortion in the imagery and the desired level of accuracy. The aerial imagery obtained from UASs deliver inaccurate location information. By georeferencing the data using GCPs, we can align the features in the aerial imagery with spatially referenced data on the ground(GCPs) (Toyama et al. 2003). Some examples of reference systems are Latitude and Longitude, Universal Transverse Mercator (UTM), and State Plane Coordinate System. These GCPs were used to build a polynomial transformation based on a least-squares fitting algorithm, that shifts each of the orthomosaics generated from UAS imagery from its existing location to the spatially correct location (Brovelli & Minghini 2012; Sheta et al. 2012). A linear transformation equation requires a minimum of 3 GCPs, a second-order equation needs 6 points, and a third-order equation: a minimum of 10 points. As in this study, it is suggested to have more than the minimum numbers to lower the errors in fitting the equation (Hamza 2009).

An in-house made calibration panel was set on the field before each flight. This foldable panel consisted of six individual 7 mm thick lightweight plywood panels with levels of gray from 0% being white and 100% being black and were attached using metal hinges. This panel was used as a white balance correction and reflectance adjustment of the temporal imagery as described in Haghighattalab et al. (Haghighattalab, González Pérez, et al. 2016).

High Throughput Phenotyping Analysis

We used a semi-automated data analysis pipeline presented in Haghighattalab et al. (Haghighattalab, González Pérez, et al. 2016) to analyze each dataset and extracted plot level phenotypic values for different vegetation indices (VIs) including green NDVI, blue NDVI, and enhanced NDVI (GNDVI, BNDVI, and ENDVI). HTP data processing, for each time point of data collection, and for each environment after pre-processing the raw imagery of Canon S100 in DPP software (http://www.canon.co.uk/support/camera_software/) are as follows:

Semi-automatically analyzing the images in Agisoft software: 1) Alignment of photos and building sparse point clouds, 2) importing GCPs and geo-referencing the images, 3) dense point cloud construction, 4) manually classifying points into plants, and ground, 5) creating digital elevation model(DEM) based on classified point clouds, 6) orthomosaic generation using DEM, 7) calculation of various VIs, and 8) extraction of plot level data from VIs' map.

Image processing was primarily conducted using Python and R scripts, open source software QGIS (http://qgis.osgeo.org) and Agisoft PhotoScan package (Agisoft LLC, St. Petersburg, Russia, 191144) (Haghighattalab 2015; Haghighattalab & Agisoft LLC 2014; Haghighattalab, González Pérez, et al. 2016).

Moving Average Window Spatial Adjustment

We applied a linear regression model with moving means as a covariate to correct for spatial variation in the field. The basic idea of moving average window adjustment is that the phenotypic value expected for plot i is correlated to some degree with its neighboring (Bos 2008). The adjustment is done by calculating the mean of all the neighboring plots and using it as a covariate for the plot in the center of the search window (Lado et al. 2013; Bos 2008).

Since we georeferenced the UAS imagery and can extract Latitude and Longitude coordinate for each pixel in the images, and correspondingly the center for each plot, we can locate the neighbor plots based on the coordinates of each plot extracted from UAS imagery and not based on the row and column information (Traditional method of moving grid) (Figure 11). We also can develop the search window not based on the number of neighbors, but based on the distance between each plot and its neighboring plots using a user defined radius. This makes a "circular" moving window search available for the user. These modifications enable us to evaluate the benefits of a less restrictive experimental design in comparison with the traditional row-column designs in breeding programs.

Hot-spot Analysis to Choose the Optimum Window Size

The circular moving window around a given plot is expected to capture a number of plots subjected to growing conditions most similar to that plot (Bos 2008). Moreover, the spatial heterogeneity in the field does not follow the same pattern all over the field. Therefore, there is a need to find the optimum window size for moving grid and customize the adjustment based on the location of the variation.

The optimum value for window size, say: ws_{opt}, depends on the nature of the variation, it could change from trial to trial, and from corner to corner. A high value for *ws* may cause bias estimation of the quality of the growing conditions, and a small value suggests a higher mean squared error of the mean phenotypic values of plot i neighboring. There are not any guidelines to choose the ws_{opt}, and $ws \approx 8$ is often suggested as a reasonable choice for the window size (Bos & Caligari 2008).

After extracting phenotypic values from the UAS imagery, we explored each feature within the context of neighboring features and performed a hotspot analysis. Hotspot analysis is a local statistics tool that calculates Getis-Ord Gi* statistic for each data available for a plot in the field (Equations 1,2,3) (Getis & Ord 1992; Mitchell 2005). Gi* identifies if local pattern is different to what is observed across the field. The Gi* statistic returned for each plot in the dataset is a Z score and p-value, by calculating the local sum for a wheat plot and its neighbor compared proportionally to the sum of all plots. When the local sum is very different from the expected local sum, and once that difference is too large to be due to random chance, a statistically significant Z score outcomes (Chester 1987; Goodchild 1986; Getis & Ord 1992; Ord & Getis 1995; Mitchell 2005).

The Z score is based on the Randomization Null Hypothesis computation, which is complete spatial randomness. Z score indicates whether the observed spatial clustering of high or low values is more distinct than a random distribution of those same values which could help with detecting spatial variation in the field trials (Figure 12) (ERSI 2016; Mitchell 2005). Although hotspot analysis can be applied to skewed data because it is "asymptotically normal".

For statistically significant positive Z score values, the larger the Z score is, the more intense the clustering of high values (hot spot). And correspondingly for statistically significant negative values of Z scores, the smaller the Z score is, the more intense the clustering of low values (cold spot) (Mitchell 2005; ERSI 2016; Chester 1987). A Z score near zero indicates no apparent concentration (neighbors have a range of values). To determine if the Z score is statistically significant, it needs to be compared to the range of values for a particular confidence level. For example, at a significance level of 0.05, a Z score would have to be less than –1.96 or greater than 1.96 to be statistically significant.

$$G_i^* = \frac{\sum_{j=1}^{n} w_{i,j} x_j - \bar{X} \sum_{j=1}^{n} w_{i,j}}{S \sqrt{\frac{\left[n \sum_{j=1}^{n} w_{i,j}^2 - \left(\sum_{j=1}^{n} w_{i,j}\right)^2\right]}{n-1}}} \qquad \text{(Equation 1)}$$

G_i^* is the Z score for plot i, where x_j is the phenotypic value for plot j, $w_{i,j}$ is the spatial weight between plot i and j, n is equal to the total number of features and S is given below in Equation 3:

$$\overline{X} = \frac{\sum_{j=1}^{n} x_j}{n} \qquad \text{(Equation 2)}$$

$$S = \sqrt{\frac{\sum_{j=1}^{n} x_j^2}{n} - (\overline{X})^2} \qquad \text{(Equation 3)}$$

Gi* results are Z scores – Z scores indicate the place of a particular value in a dataset relative to the mean, standardized with respect to the standard deviation.

The conceptualization of Spatial Relationships parameter should reflect inherent relationships among the wheat plot HTP values that we are analyzing.

The conceptualization of spatial relationships or the distance band value need to ensure every wheat plot (every feature in the analysis) has at least one neighbor, spatially when the data does not follow a normal distribution and is skewed. The number of neighbors needs to be neither too small nor too small; Z scores are reliable, even with skewed data as long as each feature is associated with several neighbors, as a rule of thumb, 8 neighbors (Mitchell 2005).

There are several strategies such as inverse distance, k-nearest distance or fixed distance that one can choose based on the impact of neighboring plots on one another (Mitchell 2005; ERSI 2016). We used inverse distance weight strategy and specified a cutoff distance (using the Euclidean distance between the centroids of plots) to include 8 neighbors for each plot.

Broad-sense Heritability

Improving phenotypic values through identification and selection the superior genotypes is the ultimate goal of plant breeders. Due to the environmental effects on phenotypic values, there is not a perfect correspondence between phenotypic and genotypic values. Heritability is an index that expresses the degree of correspondence between phenotypic and genotypic values (Holland et al. 2003).

The phenotypic variation (V_P) of an individual is the combined result of its genotype variation (V_G) and the effects of the environment (V_e):

$$V_P = V_G + V_e \qquad \text{(Equation 4)}$$

Heritability estimates the proportion of variance of a phenotype that is due to genetic variation (Holland et al. 2003). A successful adjustment increases the heritability by reducing in the environmental variance.

To estimate heritability, we calculated the plot-level value for HTP measurements and fit mixed model for replication, block, and genotype as random effects (equation 5).

$$H^2 = \frac{\sigma^2_{\text{genotypic}}}{\sigma^2_{\text{genotypic}} + \frac{\sigma^2_{\text{error}}}{\text{nrep}}} \qquad \text{(Equation 5)}$$

Where $\sigma^2_{\text{genotypic}}$is genotypic variance, σ^2_{error} is error variance*, nrep* is the number of replicates in the trial (*nrep*=3). The *lme4* R package was used for all mixed model analysis (Bates et al. 2014).

RESULTS and DISCUSSION

Image Processing for HTP Data

We deployed a low-cost UAS and consumer-grade imaging system at multiple times throughout the growing season for two different growing environments (Table 11). We analyzed all the imagery with minimum user support using our custom pipeline (Haghighattalab, González Pérez, et al. 2016). Image processing included converting raw images to TIFF format, georeferencing the imagery using GCPs, point cloud generation, digital elevation model (DEM) and orthomosaic generation using DEM, VI map generation, and plot level data extraction. A 16 bit orthomosaic TIFF image was generated with the semi-automated pipeline developed in Haghighattatlab et al (Haghighattalab & Agisoft LLC 2014; Haghighattalab, Perez, et al. 2016).

Hot Spot Analysis

We used the hotspot analysis function in ArcGIS® software by Esri to get the Z score values for each plot in the field (Figure 13). We used inverse distance weight strategy and included at least four neighbors for each feature. Z score values represent the statistical significance of the spatial clustering of yield values in both environments, with inverse distance conceptualization of spatial relationships and accounting for 8 neighbors for each plot. The resultant Z score values help us to understand the possibility and the location of spatial variation in the field (Mitchell 2005). Using the Z score we customized the size of the moving average window in the modified mvngGrAd package for each hot spot/cold spot area in the field, accounting a minimum 6 neighbors. Yield values shows variation in the field spatially, for example in drought environment, hotspots can be observed in patches on the left side of the field as well as on some other areas in small patches (Figure 14). For irrigated growing environment it can be found that coldspots of yield are clustered mostly on the left side of the field, and hotspots on the right side.

Using the spatial pattern analysis, we can detect the probability of non-random clustering in the phenotypic data. This enables us to compare patterns of different distributions or different time periods. With the temporal data set in hand, we can also determine whether the clustering becomes more or less extreme over time (Figure 15).

Moving Mean Adjustment

The R package mvngGrAd [46], uses a moving grid adjustment method to adjust for environmental variation in field trials. In this package, the trials are arranged as a matrix of row-column design. Each entry in this matrix is associated with a cell, respectively with a row and column number. A grid is then created around each cell and the mean of the cells included in the grid is calculated [46]. We modified this package to incorporate geospatial data derived from aerial imagery into moving grid adjustment analysis.

High throughput phenotypic data for VIs and yield data for both environments were analyzed using the mvngGrAd package (Technow 2012) in R. The analysis was performed individually for each growing environment and each date. A linear regression model with moving means as covariate (MVNG), was considered to account for spatial correlations.

The number of neighbors for each window was different, and it was based on the number of plots that fall into a circle with a radius of “r” defined based on the Z score values (Figure 11).

The traits under study (GNDVI, ENDVI, BNDVI, and grain yield) were analyzed adjusting for spatial variation using a linear mixed model, with moth standard moving grid approach, and modified adjustment using spatial data extracted from the imagery. The modified moving grid adjustment presented more homogeneous residuals along the field compare to the standard moving grid without using spatial data (Figure 15 and 16). We observed the same result for ENDVI and BNDVI for both environments as GNDVI. The irrigated field showed minimal spatial variation and after spatial adjustment for the yield data, we observed homogeneous residuals throughout the field (Figure 16). Both spatial adjustment approach showed same results for irrigated field.

On the other hand, drought environment presented a more pronounced field variation (Figure 15). And the adjustment using the modified moving grid for drought environment showed more uniform distribution of errors in the field, for both yield and the VIs.

Assessment of Spatial Adjustment using Broad-sense Heritability

Within environment and trial, we calculated broad-sense heritability, commonly known as repeatability (Holland et al. 2003), for extracted VIs and grain yield, before and after moving grid adjustment.

Figure 17, and 18 shows the average heritability across all ten trials, before and after moving grid adjustment. The heritability estimates were generally lower for grain yield and also VI values under irrigated growing conditions compare to drought. H2 for grain yield increased for all trials within drought environment, and for all trials in the irrigated environment with the exception of one trial.

Broad-sense heritability estimates for VIs within individual environments, were increased by using moving grid adjustment, thus make selection more efficient.

CONCLUSION

The challenge in wheat breeding remains in accelerating the selection of high-yielding and well adapted of genotypes. Newly developed technologies in high-throughput phenotyping allow taking up this challenge and provide breeders with tools to rapidly measure physiological and agronomic traits in-season. By integrating genetic information with high-throughput phenotypic data, breeders will be able to better connect genotype to phenotype while more quickly and efficiently identifying and selecting superior higher yielding crop varieties from a larger population.

To improve the accuracy of selections, the breeder needs to address the phenotypic variations caused by growing conditions. Geostatistical approaches with moving grid adjustment were examined in two environments contrasting for the accuracy gains as indicated by heritability increases. The high throughput phenotypic data and grain yield for each environment were adjusted individually and showed a strong spatial effect through the field for both drought and irrigated growing condition. The implementation of a moving mean spatial correction model enabled a better adjustment in measurements, showing an increment in the heritability of measurements. Spatial adjustment in the drought environment had a strong impact on heritability for both yield values and VIs while the irrigated trials displayed an increase in heritability with spatial adjustment for all the VIs, and for yield in nine trials out of ten. We demonstrate that the implementation of geospatial correct for field effects in the area of field-based high throughput phenotyping can be a powerful approach to increase the heritability of traits for selection by better accounting for variable field effects.

Acknowledgements

This work was done through the International Maize and Wheat Improvement Center (CIMMYT), Mexico and supported through the National Science Foundation - Plant Genome Research Program (IOS-1238187) and the US Agency for International Development Feed the Future Innovation Lab for Applied Wheat Genomics (Cooperative Agreement No. AID-OAA-A-13-00051).

Competing Interests

The authors declare no competing interests.

REFERENCES

Andrade-Sanchez, P. et al., 2014. Development and evaluation of a field-based high-throughput phenotyping platform. Funct Plant Biol, 41. Available at: http://dx.doi.org/10.1071/FP13126.

Atkinson, A.C. & Bailey, R.A., 2001. One hundred years of the design of experiments on and off the pages of Biometrika. Biometrical, 88 (1), pp.53–97. Available at: http://biomet.oxfordjournals.org/content/88/1/53.abstract.

Baluja, J. et al., 2012. Assessment of vineyard water status variability by thermal and multispectral imagery using an unmanned aerial vehicle (UAV). Irrigation Science, 30(6), pp.511–522. Available at: http://link.springer.com/10.1007/s00271-012-0382-9 [Accessed August 15, 2014].

Bates, D. et al., 2014. lme4: Linear mixed-effects models using Eigen and S4.

Bos, I., 2008. Selection methods in plant breeding, chapter 14 2nd editio. P. D. S. (Peter D. S. . Caligari, ed., Dordrecht: Dordrecht : Springer.

Bos, I. & Caligari, P., 2008. Selection Methods in Plant Breeding 2nd editio., Dordrecht : Springer.

Bowman, D.T., 1993. Estimating Spatial Variation in Analysis of Data from Yield Trials : A Comparison of Methods. Agronomy Journal, 85(6), pp.1244–1253.

Brovelli, M.A. & Minghini, M., 2012. Georeferencing old maps : a polynomial-based approach for Como historical cadastres. e-Perimetron, 7(3), pp.97–110.

Casler, M.D., 2013. Finding Hidden Treasure : A 28-Year Case Study for Optimizing Experimental Designs.

Chao, H., Cao, Y. & Chen, Y., 2010. Autopilots for small unmanned aerial vehicles: a survey. Int J Control Autom Syst, 8. Available at: http://dx.doi.org/10.1007/s12555-010-0105-z.

Chapman, S. et al., 2014. Pheno-Copter: A Low-Altitude, Autonomous Remote-Sensing Robotic Helicopter for High-Throughput Field-Based Phenotyping. Agronomy, 4(2), pp.279–301. Available at: http://www.mdpi.com/2073-4395/4/2/279/ [Accessed September 14, 2016].

Chester, D.K., 1987. Statistics in geography by David Ebdon, Basil Blackwell, 1985. No. of pages: 232. Price: £8.50 (soft covers). Geological Journal, 22(1), pp.61–62. Available at: http://dx.doi.org/10.1002/gj.3350220108.

Crain, J. et al., 2015. Development and deployment of a portable field phenotyping platform. Crop Sci., 56. Available at: http://dx.doi.org/10.2135/cropsci2015.05.0290.

Crain, J.L., Reynolds, M.P. & Poland, J.A., 2016. Utilizing high-throughput phenotypic data for improved phenotypic selection of stress adaptive traits in wheat. Crop Science.

Cullis, B. et al., 1998. Spatial Analysis of Multi-Environment Early Generation Variety Trials. International Biometric Society, 54(1), pp.1–18.

Deery, D. et al., 2014. Proximal Remote Sensing Buggies and Potential Applications for Field-Based Phenotyping, Available at: http://www.mdpi.com/2073-4395/4/3/349/ [Accessed September 14, 2016].

Dunford, R. et al., 2009. Potential and constraints of unmanned aerial vehicle technology for the characterization of Mediterranean riparian forest. Int J Remote Sens, 30. Available at: http://dx.doi.org/10.1080/01431160903023025.

ERSI, 2016. How Hot Spot Analysis (Getis-Ord Gi) works—ArcGIS Pro _ ArcGIS for Desktop. Redlands, CA: Environmental Systems Research Institute.

Es, H.M. Van et al., 2007. Spatially-Balanced Complete Block designs for field experiments. Geoderma, 140, pp.346–352.

Fritsche-Neto, R. & Borém, A., 2015. Phenomics,

Funda, T. et al., 2007. Addressing spatial variability in provenance experiments exemplified in two trials with black spruce. Journal of Forest Science, 53(2), pp.47–56. Available at: http://agriculturejournals.cz/publicFiles/00038.pdf.

Getis, A. & Ord, J.K., 1992. The Analysis of Spatial Association by Use of Distance Statistics. Geographical Analysis, 24(3), pp.189–206. Available at: http://dx.doi.org/10.1111/j.1538-4632.1992.tb00261.x.

Gilmour, A.R., Cullis, B.R. & Verbyla, A., 1997. Accounting for natural and extraneous variation in the analysis of eld experiments 1 Introduction. Journal of Agricultural, Biological, and Environmental Statistics, 2, pp.269–293.

Gonzalez-Dugo, V. et al., 2013. Using high resolution UAV thermal imagery to assess the variability in the water status of five fruit tree species within a commercial orchard. Precision Agriculture, 14(6), pp.660–678. Available at: http://link.springer.com/10.1007/s11119-013-9322-9 [Accessed September 3, 2016].

Goodchild, M.F., 1986. Spatial autocorrelation, Geo Books. Available at: https://books.google.com/books?id=2BYnAQAAIAAJ.

Haghighattalab, A., González Pérez, L., et al., 2016. Application of unmanned aerial systems for high throughput phenotyping of large wheat breeding nurseries. Plant Methods, 12(1), pp.1–15. Available at: http://dx.doi.org/10.1186/s13007-016-0134-6.

Haghighattalab, A., Perez, Lorena Gonzalez, et al., 2016. Application of unmanned aerial systems for high throughput phenotyping of large wheat breeding nurseries Application of unmanned aerial systems for high throughput phenotyping of large wheat breeding nurseries. Plant Methods, (August). Available at: "http://dx.doi.org/10.1186/s13007-016-0134-6.

Haghighattalab, A., 2015. Plot Boundary Extraction. http://dx.doi.org/10.5281/zenodo.46732. Available at: http://dx.doi.org/10.5281/zenodo.46732.

Haghighattalab, A. & Agisoft LLC, 2014. Orthomosaic generation. http://dx.doi.org/10.5281/zenodo.46734. Available at: http://dx.doi.org/10.5281/zenodo.46734.

Hamza, E.H., 2009. Effect of Ground Control points Location and Distribution on Geometric Correction Accuracy of Remote Sensing Satellite Images. In 13th International Conference on Aerospace Sciences & Aviation Technology. pp. 1–14.

Hartung, K., Piepho, H. & Knu, H., 2006. Analysis of genebank evaluation data by using geostatistical methods. Genetic Resources and Crop Evolution, 53, pp.737–751.

Holland, J., Nyquist, W. & Cervantes-Martinez, C., 2003. Estimating and interpreting heritability for plant breeding: An update. Plant Breeding Review, 22, pp.9–112.

Hu, X. & Spilke, J., 2009. Comparison of various spatial models for the analysis of cultivar trials. New Zealand Journal of Agricultural Research, 52(3), pp.277–287. Available at: http://www.tandfonline.com/doi/abs/10.1080/00288230909510512 [Accessed September 14, 2016].

J.S, P., 1937. Methode statistique pour des experiences sur champ. Bulletin Institut d'Amelioration des Plantes a Salonique, 23, pp.1–30.

Katsileros, A., Drosou, K. & Koukouvinos, C., 2015. Evaluation of nearest neighbor methods in wheat genotype experiments. pp.115–123.

Kempton, R.A. & Gleeson, A.C., 1997. Unreplicated trials. In R. A. Kempton, P. N. Fox, & M. Cerezo, eds. Statistical Methods for Plant Variety Evaluation. Dordrecht: Springer Netherlands, pp. 86–100. Available at: http://dx.doi.org/10.1007/978-94-009-1503-9_6.

Lado, B. et al., 2013. Increased genomic prediction accuracy in wheat breeding through spatial adjustment of field trial data. G3 (Bethesda, Md.), 3(12), pp.2105–14. Available at: http://www.pubmedcentral.nih.gov/articlerender.fcgi?artid=3852373&tool=pmcentrez&rendertype=abstract [Accessed September 7, 2016].

Leiser, W.L. et al., 2012. Getting the Most Out of Sorghum Low-Input Field Trials in West Africa Using Spatial Adjustment. Journal of Agronomy and Crop Science, 198(5), pp.349–359. Available at: http://doi.wiley.com/10.1111/j.1439-037X.2012.00529.x [Accessed September 14, 2016].

Leiser, W.L. et al., 2012. Getting the Most Out of Sorghum Low-Input Field Trials in West Africa Using Spatial Adjustment. Journal of Agronomy and Crop Science, 198, pp.349–359.

McBratney, A.B., Webster, R. & Burgess, T.M., 1981. The design of optimal sampling schemes for local estimation and mapping of of regionalized variables—I. Computers & Geosciences, 7(4), pp.331–334. Available at: http://www.sciencedirect.com/science/article/pii/0098300481900777.

Mead, R., 1997. Design of plant breeding trials. In R. A. Kempton, P. N. Fox, & M. Cerezo, eds. Statistical Methods for Plant Variety Evaluation. Dordrecht: Springer Netherlands, pp. 40–67. Available at: http://dx.doi.org/10.1007/978-94-009-1503-9_4.

Mitchell, A., 2005. The ESRI Guide to GIS Analysis. ESRI Press, 2.

Mitchell, J.W., Baker, R.J. & Knott, D.R., 1982. Evaluation of Honeycomb Selection for Single Plant Yield in Durum Wheat1. Crop Science, 22, pp.840–843. Available at: http://dx.doi.org/10.2135/cropsci1982.0011183X002200040033x.

OLIVER, M.A. & WEBSTER, R., 1990. Kriging: a method of interpolation for geographical information systems. International Journal of Geographical Information Systems, 4(3), pp.313–332. Available at: http://dx.doi.org/10.1080/02693799008941549.

Ord, J.K. & Getis, A., 1995. Local Spatial Autocorrelation Statistics: Distributional Issues and an Application. Geographical Analysis, 27(4), pp.286–306. Available at: http://dx.doi.org/10.1111/j.1538-4632.1995.tb00912.x.

Quinn, G.P. & J.Keough, M., 2002. Experimental Design and Data Analysis for Biologists Anessential,

Rutherford, J., 2005. Planning, Construction, and Statistical Analysis of Comparative Experiments. Technometrics, 47(1), pp.92–93. Available at: http://dx.doi.org/10.1198/004017004000000680.

Sarker, A. & Singh, M., 2015. Improving breeding efficiency through application of appropriate experimental designs and analysis models : A case of lentil (Lens culinaris Medikus subsp . culinaris) yield trials. Field Crops Research, 179, pp.26–34. Available at: http://dx.doi.org/10.1016/j.fcr.2015.04.007.

Sheta, B. et al., 2012. Comparison and Analysis of Nonlinear Least Square Methods for navigation (VBN) Algorithms. In International Archives of the Photogrammetry, Remote Sensing and Spatial Information Sciences. pp. 453–456.

Technow, F., 2012. R Package mvngGrAd : Moving Grid Adjustment In Plant Breeding Field Trials. Available at: http://artax.karlin.mff.cuni.cz/r-help/ library/mvngGrAd/html/00Index.html.Accessed October 2, 2016. CRAN, pp.1–12.

Townley-Smith, T.. & Hurd, E.A., 1973. Use of Moving Means in Wheat Yield Trials. Journal of Plant Science, 53, pp.447–450.

Toyama, K., Logan, R. & Roseway, A., 2003. Geographic Location Tags on Digital Images. In Proceedings of the Eleventh ACM International Conference on Multimedia. MULTIMEDIA ’03. New York, NY, USA: ACM, pp. 156–166. Available at: http://doi.acm.org/10.1145/957013.957046.

White, J.W. et al., 2012. Field-based phenomics for plant genetics research. Field Crop Res, 133. Available at: http://dx.doi.org/10.1016/j.fcr.2012.04.003.

Wu, T., Mather, D.E. & Dutilleul, P., 1998. Application of Geostatistical and Neighbor Analyses to Data from Plant Breeding Trials. Crop Science, 38, pp.1545–1553. Available at: http://dx.doi.org/10.2135/cropsci1998.0011183X003800060023x.

Zas, R., 2006. Iterative kriging for removing spatial autocorrelation in analysis of forest genetic trials. Tree Genetics & Genomes, 2(4), pp.177–185.

TABLES

Table 11 Flight information using unmanned aerial vehicle high-throughput phenotyping platform (IRIS+ and modified Canon S100), at CIMMYT, Ciudad Obregon, Mexico, 2016.

Drought Environment						
Dates (2016)	**Flight speed (m/s)**	**Attitude (m)**	**Percent overlap**		**No. of Images**	**Spatial Resolution (cm)**
			Side	**Forward**		
March 2	2	30	70%	80%	98	~0.9
March 10	2	30	70%	80%	100	~0.9
March 14	2	30	70%	80%	99	~0.9
Irrigated Environment						
March 10	2	25	70%	80%	93	~0.9
March 15	2	25	70%	80%	93	~0.9
April 8	2	25	70%	80%	96	~0.9

FIGURES

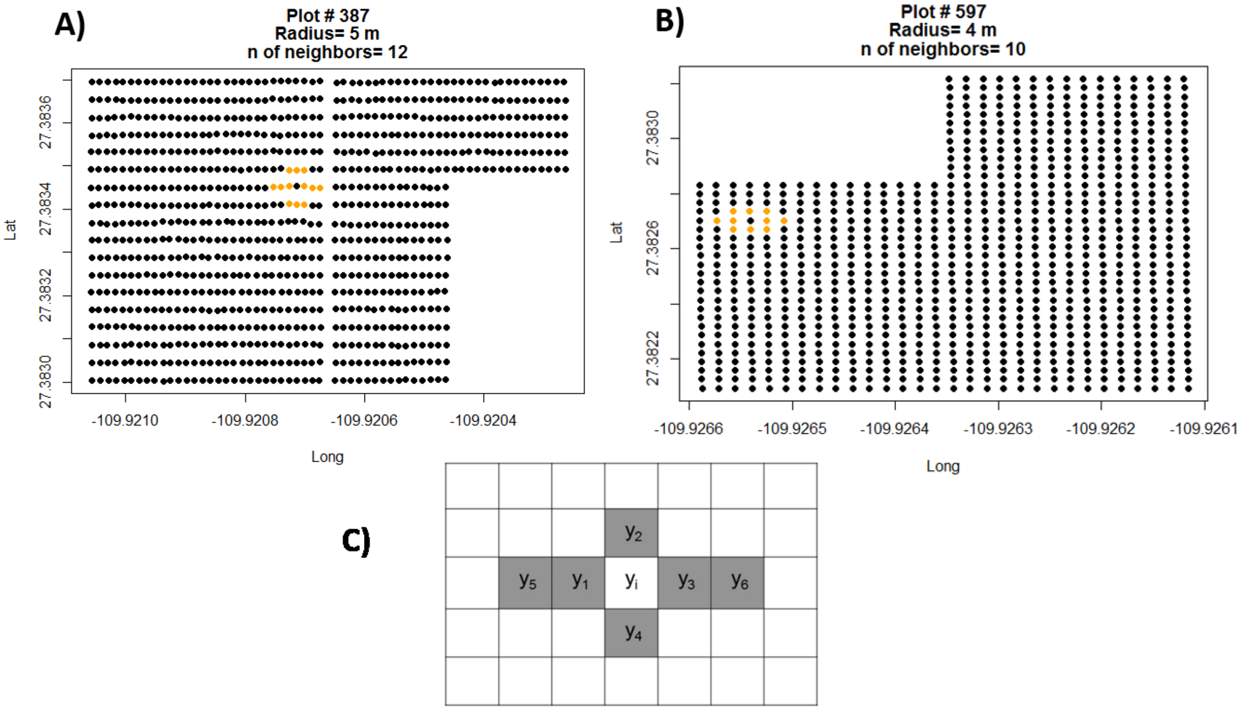

Figure 11 Modified moving window search for A) Drought and B) Irrigated environment. The plots are arranged based on their location on the ground using their Latitude-Longitude coordinates. The search window is a circular window with a defined radius based on the distance of the neighboring plots from each other. C) the search window of moving grid package before adjustment, number of neighboring plots can be defined on each row and column. The circles in the field represent the true centroid of each wheat plots extracted from aerial imagery. The distance between center of wheat plots in irrigated trials is approximately 1.6 m horizontally, and 3.5 m vertically. This distance for drought environment is 1.3 m and 4.6 m. These distances vary throughout the field due to the presence of possible mistakes in planting.

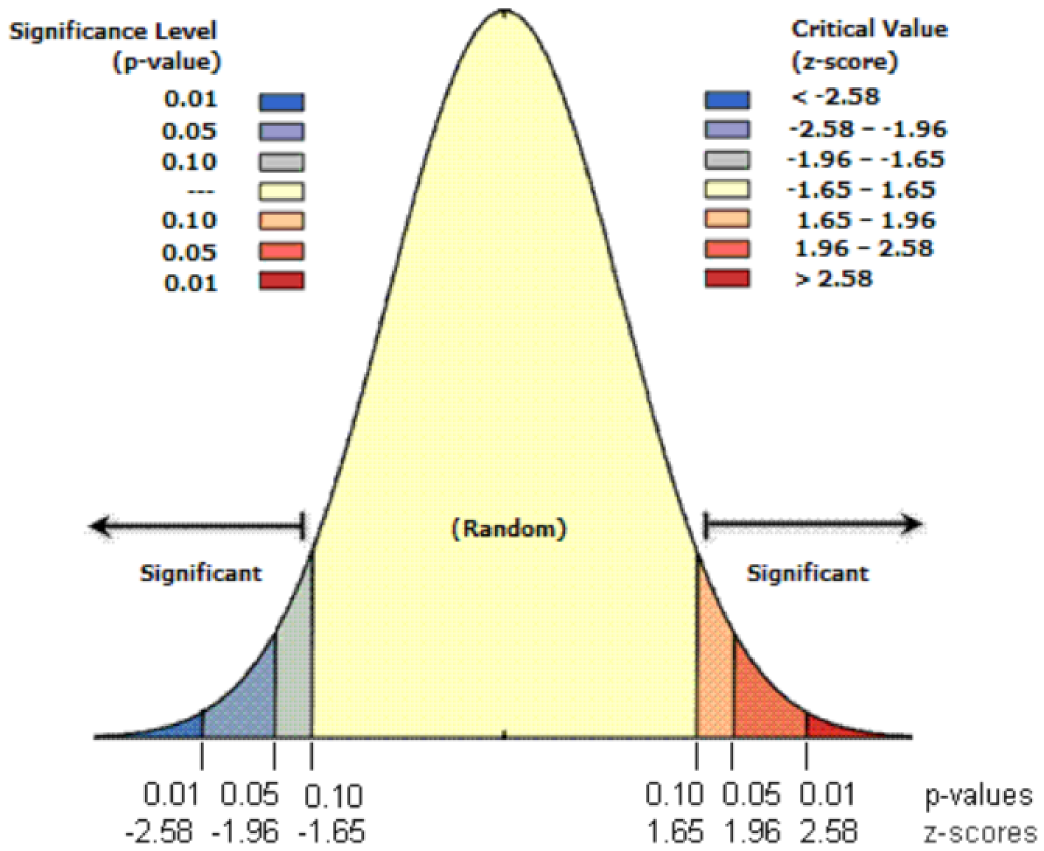

Figure 12 Z scores are standard deviations. For example, a Z score of +2.5, means that the result is 2.5 standard deviations. Both Z scores and p-values are associated with the standard normal distribution.

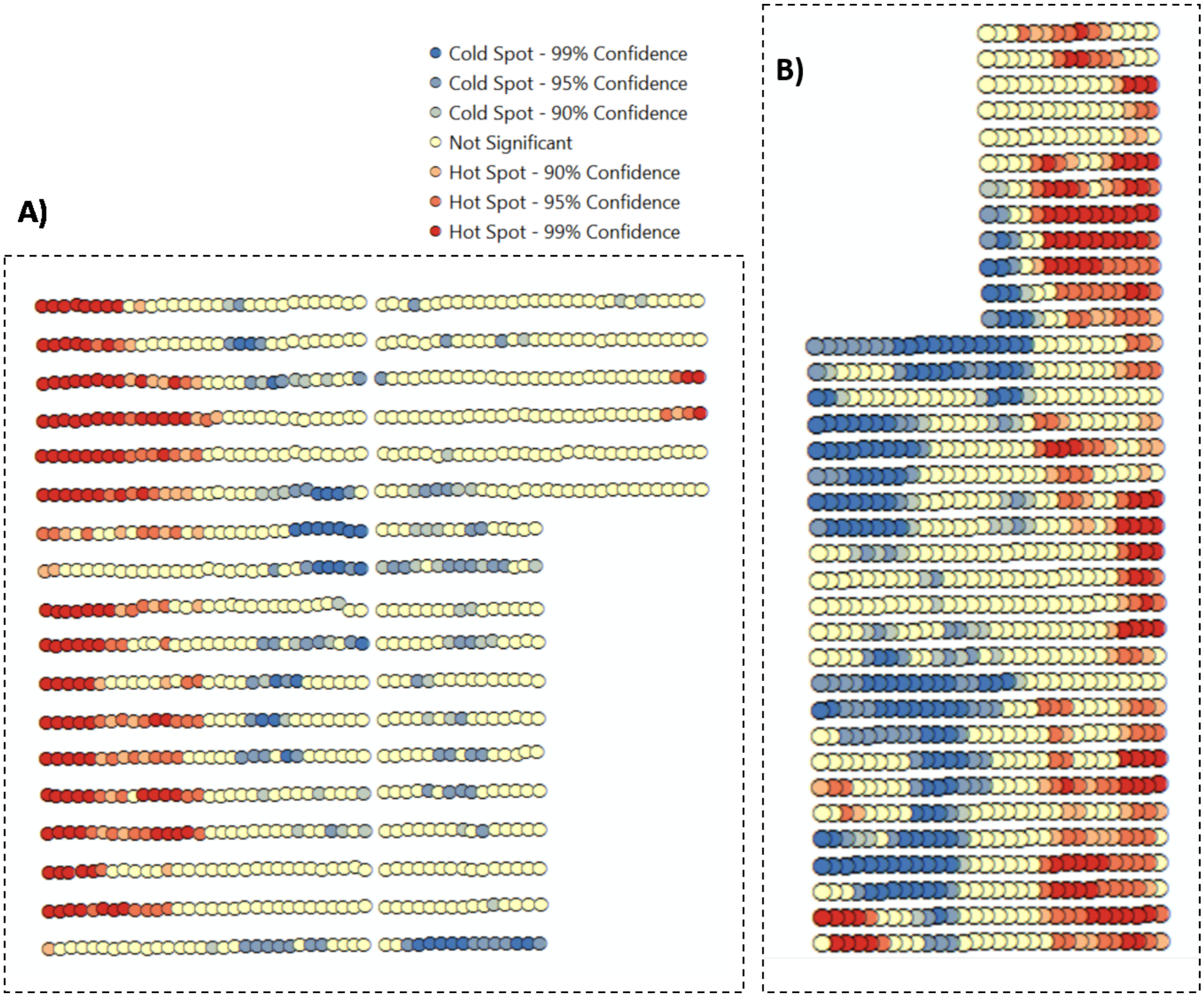

Figure 13 Z score map of A) Drought environment, B) Irrigated Environment. Z score values represent the statistical significance of the spatial clustering of yield values in both environments, with inverse distance conceptualization of spatial relationships and accounting for 8 neighbors for each plot. The circles in the field represent the true centroid of each wheat plots extracted from aerial imagery.

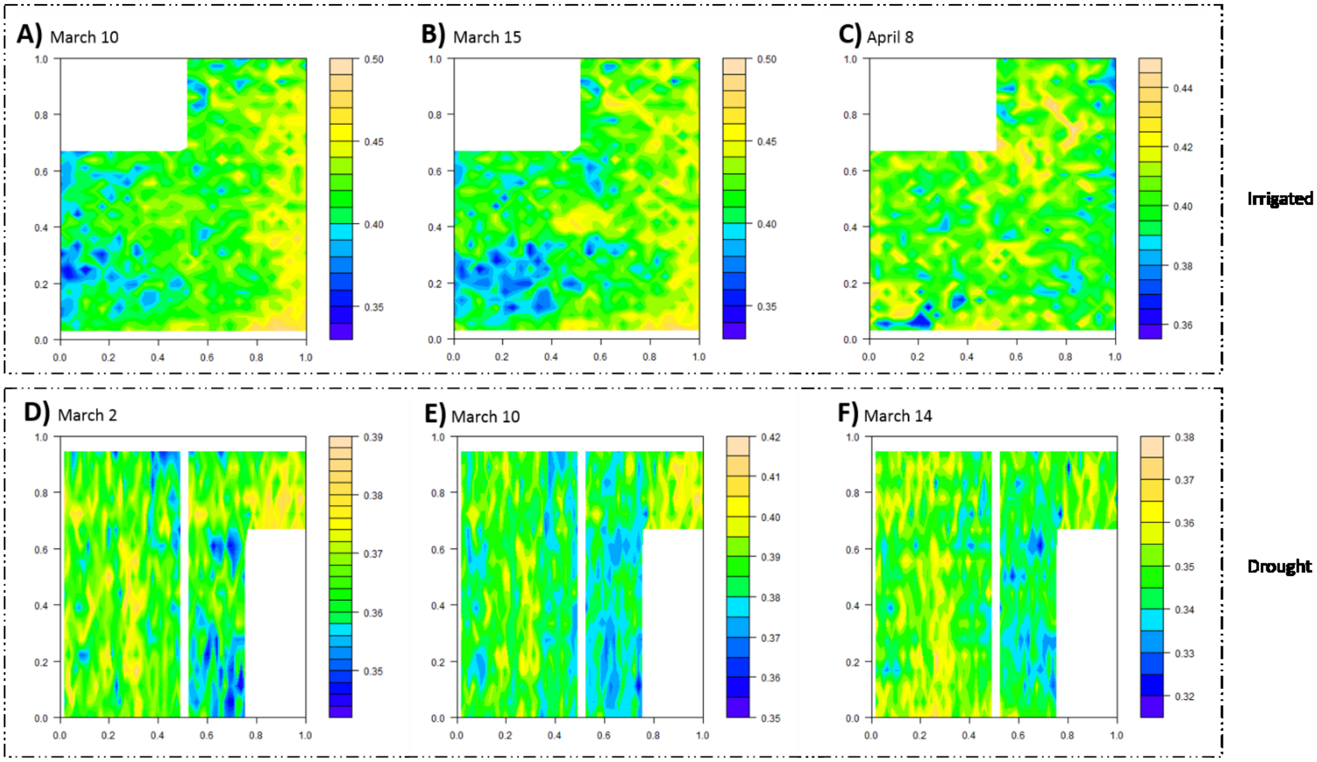

Figure 14 Temporal and spatial pattern analysis of high-throughput phenotyping data extracted from UAS imagery captured at various time points after heading. A) Contour map of GNDVI values obtained on March 10, 2016 from irrigated trials. Spatial variation is observable as high values are clustered in patches on the right side of the field. B) GNDVI map, March 15, 2016, irrigated field. The trend of variation has changed from the last time point, but still high across the field. C) GNDVI map from April 8, 2016, the trend of GNDVI values has changed in this data set, patches of high values are scattered across the field. D) Contour map of GNDVI values extracted from UAS imagery from March 2nd, 2016, in drought trials. Spatial variation is observable in patches across the field. E) GNDVI values from March 10, 2016, the trend has changed, fewer clusters of high values of GNDVI can be observed on the left side of the field, although the pattern on the right side has slight change. F) GNDVI values extracted from March 14 imagery; the spatial variation is very strong in the field, patches of high values on the left side. Slight change of low value clusters on the right side of the field is observable compare to March 10 data set.

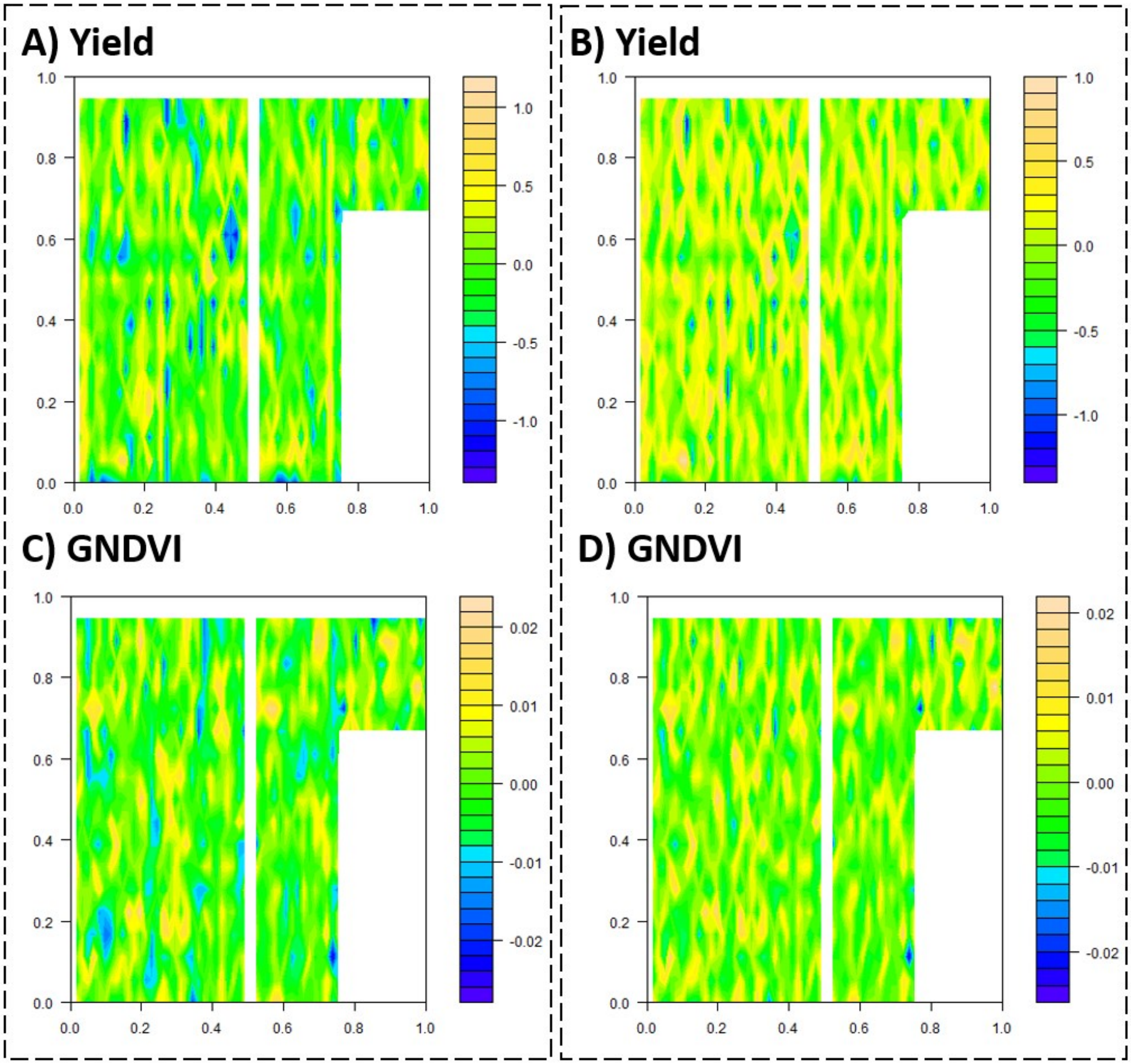

Figure 15 Plot residuals along the field for drought trials. The color scale shows the value of residual effects as indicated: A) Distribution of residual values of yield in drought environment from moving grid adjustment B) Residuals from modified moving grid approach for Yield values, drought environment, C) Plot residuals along the field for GNDVI values, in drought environment from moving grid approach, GNDVI values were extracted from UAS imagery captured on March 10, 2016 D) Residuals for GNDVI values from March 10, 2016, drought from modified moving grid approach.

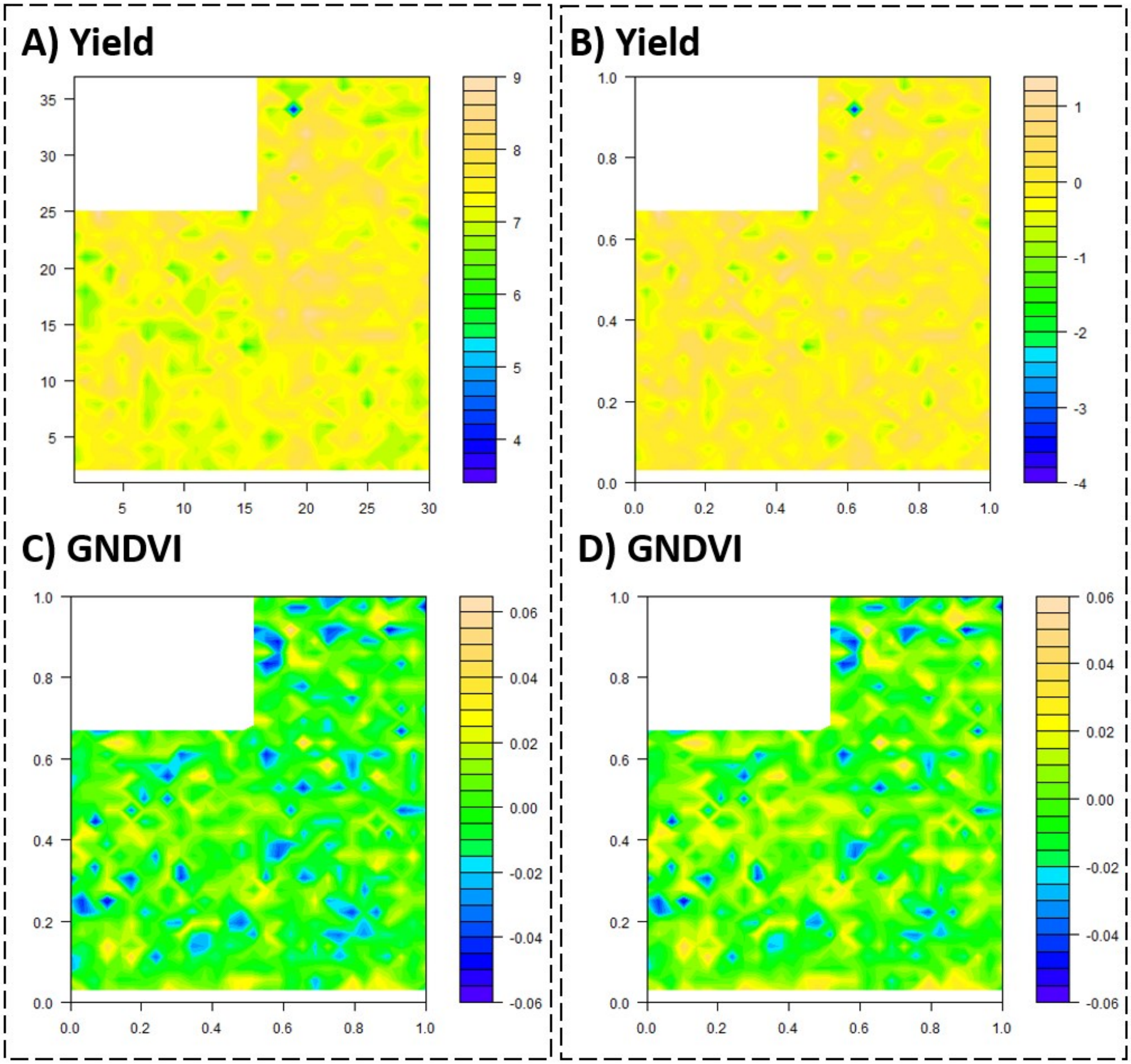

Figure 16 Plot residuals along the field for irrigated trials. The color scale shows the value of residual effects as indicated: A) Distribution of residuals for yield values in irrigated environment using moving grid adjustment B) Residuals from modified moving grid approach for Yield values, drought environment, C) Distribution of residuals for GNDVI values, in drought environment using moving grid adjustment, GNDVI values were extracted from UAS imagery captured on March 10, 2016 D) Residuals for GNDVI values from March 10, 2016, for drought environment, using modified moving grid adjustment.

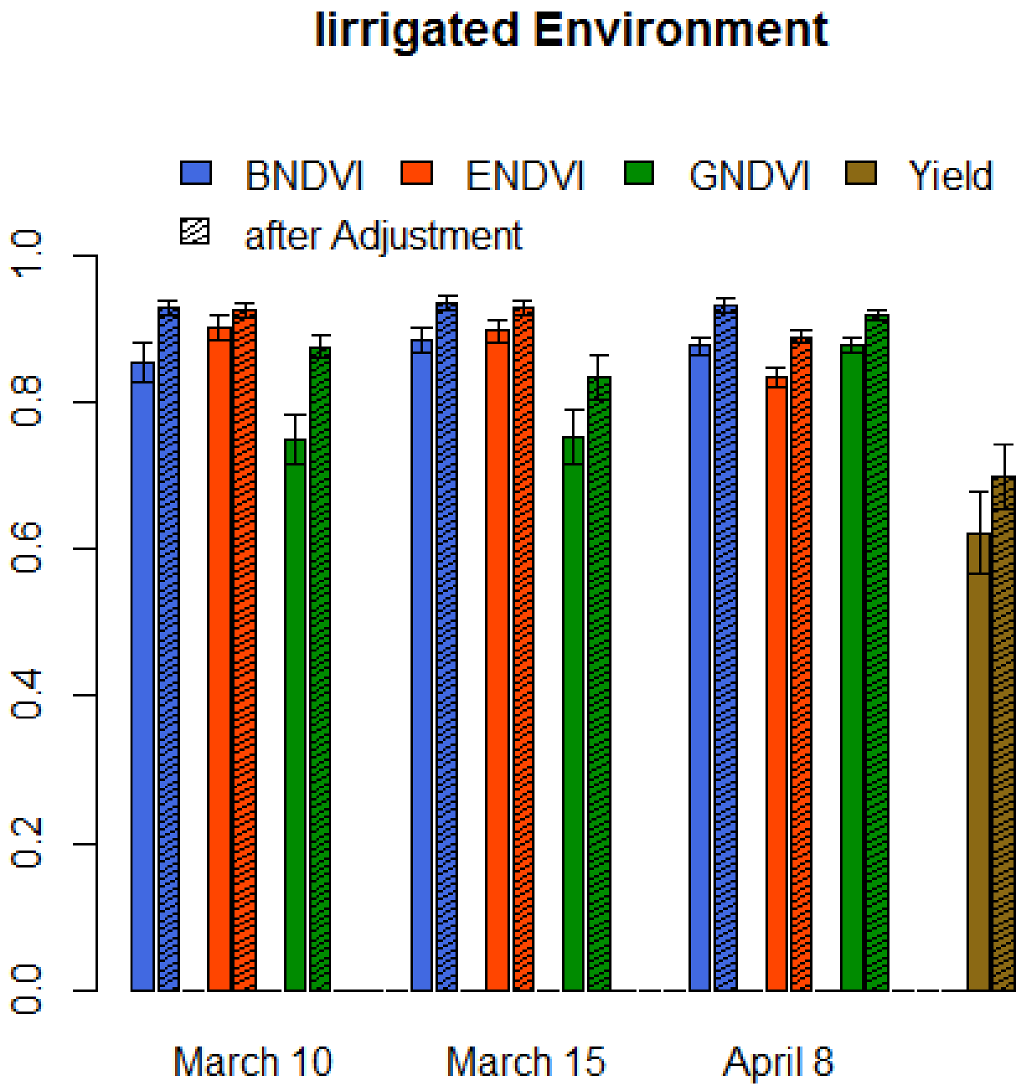

Figure 17 Broad sense heritability within environment and trial. The broad sense heritability was calculated for GNDVI values for each date and yield values in irrigated environment, the average H2 has increased after spatial adjustment for all the GNDVI values, and for yield. The error bars show the standard deviations across all the trials.

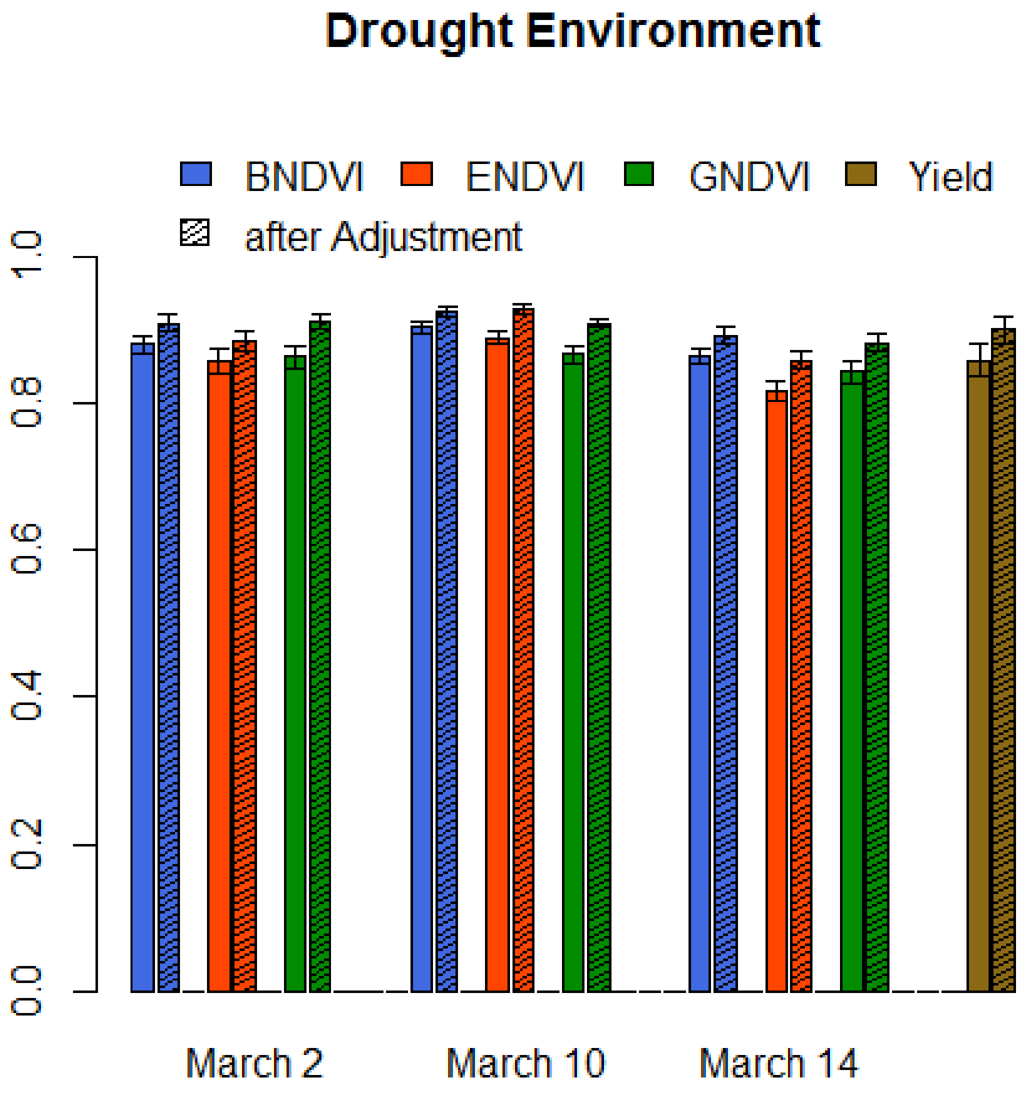

Figure 18 The broad sense heritability was calculated for GNDVI values for each date and yield values in drought environment. H2 has increased after spatial adjustment for all the GNDVI values, and yield. The error bars show the standard deviations across all the trials.

Chapter 5 - Conclusion

The bottleneck of traditional phenotyping methods has limited the ability to understand the interaction between a plant's genotype and its surrounding environment. Traditional measuring techniques widely used in conventional phenotyping, are labor-intensive, time-consuming, costly, and the accuracy is directly upon the precision of the surveyor. In the context of plant breeding and large genetic studies, these techniques are limited in the number of lines that can be adequately assessed for desirable traits.

With the introduction of high-throughput phenotyping (HTP) through unmanned aerial vehicles (UAV) equipped with imaging sensors, breeding programs can rapidly and reliably collect phenotypic data with minimal labor costs and time. This lowering of time and cost constraints allows for breeders to increase the number of lines assessed, thereby increasing the probability of finding genetically superior lines. The HTP pipeline presented in this study shows significant potential for large-scale plant measurement in breeding nurseries using remote sensing and geographic information science (GIS) techniques. The rapid, low-cost evaluation of large field trials in plant breeding with UAV platforms has the potential to greatly accelerate the breeding process through more accurate selections on larger populations.

After developing a pipeline to extract data different vegetation indices and height from UAS imagery, the second step in completing this research was to develop a geospatial method to predict grain yield using spatio-temporal data set. High correlation between GNDVI derived from aerial imagery and field measured allowed accurate prediction of estimated grain yield across the study area.

The final step in accomplishing the major research objective was to evaluate the use of geostatistical spatial analysis for controlling the heterogeneity in high throughput phenotypic data derived from UAS imagery, and yield data of a large wheat breeding nursery. Analyzing the temporal phenotypic data extracted from UAS imagery for two environments during the growing season resulted in detection of the spatially non-random patterns in the data. Geostatistical approaches integrated with moving grid adjustment were examined in two environments contrasting for the accuracy gains as indicated by heritability increases.

HTP data derived from UAS not only enables us with faster data collection, and more number of lines to be assessed, but also it can help us to increase the accuracy of selection. With the help of GIS analysis and geospatial information derived from aerial imagery, we are able to have more precise selection by addressing the phenotypic variations caused by growing conditions.

Our study provides strong evidence of the potential value of UAS for HTP applied to large wheat breeding nurseries. There is strong support of the value of UAS for predicting and evaluating several physiological traits and using this information for overall yield prediction. The use of geospatial statistics along with moving grid adjustment can improve the accuracy of HTP data used by breeders for selection. This integration of remote sensing technologies with geospatial techniques will allow for faster elucidation of the intricacies of the genotype to phenotype dilemma. When brought together, the integration of HTP in wheat breeding programs can help to accelerate the accurate identification of the most superior candidate varieties, increasing the speed and efficiency of the breeding program. The delivery of superior, high-yielding new varieties will help to meet the great challenges of meeting food security and increasing demands of a growing population.

Appendix A - Supplementary Materials

This appendix includes the supplementary figures and tables.

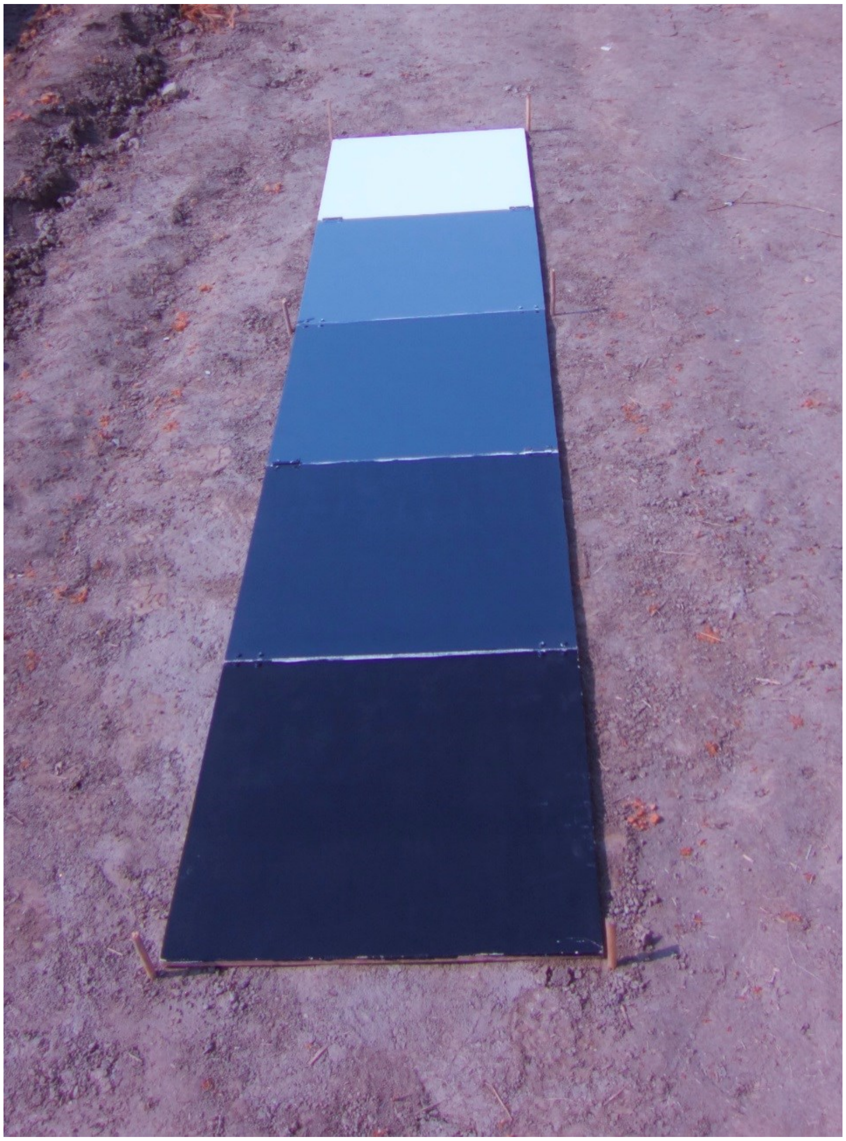

Figure 19 A foldable gray scale reference panel, used in the field for radiometric calibration as well as white balance correction. (Photo credit: Daljit Singh)

Figure 20 Surveying ground control points (GCPs) in the field using RTK GPS. Before the start of HTP 10-13 GCPs were uniformly distributed in the field.

Figure 21 IRIS+ (3D Robotics, Inc, Berkeley, CA 94710, USA) a low cost UAV, carrying modified NIR Canon S100

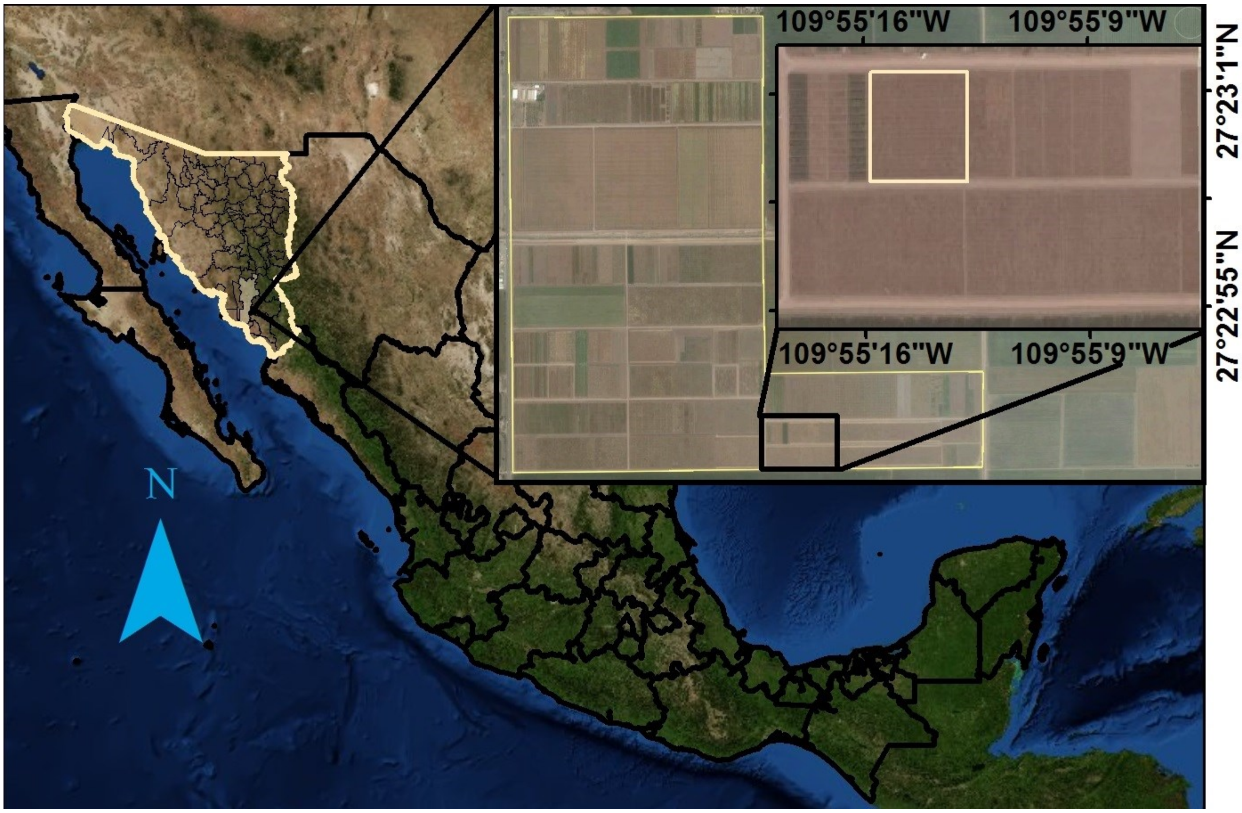

Figure 22 Location of the study area with drought wheat trials in 2016 on the Norman E Borlaug Experiment Station at Ciudad Obregon, Sonora.

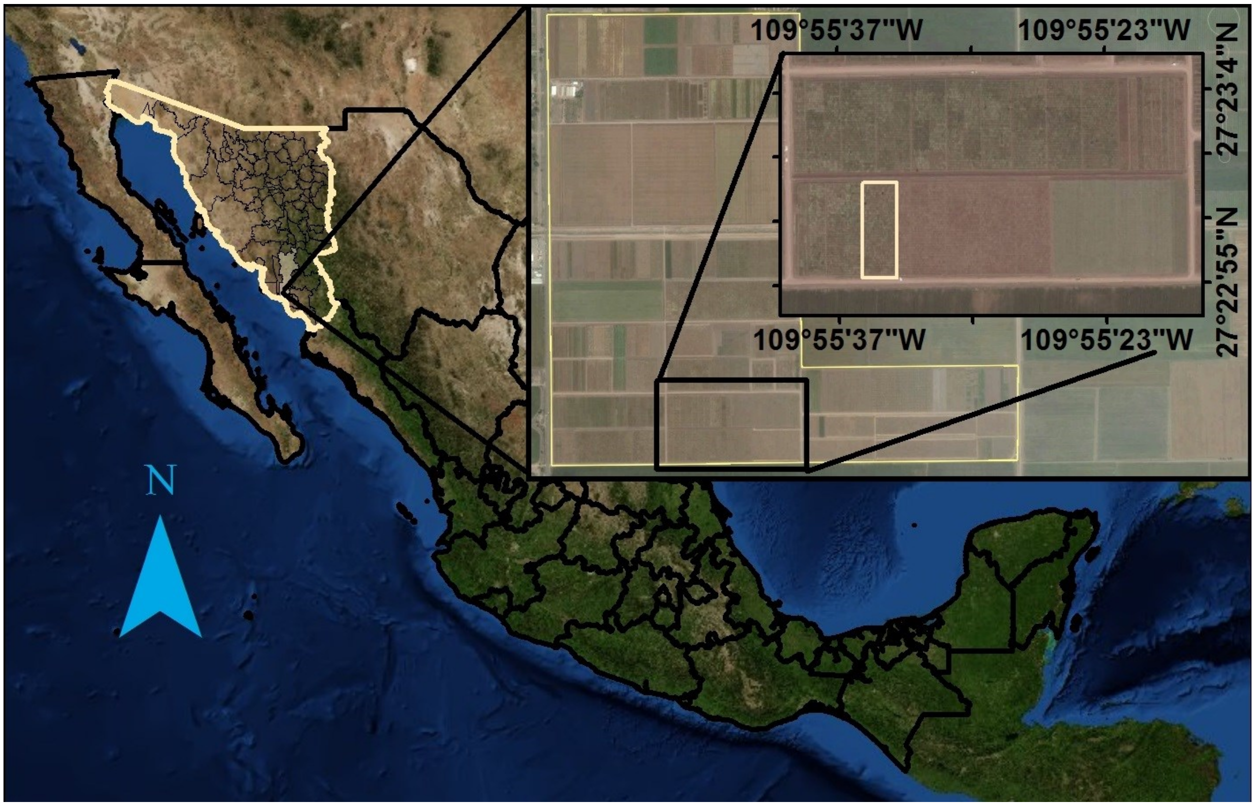

Figure 23 Location of the study area with irrigated wheat trials in 2016 on the Norman E Borlaug Experiment Station at Ciudad Obregon, Sonora.

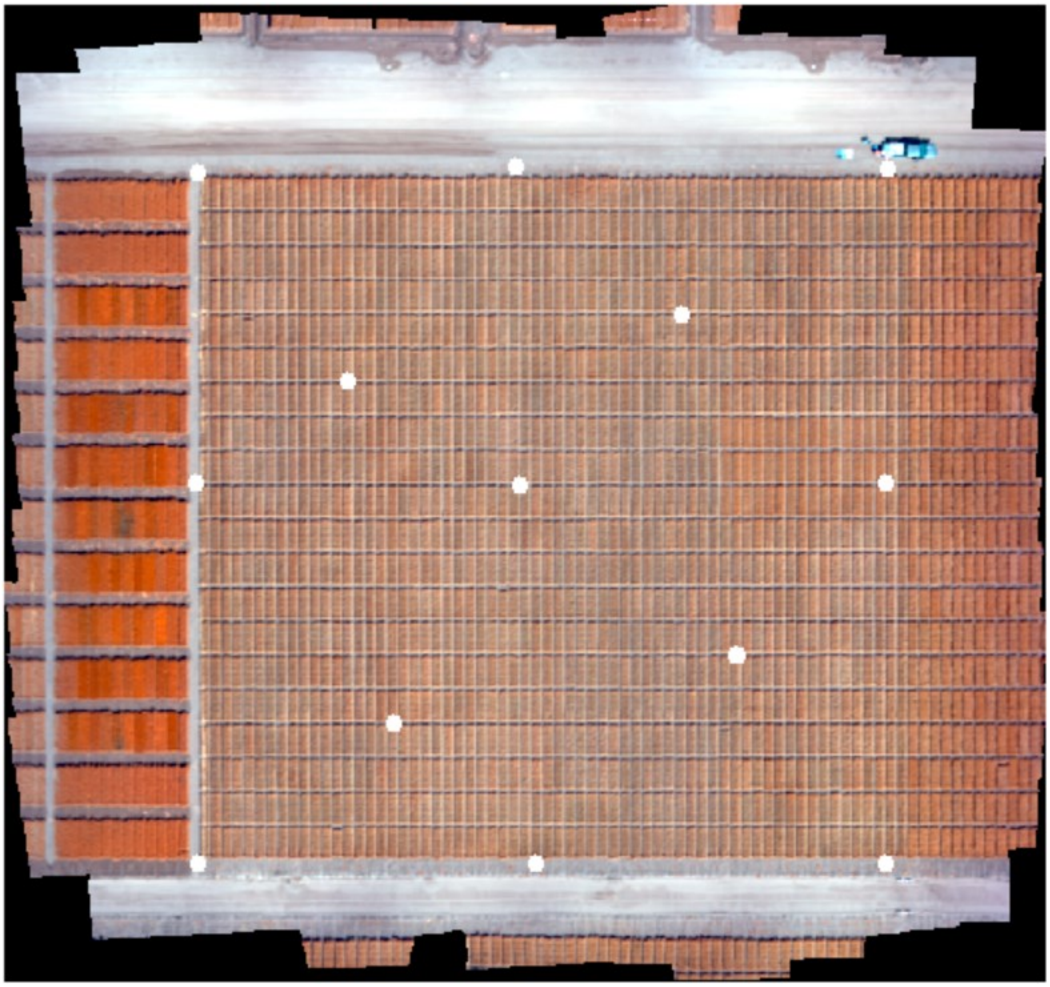

Figure 24 Orthomosaic of UAS imagery captured on March 10, 2016 from drought trials, Norman E Borlaug Experiment Station at Ciudad Obregon, Sonora. 13 GCPs were uniformly distributed across the field before data collection.

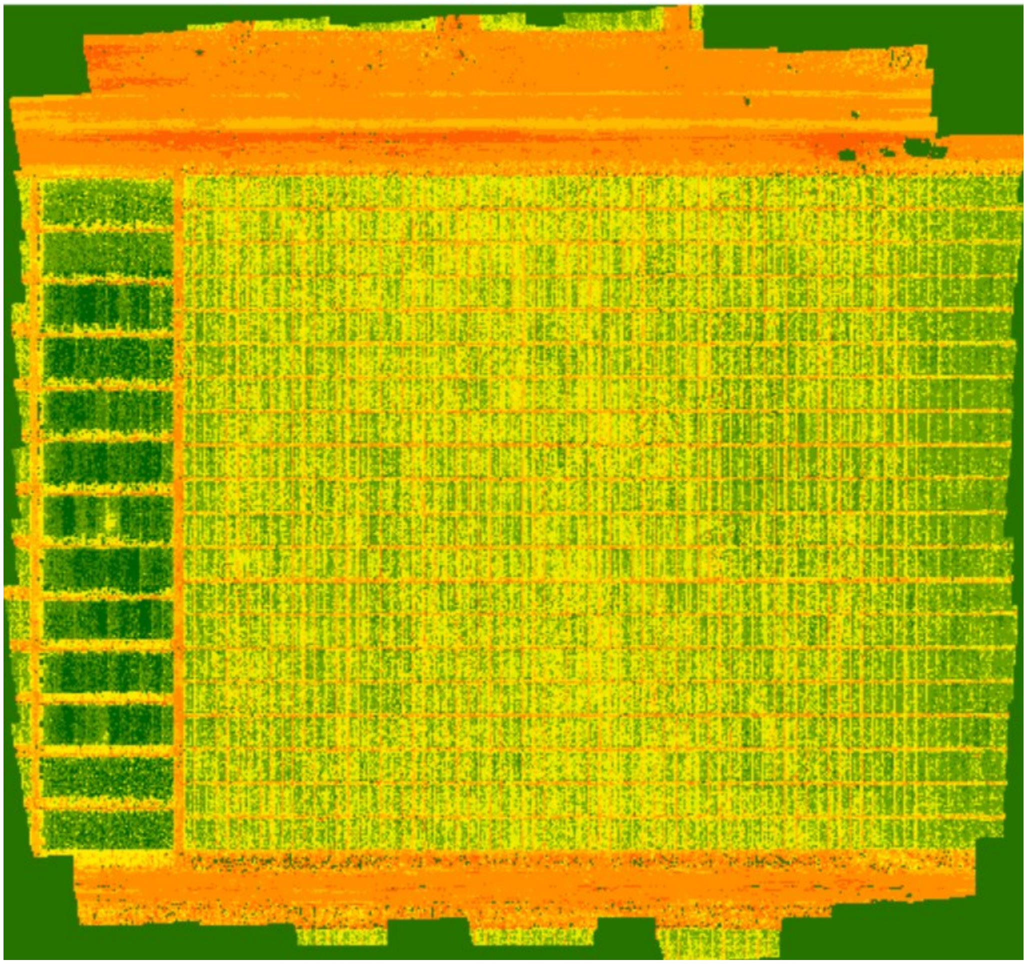

Figure 25 GNDVI map of drought trials, calculated from UAS imagery captured on March 2nd, 2016, which reveal the relative greenness of wheat plots.

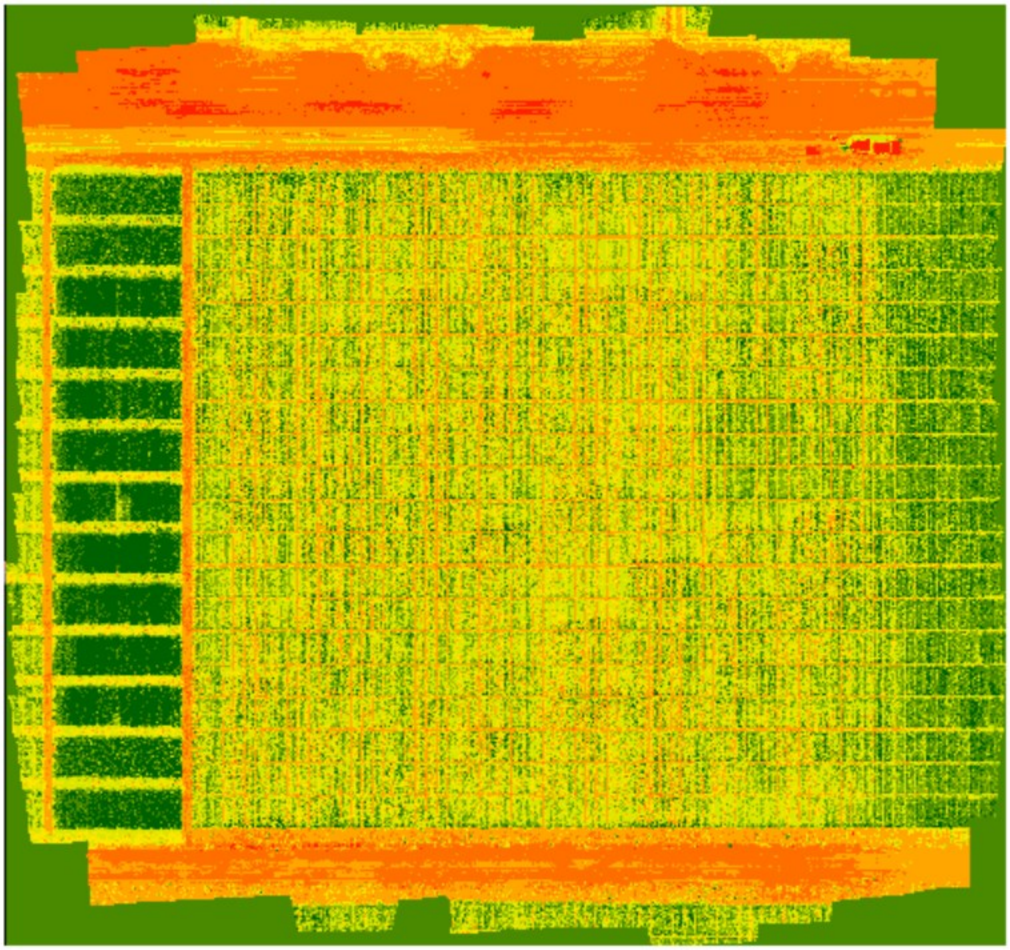

Figure 26 GNDVI map of drought trials, calculated from UAS imagery captured on March 10th, 2016. Low GNDVI values (Less green and more red) indicate a low fraction or absence of green plants on the surface.

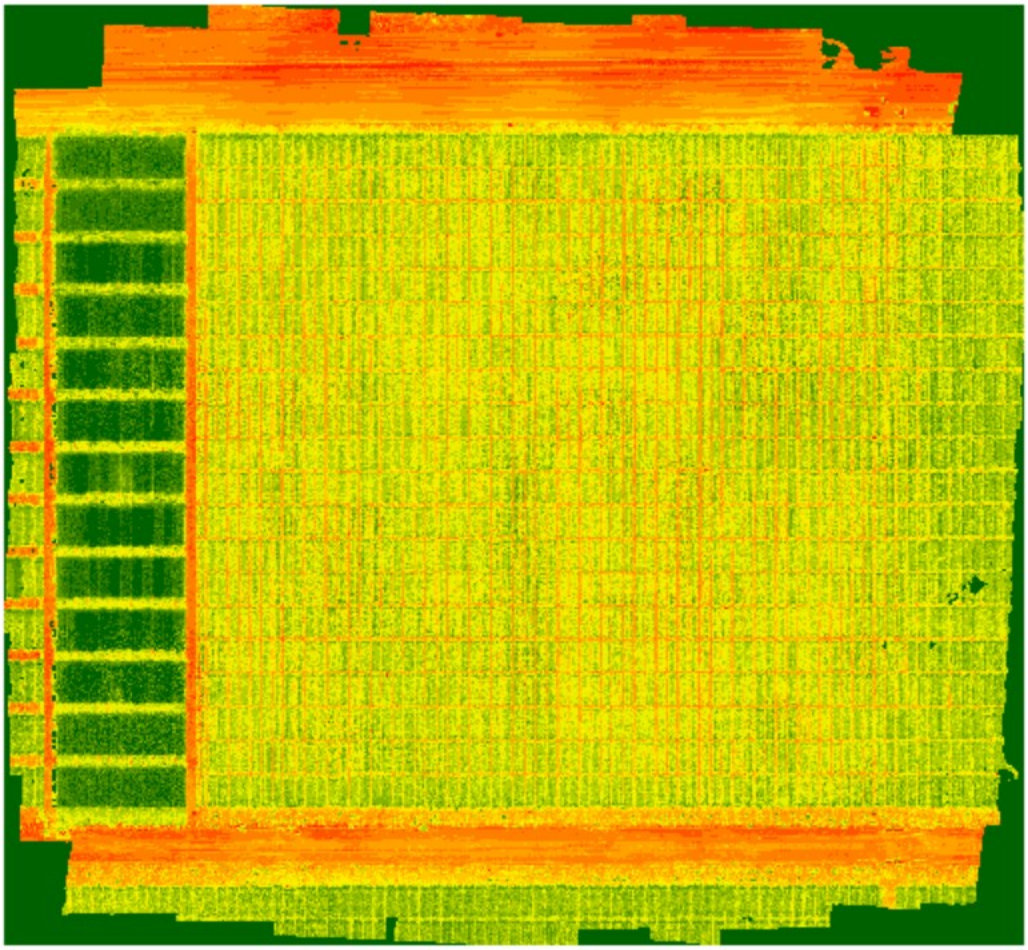

Figure 27 GNDVI map of drought trials, calculated from UAS imagery captured on March 14th, 2016

Appendix B - Supplementary Materials

This chapter includes the scripts used in this dissertation.

Plot Extraction

```
### This scrip takes the modified CSV file that has planting information; plot number, name of the plots, trials, GID, phenotypic information and converts it to KML file. Please read the "readme" that I created to help you with it.
### Developer: Atena Haghighattalab
import argparse
import os
from os.path import basename
import math
from lib.csvfile import Csvfile
from lib.xmlbuilder import XmlKmlBuilder
from lib.timer import Timer


def add_style_to_folder(f_main, xml):
    # add `Style` attribute to Main `Folder`
    s = xml.create_el_style(f_main)

    # add `IconStyle` into `Style` with `scale`
    ics = xml.create_el_icon_style(s)
    xml.create_el_scale(ics, '0.0')

    # add `LabelStyle` into `Style` with `scale`
    lbs = xml.create_el_label_style(s)
    xml.create_el_scale(lbs, '0.5')

    # add `PolyStyle` into `Style` with `fill`
    lbs = xml.create_el_poly_style(s)
    xml.create_el_fill(lbs, '0')
```

```
def addstyle_map_to_folder(f_main, xml):

    # create `StyleMap`
    sm = xml.create_el_style_map(f_main)

    # create `Pair` inside `StyleMap` with `key`
    p = xml.create_el_pair(sm)
    xml.create_el_key(p, 'normal')
    xml.create_el_styleurl(p, '#s_ylw-pushpin')


def main(x1, y1, x2, y2, input_file):

    # TODO: make this as a helper function
    name = os.path.splitext(basename(input_file))[0]

    csvfile = Csvfile(input_file)

    x1o = x1
    width = abs(x1 - x2)
    height = abs(y1 - y2)

    print(width)
    print(height)

    xml = XmlKmlBuilder()
    d = xml.create_el_document()

    # Main `Folder` with name
```

```
f_main = xml.create_el_folder(d)
xml.create_el_name(f_main, name)

# `Folder` with name (OriginPoints)
f_origin_points = xml.create_el_folder(d)
xml.create_el_name(f_origin_points, name + '-Puntos de Origen')

# `Folder` with name (Points)
f_points = xml.create_el_folder(d)
xml.create_el_name(f_points, name + '-Puntos')

add_style_to_folder(f_main, xml)
addstyle_map_to_folder(f_main, xml)

# left-top `Placemark`
pm = xml.create_el_placemark(f_origin_points)
xml.create_el_name(pm, 'Punto 1')
pt = xml.create_el_point(pm)
xml.create_el_coordinates(pt, str(x1) + "," + str(y1) + ",0")

# bottom-right `Placemark`
pm = xml.create_el_placemark(f_origin_points)
xml.create_el_name(pm, 'Punto 2')
pt = xml.create_el_point(pm)
xml.create_el_coordinates(pt, str(x2) + "," + str(y2) + ",0")

# ------------------ ------------------ ------------------ ------------------ ------------------

# count sum of rows in first column
hm = 0.0
for row in range(0, csvfile.rows_count()):
```

```
    if csvfile.is_number(0, row):
        hm += csvfile.get_number(0, row)

# count sum of cols in first row
wm = 0.0
for col in range(0, csvfile.cols_count()):
    if csvfile.is_number(col, 0):
        wm += csvfile.get_number(col, 0)

not_empty_elements = []

for row in range(1, csvfile.rows_count()):
    with Timer() as t:
        for col in range(1, csvfile.cols_count()):

            id_val = str(csvfile.get(col, row))

            # `porcentajex` is how many GEO points in current column number
            if csvfile.is_number(col, 0) and wm != 0:
                porcentajex = csvfile.get_number(col, 0) / wm
            else:
                porcentajex = 0

            if csvfile.is_number(0, row) and hm != 0:
                porcentajey = csvfile.get_number(0, row) / hm
            else:
                porcentajey = 0

            # 1st point (left-top)
            x = x1
            y = y1
```

```
coord = format(x, '.12f') + "," + format(y, '.12f') + ",0 "
coord_point = ""

# 2nd point (right-top)
x = x1 + (width * porcentajex)
coord_point += format(x1 + (width * porcentajex / 2), '.12f') + ","
coord += format(x, '.12f') + "," + format(y, '.12f') + ",0 "

yempty = 0
for in_row in range(row, csvfile.rows_count()):
   if csvfile.get(in_row, col) == "-":
      not_empty_elements.append(str(in_row) + '-' + str(col))
      yempty += csvfile.get(in_row, 0) / hm
   else:
      break

coord_point += format(y1 - (height * (porcentajey + yempty) / 2), '.12f') + ",0"

# 3rd (right-bottom)
y = y1 - (height * (porcentajey + yempty))
coord += format(x, '.12f') + "," + format(y, '.12f') + ",0 "

# 4rd (left-bottom)
x = x1
coord += format(x, '.12f') + "," + format(y, '.12f') + ",0 "

# 1st point again
y = y1
coord += format(x, '.12f') + "," + format(y, '.12f') + ",0"

x1 = x1 + (width * porcentajex)
```

```
            if (str(row) + '-' + str(col)) not in not_empty_elements and id_val != "" and id_val != "-
":

                # add placemark
                pm = xml.create_el_placemark(f_main)
                xml.create_el_name(pm, id_val)
                xml.create_el_description(pm, id_val)
                xml.create_el_styleurl(pm, '#m_ylw-pushpin')

                pl = xml.create_el_polygon(pm)
                xml.create_el_tessellate(pl, '1')
                obi = xml.create_el_outer_boundary_is(pl)
                lr = xml.create_el_linear_ring(obi)
                xml.create_el_coordinates(lr, coord)

                # Add placemark
                pm = xml.create_el_placemark(f_points)
                xml.create_el_styleurl(pm, '#m_ylw-pushpin')
                xml.create_el_name(pm, id_val)
                p = xml.create_el_point(pm)
                xml.create_el_coordinates(p, coord_point)

            # if cell is empty, but next one has something -> this is horizontal gap
            # if "" == csvfile.get(col, row) and "" != csvfile.get(col+1, row):
            #
            #     x1 += csvfile.get_number(col, 0) * porcentajex
            #
            #     print(porcentajex)
            #     print(width * porcentajex)
            #     print(csvfile.get_number(col, 0) * porcentajex)
```

```
            #    print(col)
            #    print(row)
            #    exit()

        print "=> elasped lpush: %s s" % t.secs

        print(str(math.floor(float(row) / float(csvfile.rows_count()) * 100)) + "% completed")

        x1 = x1o
        y1 = y1 - (height * porcentajey)

    # ------------------ ------------------ ------------------ ------------------ ------------------

    # output
    xml.save('output.kml')


#   Input variables:
#   --y1
#   --x1
#   --y2
#   --x2
#   -f --input-file
if __name__ == "__main__":

    parser = argparse.ArgumentParser()

    parser.add_argument('-y1', type=float, required=True, help="")
    parser.add_argument('-x1', type=float, required=True, help="")
    parser.add_argument('-y2', type=float, required=True, help="")
    parser.add_argument('-x2', type=float, required=True, help="")
```

```
parser.add_argument('-f', '--input-file', type=str, required=True, help="")

args = parser.parse_args()

main(args.x1, args.y1, args.x2, args.y2, args.input_file)
```

Orthomosaic Generation

```
## Author:      Atena Haghighattalab
## Created:     07/08/2014
## Modified: 25/03/2015

import os
import PhotoScan



def main():

    global doc
    doc = PhotoScan.app.document

    app = QtGui.QApplication.instance()
    parent = app.activeWindow()

    #prompting for path to photos
    path_photos = PhotoScan.app.getExistingDirectory("Specify input photo folder:")
    path_psz = PhotoScan.app.getSaveFileName("Specify path for the PSZ project file:")
    path_export = PhotoScan.app.getExistingDirectory("Specify EXPORT folder:")

    #processing parameters
    accuracy = PhotoScan.Accuracy.HighAccuracy  #align photos accuracy
    preselection = PhotoScan.Preselection.ReferencePreselection
    keypoints = 40000 #align photos key point limit
    tiepoints = 10000 #align photos tie point limit
    source = PhotoScan.PointsSource.DensePoints #build mesh source
    surface = PhotoScan.SurfaceType.HeightField #build mesh surface type
    quality = PhotoScan.Quality.MediumQuality #build dense cloud quality
    filtering = PhotoScan.FilterMode.AggressiveFiltering #depth filtering
```

```
interpolation = PhotoScan.Interpolation.EnabledInterpolation #build mesh interpolation
face_num = PhotoScan.FaceCount.HighFaceCount #build mesh polygon count
mapping = PhotoScan.MappingMode.OrthophotoMapping #build texture mapping
atlas_size = 8192
blending = PhotoScan.BlendingMode.MosaicBlending #blending mode
color_corr = False


print("Script started")

#creating new chunk
doc.addChunk()
chunk = doc.chunks[-1]
chunk.label = "New Chunk"

#loading images
image_list = os.listdir(path_photos)
photo_list = list()
for photo in image_list:
        if ("jpg" or "jpeg" or "JPG" or "JPEG") in photo.lower():
                photo_list.append(path_photos + "\\" + photo)
chunk.addPhotos(photo_list)

#loading coordinates from EXIF and setting up the coordinate system
chunk.loadReferenceExif()
chunk.crs = PhotoScan.CoordinateSystem("EPSG::4326")
proj = chunk.crs
PhotoScan.app.update()

#align photos
```

```
    chunk.matchPhotos(accuracy = accuracy, preselection = preselection, filter_mask =
False, keypoint_limit = keypoints, tiepoint_limit = tiepoints)
    chunk.alignCameras()

    chunk.optimizeCameras()

    #building dense cloud
    PhotoScan.app.gpu_mask = 1  #GPU devices binary mask
    PhotoScan.app.cpu_cores_inactive = 2  #CPU cores inactive
    chunk.buildDenseCloud(quality = quality, filter = filtering)

    #building mesh
    chunk.buildModel(surface = surface, source = source, interpolation = interpolation,
face_count = face_num)

    #build texture
    chunk.buildUV(mapping = mapping, count = 1)
    chunk.buildTexture(blending = blending , color_correction = color_corr, size =
atlas_size)

    doc.save(path_psz)
    PhotoScan.app.update()

    ###exporting DEM and Orthophoto

    #estimating effective ground resolution
    #recalculating WGS84 resolution from degrees into meters if export projection (proj) is
WGS84
    if proj.authority == "EPSG::4326":
        coord = PhotoScan.Vector([0,0,0])
        cam_num = 0
```

```
        for camera in chunk.cameras:
            if not camera.transform:
                continue
            coord += proj.project(chunk.transform.matrix.mulp(camera.center))
            cam_num += 1

        crd = (1. / cam_num) * coord

        #longitude
        v1 = PhotoScan.Vector((crd[0], crd[1], 0) )
        v2 = PhotoScan.Vector((crd[0] + 0.001, crd[1], 0))
        vm1 = proj.unproject(v1)
        vm2 = proj.unproject(v2)
        res_x = (vm2 - vm1).norm() * 1000

        #latitude
        v2 = PhotoScan.Vector( (crd[0], crd[1] + 0.001, 0))
        vm2 = proj.unproject(v2)
        res_y = (vm2 - vm1).norm() * 1000

        d_x = d_x / res_x
        d_y = d_y / res_y


    chunk.exportDem(path_export + "\\DEM.tif", format = "tif", projection = proj, dx = d_x, dy = d_y, nodata = -32767, crop_borders = True, write_kml = False, write_world = False)
    chunk.exportOrthophoto(path_export + "\\ortho.tif", format='tif', blending = blending, dx = d_x, dy = d_y, color_correction = color_corr, projection = proj, write_kml = False, write_world = False)

    print("Script finished")
```

```
PhotoScan.app.addMenuItem("Custom menu/Process 1", main)
```

Geographically Weighted Regression Models

```
        ### this function is modified from gwr.predict in GWmodel package ###

        gwr.predict.mod = function(formula, data, predictdata, bw, kernel, approach, adaptive, p,
theta, longlat, generate.prediction.var=F) {

         fd.locat <- coordinates(data) ### extract training co-ordinate
         fd.n <- nrow(fd.locat) ### number of training co-ordinate

         pd.locat <- coordinates(predictdata) ### extract test co-ordinate
         pd.n <- nrow(pd.locat) ### number of test co-ordinate

##################################################################################
########################################################
         ### THIS WHOLE CHUNK IS TO EXTRACT OUT THE PROPER X (independent
variable) AND Y (dependent variable) VALUES from the training data #
```

```
#####################################################################################
############################################################
	mf <- match.call(expand.dots = FALSE)
	m <- match(c("formula", "data"), names(mf), 0L)
	mf <- mf[c(1L, m)]
	mf$drop.unused.levels <- TRUE
	mf[[1]] <- as.name("model.frame")
	mf <- eval(mf, parent.frame())
	mt <- attr(mf, "terms")
	y <- model.extract(mf, "response")
	x <- model.matrix(mt, mf)

	var.n <- ncol(x) ### number of predictor (including intercept)
	idx1 <- match("(Intercept)", colnames(x)) ### identify intercept column
	if (!is.na(idx1)) {colnames(x)[idx1] <- "Intercept"} ### some renaming
	inde_vars <- colnames(x)[-1] ### names of independent variables (excluding intercept
column)


	########################################
	### THIS IS TO EXTRACT THE TEST DATA ###
	########################################
```

```
predictdata <- as(predictdata, "data.frame") ### convert the test data to dataframe
x.p <- predictdata[, inde_vars] ### extract the test indepedent variables
x.p <- cbind(rep(1, pd.n), x.p) ### add intercept ("1")
x.p <- as.matrix(x.p)


###########################################
#### PART 1: FOCUS ON TEST DATA ###########
#### THIS IS THE ACTUAL PREDICTION STEP ###
###########################################

### matrix to hold the weights
wt <- matrix(nrow = fd.n, ncol = pd.n)

### matrix to hold xtxinv (i.e. inverse of t(x) %*% t)
xtxinv <- as.double(rep(0, pd.n * var.n * var.n))
dim(xtxinv) <- c(pd.n, var.n, var.n)

### matrix to hold beta
betas1 <- matrix(nrow = pd.n, ncol = var.n)

### for each set of test co-ordinate
for (i in 1:pd.n) {
```

```
  ### get GW distance between train co-ordinate and test co-ordinate

  dist.vi <- gw.dist(fd.locat, pd.locat, focus = i, p, theta, longlat)


  ### assign corresponding GW weights

  W.i <- gw.weight(dist.vi, bw, kernel, adaptive)


  ### record the weight (W.i) in wt

  wt[, i] <- W.i


  ### GW regression on x and y using weight (W.i)

  gw.resi <- gw.reg1(x, y, W.i, i)


  ### record the beta values

  betas1[i, ] <- gw.resi[[1]]


  ### record the xtxinv

  xtxinv[i, , ] <- gw.resi[[2]]

}


### THIS IS THE PREDICTION STEP!!!

### predict using x.p (predictor independent variables) and betas1 (previously recorded)

gw.predict <- gwr.fitted(x.p, betas1)
```

```
    if (generate.prediction.var) {


################################################################################
      ### Everything below are for generating the regression statistics only ###

################################################################################

      ########################################
      #### PART 2: FOCUS ON TRAINING DATA ###
      ########################################

      ### matrix to hold beta
      betas2 <- matrix(nrow = fd.n, ncol = var.n)

      ### S is analogous to xtxinv above, but the form is much simpler
      S <- matrix(nrow = fd.n, ncol = fd.n)

      for (i in 1:fd.n) {
        dist.vi <- gw.dist(fd.locat, fd.locat, focus = i, p, theta, longlat)
        W.i <- gw.weight(dist.vi, bw, kernel, adaptive)
```

```
  gw.resi <- gw.reg(x, y, W.i, T, i)

  betas2[i, ] <- gw.resi[[1]]

  S[i, ] <- gw.resi[[2]]

}


tr.S <- sum(diag(S))

tr.StS <- sum(S^2)

Q <- t(diag(fd.n) - S) %*% (diag(fd.n) - S)

RSS.gw <- t(y) %*% Q %*% y

sigma.hat <- RSS.gw/(fd.n - 2 * tr.S + tr.StS)

    predict.var <- numeric(pd.n)

for (i in 1:pd.n) {

  w2 <- wt[, i] * wt[, i]

  w2x <- x * w2

  xtw2x <- t(x) %*% w2x

  xtxinvp <- c()

  for (j in 1:var.n) xtxinvp <- rbind(xtxinvp, xtxinv[i, , j])

  s0 <- xtxinvp %*% xtw2x %*% xtxinvp

  x.pi <- x.p[i, ]

  dim(x.pi) <- c(1, length(x.pi))

  s1 <- x.pi %*% s0 %*% t(x.pi)

  pse <- (sqrt(sigma.hat)) * (sqrt(1 + s1))

  pvar <- (pse)^2
```

```
     predict.var[i] <- pvar
    }
      gwr.pred.df <- data.frame(betas1, gw.predict, predict.var)
  } else {
    gwr.pred.df <- data.frame(betas1, gw.predict, NA)
  }
   ### clean up and output data
  colnames(gwr.pred.df) <- c(paste(colnames(x), "coef", sep = "_"), "prediction",
"prediction_var")
    form =  as.character(formula)
  form = form[2]
  gwr.pred.df = cbind(gwr.pred.df, actual=predictdata[,form])
  rownames(pd.locat) <- rownames(gwr.pred.df)
  SDF = SpatialPointsDataFrame(coords = pd.locat, data = gwr.pred.df)
  return(SDF)
}

### this function is modified from gwr.predict in GWmodel package ###

gwr.predict.mod.quick = function(formula, data, predictdata, bw,  kernel, approach,
adaptive, p, theta, longlat.type, DM, train.numbering, test.numbering) {

  fd.locat <- coordinates(data) ### extract training co-ordinate
```

```
    fd.n <- nrow(fd.locat) ### number of training co-ordinate

    pd.locat <- coordinates(predictdata) ### extract test co-ordinate
    pd.n <- nrow(pd.locat) ### number of test co-ordinate

###########################################################################################
##########################################################
    ### THIS WHOLE CHUNK IS TO EXTRACT OUT THE PROPER X (independent
variable) AND Y (dependent variable) VALUES from the training data #

###########################################################################################
##########################################################
    mf <- match.call(expand.dots = FALSE)
    m <- match(c("formula", "data"), names(mf), 0L)
    mf <- mf[c(1L, m)]
    mf$drop.unused.levels <- TRUE
    mf[[1]] <- as.name("model.frame")
    mf <- eval(mf, parent.frame())
    mt <- attr(mf, "terms")
    y <- model.extract(mf, "response")
    x <- model.matrix(mt, mf)
```

```
var.n <- ncol(x) ### number of predictor (including intercept)
idx1 <- match("(Intercept)", colnames(x)) ### identify intercept column
if (!is.na(idx1)) {colnames(x)[idx1] <- "Intercept"} ### some renaming
inde_vars <- colnames(x)[-1] ### names of independent variables (excluding intercept column)

########################################
### THIS IS TO EXTRACT THE TEST DATA ###
########################################
predictdata <- as(predictdata, "data.frame") ### convert the test data to dataframe
x.p <- predictdata[, inde_vars] ### extract the test indepedent variables
x.p <- cbind(rep(1, pd.n), x.p) ### add intercept ("1")
x.p <- as.matrix(x.p)

###########################################
#### PART 1: FOCUS ON TEST DATA ###########
#### THIS IS THE ACTUAL PREDICTION STEP ###
###########################################

### matrix to hold the weights
wt <- matrix(nrow = fd.n, ncol = pd.n)
```

```
### matrix to hold xtxinv (i.e. inverse of t(x) %*% t)

xtxinv <- as.double(rep(0, pd.n * var.n * var.n))

dim(xtxinv) <- c(pd.n, var.n, var.n)


### matrix to hold beta

betas1 <- matrix(nrow = pd.n, ncol = var.n)


### for each set of test co-ordinate

for (i in 1:pd.n) {


  ### use pre.compute DM

  dist.vi <- DM[test.numbering[i], train.numbering]


  ### assign corresponding GW weights

  W.i <- gw.weight(dist.vi, bw, kernel, adaptive)


  ### record the weight (W.i) in wt

  wt[, i] <- W.i


  ### GW regression on x and y using weight (W.i)

  gw.resi <- gw.reg1(x, y, W.i, i)
```

```
      ### record the beta values
      betas1[i, ] <- gw.resi[[1]]

      ### record the xtxinv
      xtxinv[i, , ] <- gw.resi[[2]]
    }

    ### THIS IS THE PREDICTION STEP!!!
    ### predict using x.p (predictor independent variables) and betas1 (previously recorded)
    gw.predict <- gwr.fitted(x.p, betas1)

    ### Skip the variance calculation
    gwr.pred.df <- data.frame(betas1, gw.predict, NA)

    ### clean up and output data
    colnames(gwr.pred.df) <- c(paste(colnames(x), "coef", sep = "_"), "prediction",
"prediction_var")

    form =  as.character(formula)
    form = form[2]
    gwr.pred.df = cbind(gwr.pred.df, actual=predictdata[,form])
    rownames(pd.locat) <- rownames(gwr.pred.df)
    SDF = SpatialPointsDataFrame(coords = pd.locat, data = gwr.pred.df)
```

```
 return(SDF)

}

gwr.bootstrap = function(formula.reg, data, output.folder, bootstrap, percentage.test, kernel, bandwidth=NULL,  approach, adaptive, p, theta, longlat) {

 data.full = data

 out.fold = file.path(output.folder)

 ### calculate GW matrix
 print("Calculate GW distance matrix...")
 DM = gw.dist(dp.locat=coordinates(data.full))

 ### select best bw
 if (is.null(bandwidth)) {
  print("Select best bandwidth...")
  bw.best = bw.gwr(formula(formula.reg), data.full, approach, kernel, adaptive, p, theta, longlat, DM)
 } else {
  bw.best = bandwidth
 }
```

```
    write(paste("Bandwith:", bw.best), paste(out.fold, "/bootstrap_log.txt", sep=""), append = T)


    ### bootstrap
    print("Start Bootstrap procedure...")
    num.data = nrow(data.full)
    write(paste("Number of total data:", num.data), paste(out.fold, "/bootstrap_log.txt", sep=""), append = T)
    write(paste("Percentage of test data:", percentage.test, "%"), paste(out.fold, "/bootstrap_log.txt", sep=""), append = T)
    num.test = round(num.data*percentage.test/100, 0)
    write(paste("Number of test data:", num.test), paste(out.fold, "/bootstrap_log.txt", sep=""), append = T)

    row.numbering = 1:num.data

    bootstrap.raw = list()

    progbar = utils::txtProgressBar(style = 3)
    for (i in 1:bootstrap) {

      test.numbering = sort(sample(row.numbering, num.test))
      train.numbering = row.numbering[!row.numbering %in% test.numbering]
```

```
      ### training
      data.train = data.full[train.numbering,]

      ### test
      data.test = data.full[test.numbering,]

      ### use GW regression (simplified function) for prediction
      temp =  gwr.predict.mod.quick(formula(formula.reg), data.train, data.test, bw.best,
kernel, approach, adaptive, p, theta, longlat, DM, train.numbering, test.numbering)

      bootstrap.raw[[i]] = as.matrix(data.frame(temp)[,c("prediction", "actual")])

      utils::setTxtProgressBar(progbar, i/bootstrap)
    }
    close(progbar)

    print("Saving bootstrap results...")
    save(bootstrap.raw, file = paste(out.fold, "/bootstrap_raw.RObj", sep=""))

    print("Calculate summary statistics...")
    bootstrap.result = do.call(rbind, lapply(bootstrap.raw, function(x) {
      t.ssq = sum((x[,2]-mean(x[,2]))^2)
```

```
              r.ssq = sum(abs(x[,1]-x[,2])^2)
              R2.model = 1 - r.ssq/t.ssq
              temp = cor.test(x[,1], x[,2])
              return(c(p=temp$p.value, cor=as.numeric(temp$est), R2.model=R2.model))
            }))
            bootstrap.result = data.frame(bootstrap.result)
            write.table(bootstrap.result, file = paste(out.fold, "/bootstrap_result.txt", sep=""),
sep="\t", quote=F, row.names=F, col.names=T)
            save(bootstrap.result, file = paste(out.fold, "/bootstrap_result.RObj", sep=""))

            bootstrap.summary = summary(bootstrap.result)
            write.table(bootstrap.summary, file = paste(out.fold, "/bootstrap_summary.txt", sep=""),
quote=F)

            print("DONE")

          }
```